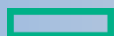# SVS FEM
Your partner in computing

Proceedings of
27th SVSFEM ANSYS Users' Group Meeting and Conference 2019
12th – 14th of June 2019, Olomouc, Czech Republic

Sponsors:

Hewlett Packard Enterprise

CADFEM®

ANSYS®

http://aum.svsfem.cz

Content

PEVNOSTNÍ KONTROLA RADIÁLNÍHO KOMPRESOROVÉHO KOLA POMOCNÉ ENERGETICKÉ JEDNOTKY

MIROSLAV SVOBODA, MARTIN TŮMA

První brněnská strojírna Velká Bíteš, a. s.

Abstract: The auxiliary power unit (APU) Safir 5K/G Z8, developed by PBS Velka Bites, a. s. (CZ), is an independent source of the electrical energy for a helicopter. The APU consists of an electric and gas generator. The gas generator is small-size gas turbine, where radial impeller, annular combustion chamber and double stage axial turbine are assembled. This paper deals with computational analysis of integral radial impeller, which is made of wrought high strength aluminum alloy. The static structural, modal, harmonic and life analyses were performed for EASA certification program by using ANSYS Workbench. Harmonic analysis was performed only informatively.

Keywords: Impeller, Stress Analysis, Low Cycle Fatigue, Natural Frequency, Resonance.

1 Úvod

Pomocná energetická jednotka (zkráceně PEJ) Safír 5K/G Z8, z produkce První brněnské strojírny ve Velké Bíteši, je používána jako autonomní zdroj energie pro vrtulníky. Primárním účelem je pohon generátoru pro dodávku elektrické energie při předletové přípravě, pro startování hlavních motorů nebo při výpadku hlavních zdrojů za letu. Dále může být využita pro dodávku stlačeného vzduchu pro klimatizační systém letounu. Skládá se z generátoru elektrické energie a generátoru plynů, což je malý turbínový motor s prstencovou spalovací komorou, dvoustupňovou axiální turbínou a jednostupňovým radiálním kompresorem.

Za účelem plnění certifikačních požadavků, stanovenými Evropskou agenturou pro bezpečnost letectví (EASA), byly provedeny příslušné pevnostní analýzy. Následující příspěvek se zabývá strukturální, modální a orientační harmonickou analýzou kompresorového kola, včetně hodnocení jeho životnosti. Integrální, radiální kolo kompresoru je vyráběno z pokročilé hliníkové slitiny, určené pro vysoce namáhané dílce. Pro zvýšení korozní odolnosti a odolnosti proti abrazivnímu poškozování od pevných částic je povrch kola elektrochemicky upraven anodickou oxidací (tzv. chromeloxem). Disponuje 12 lopatkami a 12 mezilopatkami, viz obrázek 1. Poháněno je dvojící axiálních turbín, uložených na společné hřídeli s kompresorem.
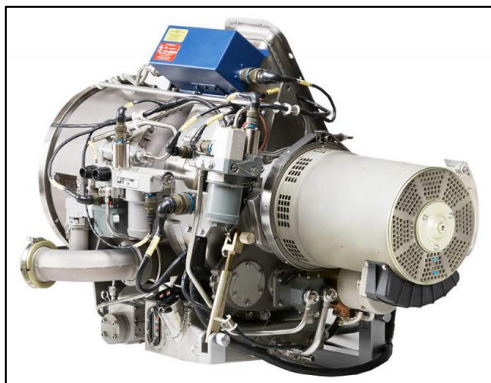
Obrázek 1 – Vlevo: Pomocná energetická jednotka; Vpravo: kompresorové kolo.

2 Výpočtové modely

Numerické analýzy byly provedeny na samostatném prostorovém modelu kompresorového kola. Modální a strukturální analýza (s navazujícím analytickým hodnocením nízkocyklové únavy) byla provedena na periodickém segmentu s jednou lopatkou a jednou mezilopatkou. Harmonická analýza byla provedena na celém prostorovém modelu. Viz obrázek 2.
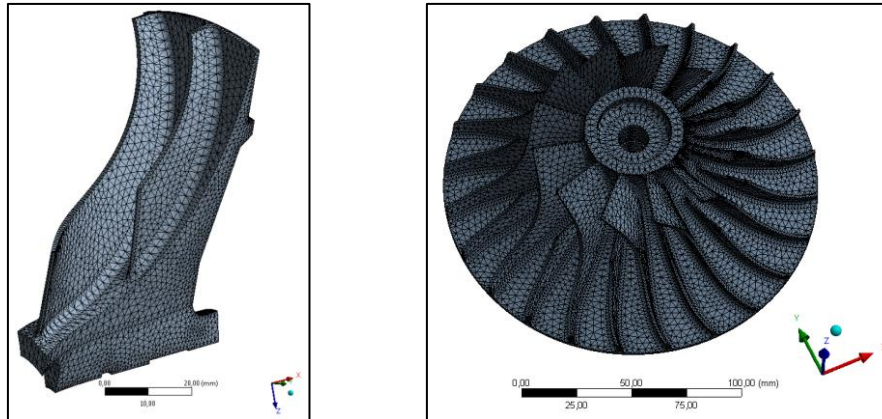
Obrázek 2 – Model geometrie kompresorového kola (vlevo periodický segment).

Strukturální analýza

Jedná se o základní pevnostní analýzu kola, zatíženého pouze odstředivými silami od rotace při maximálních provozních otáčkách PEJ, s použitím lineárního modelu materiálu. Výsledkem výpočtu je hodnocení napjatosti a deformace kola od nejdominantnějšího zatížení. Získaná napětí jsou dále použita při hodnocení nízkocyklové únavy, založené na tzv. Neuberově koncepci redistribuce napětí. Tato teorie umožňuje s technicky přijatelnou přesností stanovit z lineárního výpočtu pružně-plastickou deformaci (odpovídající cyklickému chování) ve vrubu. Je založena na předpokladu proprocionálního zatěžování a pracuje se standardními nízkocyklovými parametry materiálu, získaných z normalizovaných únavových zkoušek. Hodnocení vysokocyklové únavy bylo řešeno prostřednictvím dynamiky lopatek, resp. patřičným rozborem odpovídajících rezonančních stavů (viz dále).

Výpočtový model byl diskretizován volnou sítí, přibližně o 74 tis. tetraedrických elementech (SOLID 187). V očekávaných kritických oblastech byla síť dostatečně zjemněna. Okrajové podmínky byly aplikovány tak, že v jednom z uzlů na zadní straně disku (poblíž centrálního otvoru) bylo zamezeno natočení a axiálnímu posuvu. Na rovinách řezu segmentu byla předepsána cyklická symetrie. Samotný výpočet byl realizován v jednom zátěžném kroku. V případě hodnocení životnosti byl uvažován harmonický cyklus, reprezentující spuštění a vypnutí PEJ. Tomu odpovídá míjivé zatěžování do tahu, s konstantní amplitudou a středním napětím. Vliv středního napětí byl zahrnut prostřednictvím modifikované Manson-Coffinovy křivky dle teorie Morrow. Maximální zatížení cyklu odpovídá maximálním provozním otáčkám kompresoru.
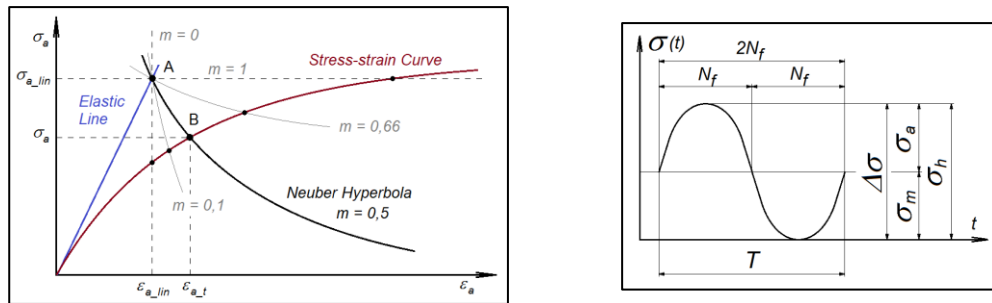
Obrázek 3 – Vlevo: Neuberova koncepce redistribuce napětí; Vpravo: Zátěžný cyklus kompresoru.

Modální analýza

Pro potřeby vyhodnocení modálních vlastností byly vytvořeny dva výpočtové modely. Jeden pro popis vetknutých lopatek, druhý pro popis vázaného kmitání disku a lopatek (tzv. olopatkovaný disk). V obou případech byl použit stejný periodický segment kola s jednou celistvou lopatkou a mezilopatkou, na kterém byla vytvořena homogenní síť. Rozdíl spočíval v aplikovaných okrajových podmínkách, kdy v případě vetknutých lopatek je na rovinách řezu zamezeno posuvu, zatímco u olopatkovaného disku byla použita cyklická symetrie. Zde bylo zamezeno posuvu v jednom z uzlů na zadní straně disku.

Analýza vetknuté lopatky je analýzou pomocnou. Slouží především k naladění modelu s experimentálně naměřenými frekvencemi pomocí vysokofrekvenčního mikrofonu a budícího kladívka (viz obrázek 4). Také pomáhá s rozlišením jednotlivých vlastních tvarů kmitání lopatky, mezilopatky a disku. Analýza celé sestavy lopatek a disku (tj. olopatkovaného disku) poskytuje nejvěrohodnější modální vlastnosti oběžného kola. Byly spočítány vlastní frekvence (cca do 20 kHz) pro všechny uzlové průměry $k_{c,h}$, jejichž maximální počet je dán vztahem

$$k_{c,h} = |c \cdot r - h \cdot s| \leq \begin{cases} \frac{r}{2} & \text{(pro } r \text{ sudé)} \\ \frac{r-1}{2} & \text{(pro } r \text{ liché)} \end{cases}, \tag{1}$$

kde h je harmonický násobek, r je počet lopatek rotoru a s počet lopatek statoru. Konstanta c (c = 0, 1, 2, …) reprezentuje rotující tvar. Dále je uvažován případ nulových (analýza bez předpětí) a maximálních (s předpětím) otáček. Získané frekvence jsou následně zpracovány do tzv. Campbellových diagramů (např. viz obrázek 8), z nichž jsou vyhodnoceny rezonanční stavy, odpovídající aerodynamickému buzení (interakce proudu vzduchu s lopatkami statoru a rotoru).
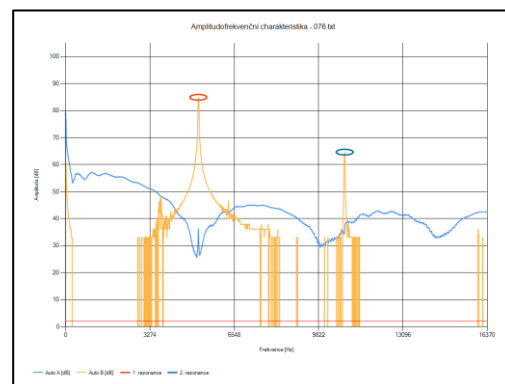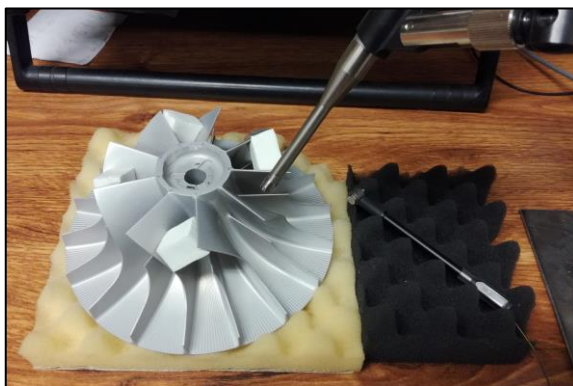

Obrázek 4 – Vlevo: Experimentální měření vlastních frekvencí; Vpravo: Výstup z měření.

Harmonická analýza

V případě harmonické analýzy byl použit celý prostorový model kompresoru, na kterém byly aplikovány jednotkové budící síly, s fázovým posunutím $\phi_{m,n}$ dle vztahu

$$\phi_{m,n} = n \cdot \varphi_s - m \cdot \varphi_r \ . \tag{2}$$

Symbol φ_s, resp. φ_r, značí úhel mezi lopatkami statoru, resp. rotoru. Rovnice (2) představuje fázový rozdíl mezi impulsem od *n*-té lopatky statoru, působícím na *m*-tou lopatku rotoru. Byly přitom uvažovány dva případy vynuceného kmitání (resp. dvě kombinace rotorových a statorových lopatek), označené jako vstupní a výstupní strana kompresorového kola. V obou případech byly budící síly aplikovány tangenciálně, vždy do uzlu na příslušnou špičku lopatky, resp. mezilopatky (viz obrázek 5). Hodnota proporcionálního tlumení byla zvolena na 0,1 %.
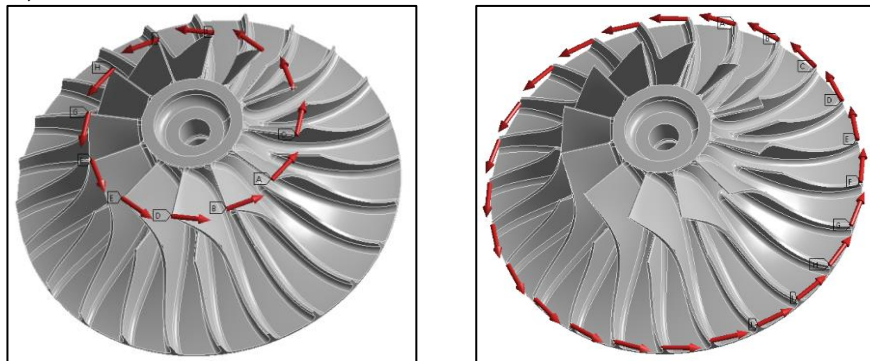

Obrázek 5 – Definice budících sil harmonické analýzy: vstupní (vlevo) a výstupní (vpravo) strana kompresorového kola.

Snahou harmonické analýzy bylo posoudit vliv buzení lopatek kompresorového kola na vynucené kmitání od počtu lopatek difuzoru nebo žeber v sání. Výstupem výpočtu jsou frekvenčně-amplitudová spektra (např. viz obrázek 9), přičemž hlavní oblastí zájmu byly provozní a stabilizační (stabilizace hoření při startu) otáčky PEJ. Výpočty byly provedeny s homogenní sítí, metodou Mode Superposition, bez předpětí a s lineárním frekvenčním krokem.

3   Vyhodnocení

Prostřednictvím elastické strukturální analýzy bylo hodnoceno ekvivalentní napětí ve třech kritických oblastech kola. Konkrétně na lopatce, v centrálním otvoru a v přechodovém rádiu na zadní straně disku. Ve všech třech případech nepřesáhla hodnota napětí minimální smluvní mez kluzu použitého materiálu. Nejnižší bezpečnost byla stanovena na lopatce, viz obrázek 6. Dále byly hodnoceny radiální a axiální deformace, především na vnějším meridiánu lopatek. Z výsledků vyplývá, že během provozu nehrozí riziko vymezení navržených vůlí mezi rotorem a statorem. Z hlediska statické pevnosti bylo kompresorové kolo shledáno jako vyhovující.

Jak již bylo popsáno výše, životnost je posuzována prostřednictvím výpočtového odhadu nízkocyklové únavy, která je porovnávána s jinými, podobnými aplikacemi. Důvodem jsou především zjednodušující předpoklady analytického výpočtu a dosavadní absence jeho relevantních verifikací. Zkušenosti i dlouhodobé zkoušky totiž potvrzují, že životnost PEJ jako celku je zpravidla omezena jinými součástmi, resp. konstrukčními celky. U zde posuzovaného kola byla pro výše definovaný cyklus stanovena nejnižší výpočtová životnost 24 000 cyklů na přechodovém rádiu zadní strany disku (technickou specifikací PEJ je požadováno min. 6 000 startů). Pro daný produkt se jedná o hodnotu v běžně počítaných mezích. V centrálním otvoru byl zjištěn o dva řády vyšší počet a na lopatce vzniká vlivem deformace napětí tlakové.
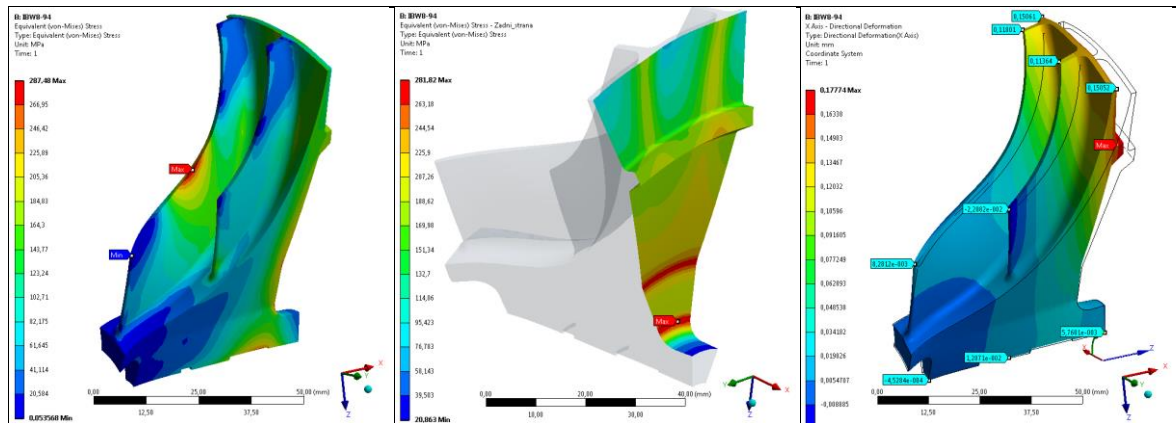
Obrázek 6 – Vlevo a uprostřed: Vyhodnocení ekvivalentního napětí; Vpravo: Vyhodnocení radiální deformace.

Prostřednictvím modální analýzy vetknuté lopatky byly identifikovány a roztříděny vlastní tvary kmitání lopatky a mezilopatky od kmitání disku (viz obrázek 7), který není prostřednictvím aerodynamického buzení reálně vybuditelný. Počet skutečně vybuditelných tvarů (tzn. uzlových průměrů $k_{c,h}$) je dále omezen kombinací statorových a rotorových lopatek podle rovnice (1). Standardně se uvažuje první a druhý harmonický násobek h pro tři rotující tvary (tři konstanty c, nejbližší poměru s/r). U hodnoceného kola vychází dva, tři a pět uzlových průměrů (opět jsou uvažovány kombinace lopatek pro vstupní a výstupní stranu kompresoru).

Vypočtené frekvence, které přísluší výše určeným uzlovým průměrům, byly zpracovány do Campbellových digramů (např. viz obrázek 8), zobrazující závislost vlastní frekvence na otáčkách. Pravděpodobné rezonanční stavy jsou následně identifikovány průsečíkem vlastní frekvence a tzv. náběhové přímky, která je $h \cdot s$ násobkem otáčkové frekvence. Snahou je vyhnout se těmto rezonancím v blízkosti provozních (a jiných důležitých) otáček PEJ. V opačném případě dochází k ulomení lopatek vlivem vyčerpání vysokocyklové životnosti. U hodnoceného kola byly posuzovány provozní a stabilizační otáčky (stabilizace hoření při startu), v jejichž bezprostředně blízkém okolí nebyly rezonance nalezeny. Kolo je z hlediska modálních vlastností vyhovující.
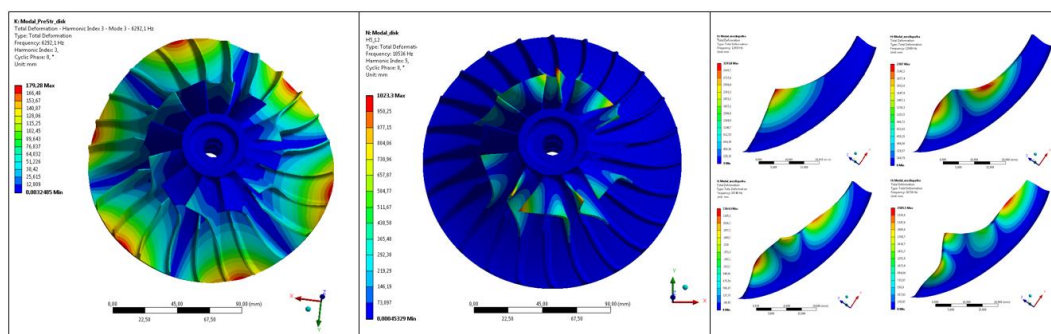
Obrázek 7 – Ukázka vlastních tvarů kmitání: disk (vlevo), lopatka (uprostřed), mezilopatka (vpravo)
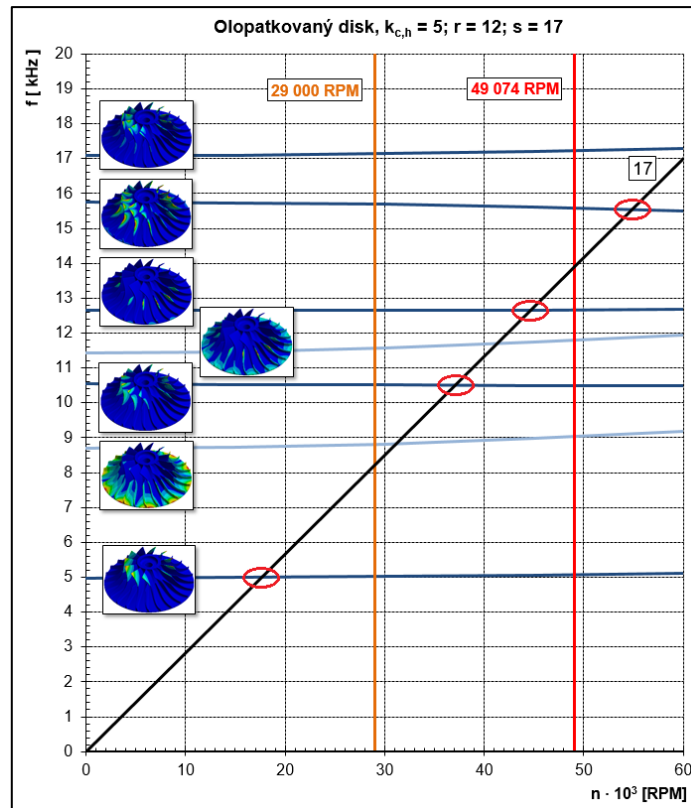
Obrázek 8 – Campbellův rezonanční diagram (pět uzlových průměrů, výstupní strana kompresoru).

Pro posouzení vlivu buzení lopatek kompresoru byla provedena harmonická analýza. Průběhy výchylek a napětí byly zjišťovány na třech po sobě jdoucích lopatkách a mezilopatkách. Výsledkem jsou frekvenčně-amplitudové charakteristiky, viz obrázek 9 (výstupní strana kola). Z grafů je patrných pět potenciálních rezonancí, přičemž pouze tři jsou poměrově výraznější. Absolutní hodnotu amplitudy nelze v tomto případě uvažovat. Důvodem je např. neznalost reálné budící síly, která byla mj. ve výpočtech uvažována konstantní v celém frekvenčním spektru. Také skutečná hodnota tlumení není známa.

U obou uvažovaných variant, tzn. vstupní i výstupní strany kompresoru, bylo identifikováno několik výrazných rezonancí, vyskytujících se mimo důležité otáčkové hladiny PEJ. Ty jsou při jejím startu rychle přejížděny, tudíž nepředstavují zásadní riziko. V oblasti stabilizace hoření nebo provozu kompresorového kola nebyly nalezeny rezonance, které by měly ohrozit jeho provozuschopnost.
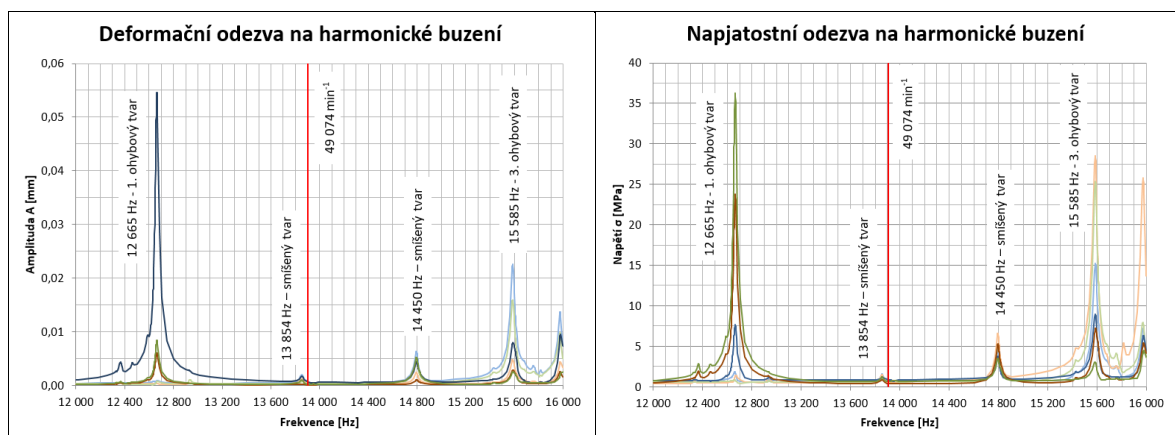
Obrázek 9 – Frekvenčně-amplitudové charakteristiky pro případ výstupní strany kompresoru.

4   Závěr

V krátkosti byla představena pevnostní numerická kontrola radiálního kompresorového kola, rozdělená do tří základních oblastí. S nejběžnější statickou kontrolou nejsou většinou velké potíže. Hodnocené kolo zpravidla vychází z ověřeného návrhu, který je modifikován změnou lopatkování, jak z pohledu geometrie (tloušťky, zakřivení, apod.), tak z pohledu počtu lopatek. Takové změny mají zásadní vliv především na dynamické chování, tudíž této oblasti je věnována větší pozornost.

Dynamická kontrola byla řešena skrze aerodynamické buzení, vznikající interakcí proudu vzduchu s lopatkami statoru a rotoru. Z modální analýzy bylo získáno poměrně velké množství vlastních frekvencí a vlastních tvarů kmitání. Reálně je však vybuditelná pouze část, přitom některé jsou více a některé méně nebezpečné. Z tohoto důvodu byla provedena harmonická analýza, jejíž snahou bylo porovnat velikosti amplitud jednotlivých potenciálních rezonančních stavů. Výsledkem analýz je závěr, že v oblasti důležitých otáček PEJ se nenachází nebezpečné rezonance. Toto tvrzení je samozřejmě patřičně ověřováno náležitými zkouškami celé PEJ.

Dále bylo kolo hodnoceno z pohledu nízkocyklové únavy, prostřednictvím známých a dostupných teoretických vztahů. Odhadovaný počet cyklů byl stanoven několikanásobně nad rámec garantovaných počtů startů PEJ.

Ve výsledku bylo kompresorové kolo shledáno jako vyhovující. V současné době bylo vyrobeno 80 kusů. Prezentované analýzy byly použity pro plnění certifikačních pažadavků civilního letectví podle CS-APU 300 (Vibrace) a CS-APU 310 (Omezení životnosti).

Literatura

KAMENICKÝ, J., 1989. *Konstrukce leteckých motorů: Pevnost a dynamika.* Část 2.. Brno: Vojenská akademie, 448 stran. Č. tisku: U-781/2.

KUSHNER, F., 2000. Critical Review of Compressor Impeller Vibration Parameters For Failure Prevention. In.: *Proceedings of the 29th Turbomachinery Symposium*, Texas A&M University. Turbomachinery Laboratories. Dostupné z: https://doi.org/10.21423/R1F959.

LEE, Y., 2005. *Fatigue testing and analysis: Theory and practice.* Boston: Elsevier Butterworth-Heinemann, 402 stram. ISBN 0-7506-7719-8.

STATEČNÝ, J., 1991. *Pevnost a životnost leteckých turbínových motorů, část II*. Praha: České vysoké učení technické, 172 stran.

Kontaktní adresa:
Ing. Miroslav Svoboda
První brněnská strojírna Velká Bíteš, a. s., Vlkovská 279, 595 01, Velká Bíteš, Česká republika
Ing. Martin Tůma
První brněnská strojírna Velká Bíteš, a. s., Vlkovská 279, 595 01, Velká Bíteš, Česká republika

INFLUENCE OF THE TEMPERATURE IN THE VENTILATED DOUBLE-SKIN TRANSPARENT FAÇADE

MAREK MACÁK[1], BORIS BIELEK[2]

[1]Department of Mathematics and Descriptive Geometry, Slovak University of Technology in Bratislava, Faculty of Civil Engineering, Radlinského 11, 810 05 Bratislava

[2]Department of Building Construction, Slovak University of Technology in Bratislava, Faculty of Civil Engineering, Radlinského 11, 810 05 Bratislava

Abstract: The paper deals with the Computational Fluid Dynamics (CFD) modelling of the double-skin transparent façade. In CFD simulation of double-skin transparent façade we study the change in air temperature from external influences like as radiation. The air momentum is defined by suction power of the air heat pump. In our study we have performed simulation for a cavity of a 4-storey double-skin transparent façade.

Keywords: computational fluid dynamics, double-skin transparent façade, Realizable $k - \varepsilon$ model, solar energy

1. Introduction

The technology of building façades is determined by architectural trends and the development of technology itself, societal requirements and other factors. The design of modern wall claddings is driven by climate-specific contexts on one hand and on the other in response to regulatory and social aspects governing the quality of work environments. Ecological, low-energy architecture with automated control systems for environmental, energy, security, transport, communication and information processes is also finding a home in facade technology that uses environmentally-friendly renewable energy sources that are in line with the concept of sustainable development of the European construction industry.

The double-skin transparent façade concept is one of the types of the facade technology of buildings that uses environmentally-clean alternative source of solar energy; although the concept is not completely new, the growing tendency to use these facades in architectural design, especially in Europe, cannot be denied (Bielek, 2002). In addition, double-skin facades, historically speaking, have been used more often in European architecture than in the United States. This is probably due to significantly higher energy prices in Europe and a traditionally higher concern for ecology and the enviroment.

From a technical point of view, development of modern double-skin transparent facades is based on the physical theory of cavities, which allows for a wide range of modifications, e.g., in cavity geometry or in the types of glazing systems used (Bielek, 2002).

This paper presents computational fluid dynamics (CFD) for double-skin transparent façade concept modeling efects of radiation and air flow due to air pump. First, in Section 2 we describe equations for temperature and turbulent model. Section 3 deals with the CFD simulation, computational domain, mesh setting and boundary conditions. In Section 4, we present obtained results. Finally, Section 5 concludes the paper.

2. Applied equation for simulations

These assumptions were considered: steady-state flow, Newtonian fluid, incompressible turbulent flow, constant physical properties and sun radiation. This assumptions leads to these equations. Namely:

Continuity equations:

$$\nabla . \rho \boldsymbol{u} = 0, \qquad (1)$$

Momentum equations:

$$\rho(\boldsymbol{u}. \nabla \mathbf{u}) = -\nabla p + \mu \nabla^2 \boldsymbol{u}, \qquad (2)$$

Energy equations:

$$\rho c_p(\boldsymbol{u}. \nabla \mathrm{T}) = \lambda \nabla^2 T, \qquad (3)$$

where $\boldsymbol{u}$ is velocity [*m/s*], ρ is density [*kg/m³*], μ is viscosity [*Pa.s*], c_p is specific heat [*J/kg.K*], λ is thermal conductivity [W/m.K] and T is temperature[*°C*].

Form turbulence modelling we use the two-equation Realizable $k - \boldsymbol{\varepsilon}$ model (Wilcox, 2006) with transport equations formulated as:

$$\nabla . \left[\rho k \boldsymbol{u} - \left(\mu + \frac{\mu_t}{\sigma_k}\right)\nabla k\right] = P_k + P_b - \rho\varepsilon - Y_M + S_k, \qquad (5)$$

$$\nabla . \left[\rho \varepsilon \boldsymbol{u} - \left(\mu + \frac{\mu_t}{\sigma_k}\right)\nabla \varepsilon\right] = \rho C_1 S_\varepsilon - C_2 \rho \frac{\varepsilon^2}{k+\sqrt{\upsilon\varepsilon}} - C_{1\varepsilon}\frac{\varepsilon}{k}C_{3\varepsilon}P_b + S_\varepsilon, \qquad (6)$$

where k is turbulent kinetic energy in [*m²/s²*], ε is turbulent dissipation rate in [*m²/s³*], μ_t is turbulent dynamic viscosity in [*kg/m.*s], P_k is generation of the kinetic turbulence energy due to the mean speed gradient, P is generation of the kinetic turbulence energy due to the lift, Y_M is increase from fluctuation in compressible turbulent flow to overall dissipation, $C_1 = max\left[0.43\frac{\eta}{\eta+5}\right]$, C_2, $C_{1\varepsilon}$, $C_{3\varepsilon}$ are model constants, σ_k and σ_k are Prandtl numbers for k and ε, S_k and S_ε are user-defined source term.

All equations were integrated using a commotional CFD package ANSYS Fluent (Ansys, 2018) which use finite volume method (Eymard, 2001).

3　Numerical simulation

For the simulations we have used program ANSYS Fluent (Ansys, 2018).

3.1 Computational domain and mesh

In our simulation of double-skin transparent façade we chose a model with the thickness of the cavity of 800 mm, and the length of a section of the façade 6 x 1250 mm = 7500 mm. The height of the model corresponds to 4 storeys (4 x 3450 mm), as shown in Image 1.

The exterior glazing of the double-skin façade, which influences the energy gains of the façade most significantly, is modelled as a simple tempered glass with the thickness of 12 mm. Material properties was λ thermal conductivity 1 [W/m.K], absorption 34% and total solar energy transmittance 70%. The inner transparent wall consists of aluminium windows with triple glazing. Material properties was λ thermal conductivity 0.7 [W/m.K], absorption 20% and total solar energy transmittance 45%. The opaque wall of the building was modled with concrete parapet wall λ = 1.5 [W/m.K] ,thermal izolation λ 0.03 [W/m.K] and aluminium sheet cassette (λ = 202.4 [W/m.K]). At the level of each floor, the aluminium floor grid (λ = 202.4 [W/m.K]) with an effective area of 70% is mounted along the entire façade.

Mesh was generated using CutCell elements. The maximal element size was set 2 cm. All other settings were left on default. Generated was 2 492 692 elements with 2 933 091 nodes.
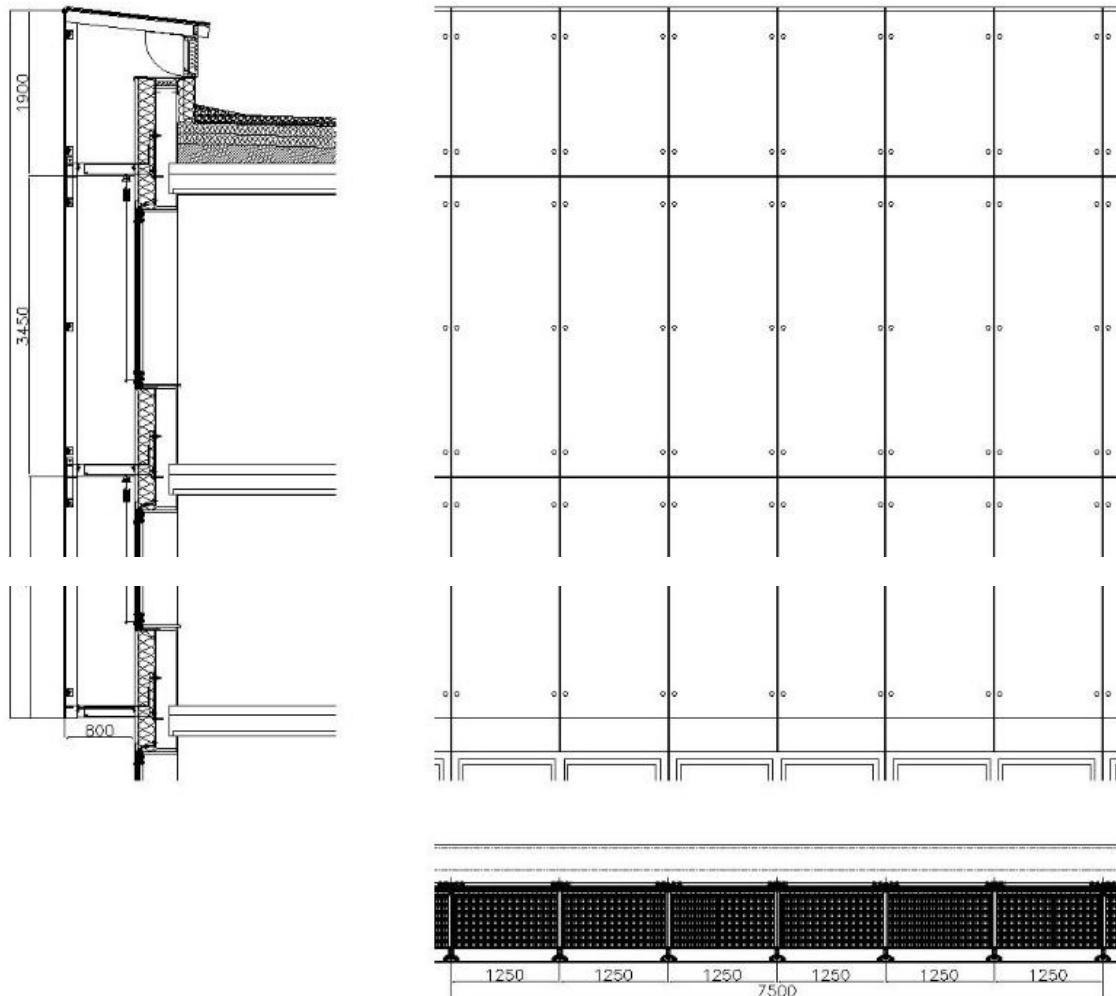

Image 1 – Design of the double-skin transparent façade.

3.2 Boundary conditions

Our computations include fluid and thermal simulations. Therefore, we explain each case individually.

2.3.1   Fluid conditions

At the construction is an air intake opening at the bottom of the cavity. On this area we set mass flow inlet as boundary condition. At the highest level of the cavity in the centre there is an air outlet through an opening with the dimensions 700 x 355 mm and the area of approximately 0.25 m^2. On this area we set mass flow outflow as boundary condition. We are investigated in these air flows rates 50, 100, 150, and 200 m^3/min (real air flow rates for heat pumps with primary energy of air).

3.2.2   Thermal conditions

For whole model we prescribe intensity of solar radiation at four levels of 150, 300, 450 and 600 W/m^2accodring to climate data in area of Bratislava. On the interior rooms behind the facade we set temperature of +20.0°C with heat transfer coefficient 4 W/m^2K. The outside boundary condition of the façade we set temperature of the exterior air -11.0°C

with heat transfer coefficient 25 W/m^{2}K. Solar boundary conditions (absorptivity, transmissivity) was set according to material properties describer in section 3.1.

3.3.3 Solution setting

All simulations ran as pressure-based, steady, without production limiter and curvature correction. From solution methods there was used SIMPLE pressure-velocity coupling scheme with the second order spatial discretization. Solution was initialized with the hybrid initialization. The simulations were done when scaled residuals reached the minimum values: 10^{-4} all quantities. The simulations were performed using parallel processing on a desktop computer with one Intel Core i7-8700K 3.7 GHz processor and 64 GB DDR4 memory.

4   Results and discussion

We have performed computations for every radiation intensity and flows rates. We presented results for the mean temperature in air outlet through an opening with the dimensions 700 x 355 mm at the highest level of the cavity. In Table 1 we can see values of mean air temperature in the outflow of double-skin transparent façade for different intensity of radiation and air flow. For better illustration we present results also in graph, see Image 2. In Image 3 we can see illustration of stream lines for different air flow and radiation intensity. We can see that the air temperature in outlet increases by rise of intensity of radiation and decreases by the higher rate of change of air in cavity. These results fulfilled our expectations but to confirm these values we have to do experimental measurement in situ.

Table 1 The mean air temperature in the outflow of double-skin transparent facade as a function of the intensity of the solar radiation and the air flow through the cavity.

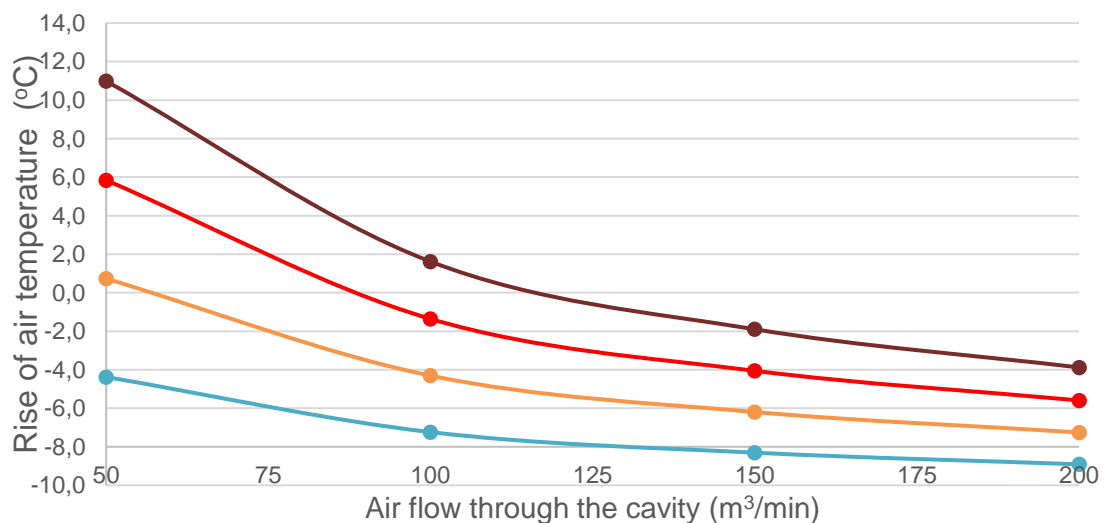| Air flow (m³/min)	Radiation (W/m2)			
	150	150	150	150
50	-4,38	0,73	5,84	10,99
100	-7,24	-4,31	-1,36	1,62
150	-8,30	-6,19	-4,05	-1,90
200	-8,91	-7,25	-5,59	-3,88

Image 2 – The mean air temperature in the outflow of double-skin transparent facade as a function of the intensity of the solar radiation and the air flow through the cavity

Image 3 – Illustration of streamlines a) Radiation 150 (W/m2) and air flow 50 (m3/min), a) Radiation 450 (W/m2) and air flow 150 (m3/min).

5   Conclusion

We have presented a study of concept of a two-stage system to utilize solar energy to preheat the primary air for an air heat pump. The computer simulations have shown that by thermal conditioning of the outside air in the cavity of a double-skin facade it is possible to substantially increase the temperature of the primary air for the heat pump. The difference between the temperature of fresh outside air and the temperature of thermally conditioned air at the outlet from the cavity was ranging from 4 °C up to 23 °C depending on air speed and radiation intensity.
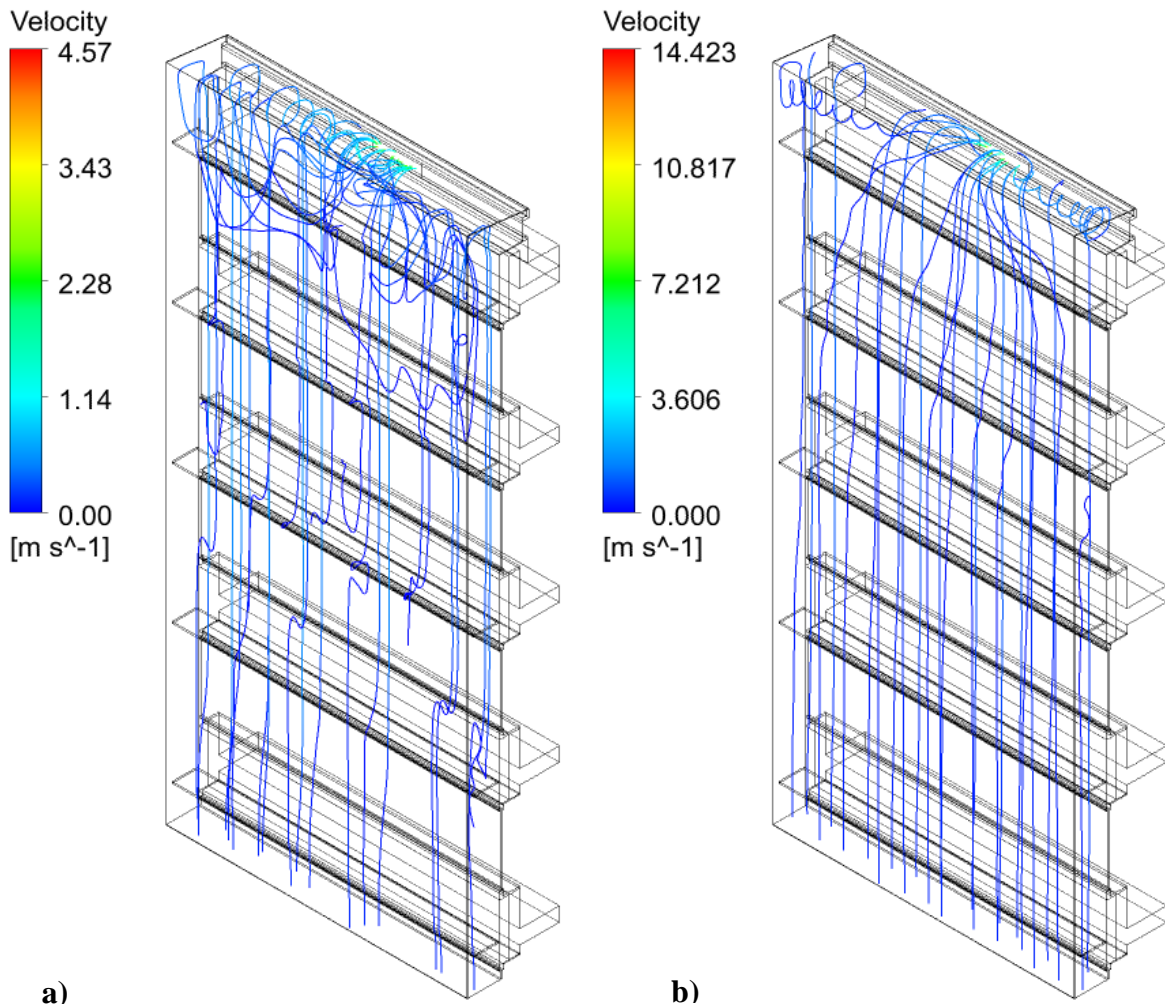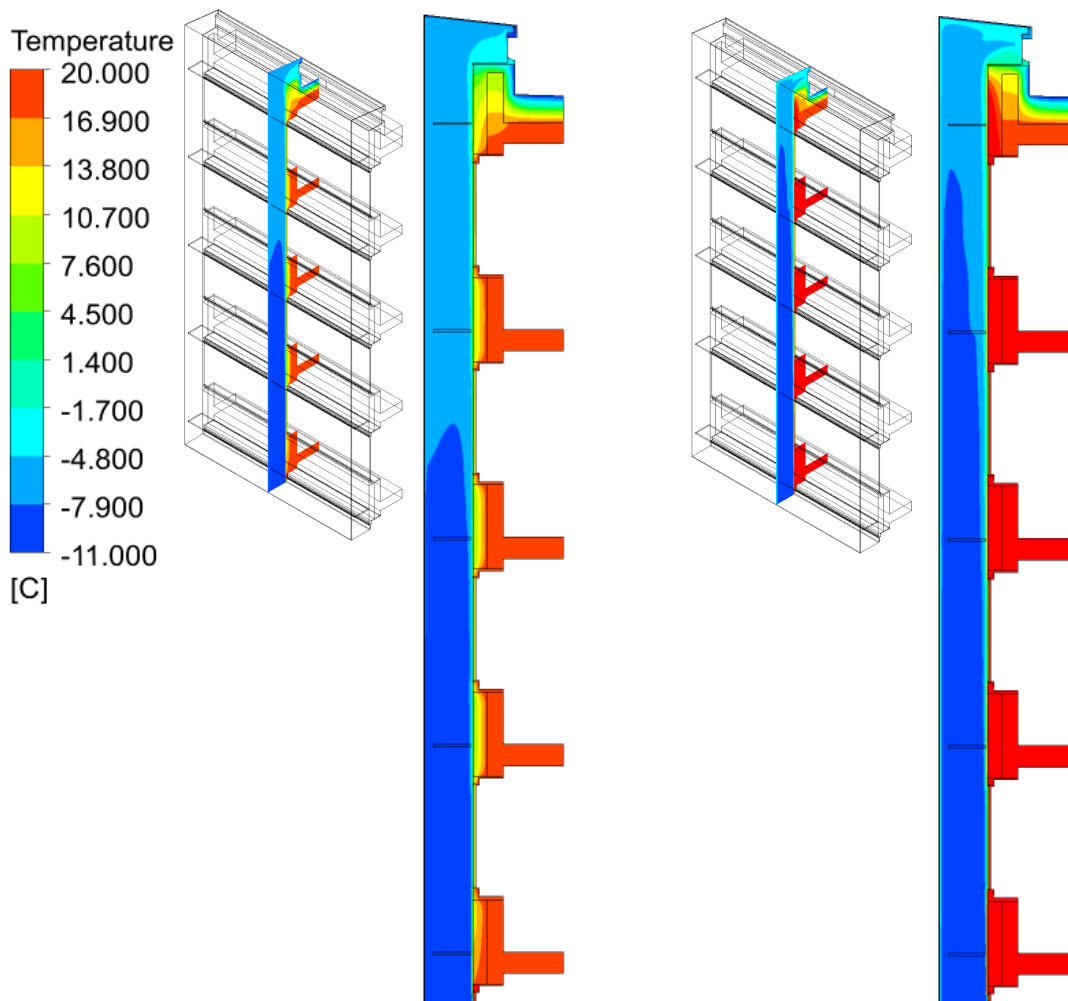
Image 4 – Illustration of air temperature a) Radiation 150 (W/m2) and air flow 50 (m3/min), a) Radiation 450 (W/m2) and air flow 150 (m3/min).

References

ANSYS Inc., 2018, ANSYS Fluent Theory Guide, Release 19.1

BIELEK, B., BIELEK, M. AND PALKO M., 2002, Double-skin transparent facades of buildings, Coreal, Bratislava.

EYMARD, R., GALLOUET, T. AND HERBIN, R., 2001, Finite volume approximation of elliptic problems and convergence of an approximate gradient, Applied Numerical Mathematics, 37, 1 - 2, 31- 53.

WILCOX, D.C., 2006, *Turbulence modeling for CFD*, 3rd edition. Journal of Fluid Mechanics [online], vol. 289, pp. 460. ISSN 0022-1120. Available on: DOI: 10.1017/S0022112095211388

Acknowledgement

Contact address:
Ing. Marek Macák, PhD.
Slovak University of Technology in Bratislava, Faculty of Civil Engineering, Department of Mathematics and Descriptive Geometry, Radlinského 11, 810 05 Bratislava, Slovakia
E- mail: marek.macak@stuba.sk

prof. Ing. Boris Bielek, PhD.
Department of Building Construction, Slovak University of Technology in Bratislava, Faculty of Civil Engineering, Radlinského 11, 810 05 Bratislava
E - mail: boris.bielek@stuba.sk

A CFD APPROACH AS A BASE WIND STUDY OF PRESSURE DISTRIBUTION ON THE COMPLEX BUILDINGS

MICHAL FRANEK[1], MAREK MACÁK[2], OĽGA HUBOVÁ[3]

[1]Department of Building Construction, Slovak University of Technology in Bratislava,
Faculty of Civil Engineering,
Radlinského 11, 810 05 Bratislava
[2]Department of Mathematics and Descriptive Geometry, Slovak University of Technology
in Bratislava, Faculty of Civil Engineering,
Radlinského 11, 810 05 Bratislava
[3]Department of Structural Mechanics, Slovak University of Technology in Bratislava,
Faculty of Civil Engineering,
Radlinského 11, 810 05 Bratislava

Abstract: Evaluation and quantification of the wind effect on the real urban structures is very complex challenge. It has to be taking into account the approaching wind conditions, surroundings structures and geometrical accuracy of the testing model. The present article focuses on the solving this issue with an integrated numerical and experimental approach. Calibrated numerical model based on Computational Fluid Dynamics (CFD) help us to understand the wind effects and critical areas, which were solved closely with experiment. Experimental part was planned in Boundary Layer Wind Tunnel (BLWT) in Bratislava at a reduced scale models including the surroundings topography and buildings.

Keywords: computational fluid dynamics, boundary layer wind tunnel, case wind study, external pressure coefficient, ansys fluent

1 Introduction

For complex understanding and quantification of wind effects on structures it is offered various approaches. It could be used the in Situ measurement, experimental or numerical approach. Each has advantages and disadvantages. Using only one approach can cause the underestimation or failure. Therefore it is necessary to use the integrated approach. It must be pointed out that each of them is evolving, expecially the numerical simulations. Development of simulation models work hand in hand with accurate experimental tests. Field of research that deal with development of numerical simulations of wind effects on Civil Engineering is called Computational Wind Engineering (CWE). It is based on Computational Fluid Dynamics (CFD). CWE study properties of natural wind in the lower part of the atmospheric boundary layer (ABL) (0 – 200 m) where occurs to turbulence. Correct definition of the turbulence is difficult. Better express of turbulence is as a list of properties and attributes. It contains diffusivity, vorticity, randomness, scale spectrum, 3D structure, dissipation and non – linearity. Comprehensive reviews have been published (Stathopoulos, 1997; Reichrath and Davies, 2002; Blocken and Carmeliet, 2004).

Aim of this contribution was to used numerical simulation as prediction method to localize the critical pressure zones which are important due to the design of façade system. Pedestrian comfort was evaluated too. Simulation show us zones where the wind effect is major and reduce the measuring time and probes in wind tunnel.

2   Numerical simulation

Correct simulation is obtained with accurate and reliable predictions of atmospheric processes. Flow profiles are characterized by mean wind speed and turbulence quantities at the inlet zone of the computational domain. These profiles are represented by the roughness characteristics of the upstream terrain. Roughness of the approach terrain is included in the computational domain for better catch of the ABL. For accurate results from simulation it is necessary to achieve the similarity of the ABL and measuring models. Our study is focused on using the calibrated numerical model (Franek et al., 2016) as a preliminary wind analysis.

It was chosen the finite volume method implemented under program ANSYS Fluent (Ansys, 2017). There are several turbulence models in Fluent. All computations were ran as pressure – based, steady, without production limiter. From solution methods was used SIMPLE pressure-velocity coupling scheme with second order spatial discretization, for transient formulation was used second order implicit method. Solution was initialized with hybrid initialization with default setting.

2.1 Turbulence model

For our computation it was chosen RANS Realizable $k – \varepsilon$ model. It is two equations model where the solution of the turbulent dynamic viscosity in the Bussinesque hypothesis is solved with two separated transport equations and it can determine the turbulent kinetic energy k and turbulent dissipation ε. The first transported variable is turbulent kinetic energy k. The equation for solving is formulated as

$$\frac{\partial}{\partial t}\left(\rho k\right)+\frac{\partial}{\partial x_i}\left(\rho k u_i\right)=\frac{\partial}{\partial x_j}\left[\left(\mu+\frac{\mu_t}{\sigma_k}\right)\frac{\partial k}{\partial x_j}\right]+P_k+P_b-\rho\varepsilon-Y_M+S_k. \tag{3}$$

The second transported variable is the turbulent dissipation ε. The equation is characterized as

$$\frac{\partial}{\partial t}\left(\rho\varepsilon\right)+\frac{\partial}{\partial x_i}\left(\rho\varepsilon u_i\right)=\frac{\partial}{\partial x_j}\left[\left(\mu+\frac{\mu_t}{\sigma_\varepsilon}\right)\frac{\partial\varepsilon}{\partial x_j}\right]+\rho C_1 S_\varepsilon-C_2\rho\frac{\varepsilon^2}{k+\sqrt{\upsilon\varepsilon}}-C_{1\varepsilon}\frac{\varepsilon}{k}C_{3\varepsilon}P_b+S_\varepsilon \tag{2}$$

where u is the wind speed [m/s], t is time [s], k is the turbulent kinetic energy [m^2/s^2], ε is turbulent dissipation [m^2/s^3], ρ is the density [kg/m^3], μ_t is the turbulent dynamic viscosity [kg/m·s], v is the kinematic viscosity [m^2/s], σ is the turbulent Prandtl number [-], P_k is generation of the turbulent kinetic energy k due to the gradient of mean velocity [-], P_b is generation of the turbulent kinetic energy k due to the drag forces [-], Y_M is the addition of turbulent dilatation [-], $C_{1\varepsilon}$, $C_{2\varepsilon}$, $C_{3\varepsilon}$ are empirical constants [-], S_k and S_ε are the user defined values.

2.2 Computational domain

The size of the computational domain was created according to maximum value of blockage ratio, which is maximum 3 % (Franke et al., 2007; Tominaga et al., 2008). In our case it was 2.65 × 1.6 × 0.6 km^3 (L × W × H). The distance from the investigated models to the inlet, sides and top of domain boundaries is at least eleven times bigger as the characteristic length, according to Franke et al. (2007) and Tominaga et al. (2008).

In our computational domain, generally three different region can be significant as it is illustrated in Image 1. First zone is central where the actual obstacles (buildings, construction, etc.) are modelled explicitly with their geometrical shapes. Second and third zones are the upstream and downstream region, where the obstacles are modelled

implicitly, their geometry is not included but their effect on flow is modelled in terms of roughness (Blocken et al., 2007).
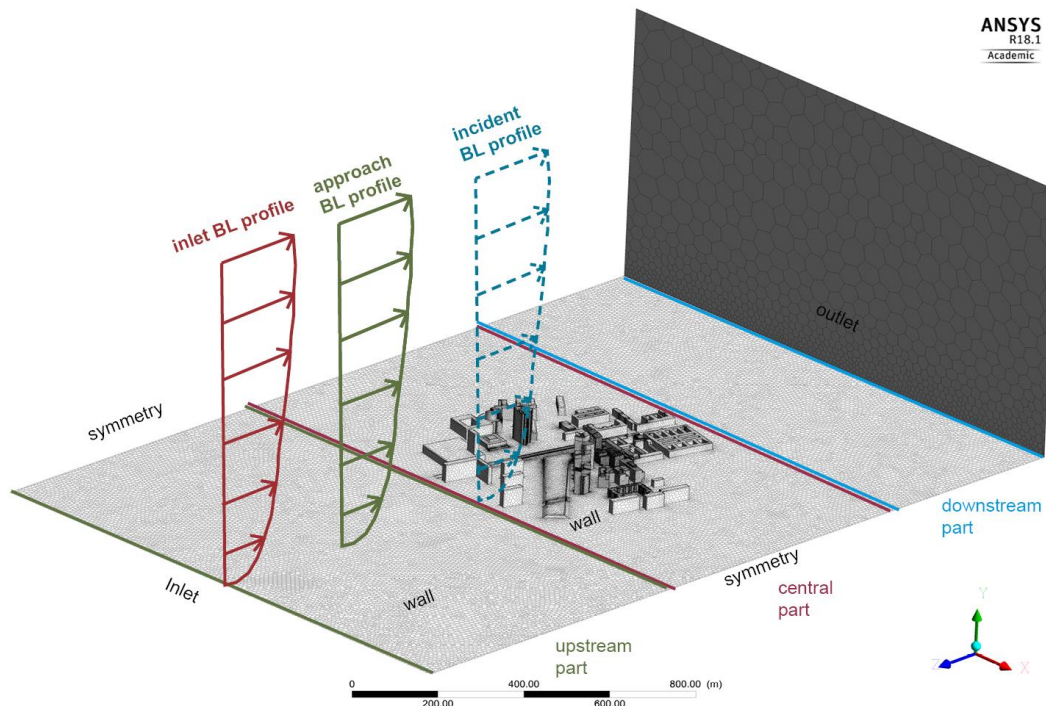

Image 1 – Computational domain with boundary conditions

2.3 Computational grid (Mesh)

Mesh was created with size function set on a distance using polyedral elements. The element size on surface of the investigated building was 0.3 m with soft behaviour using curvature function. Inflation for these surfaces was applied with 5 layers with the height of the first layer 0.4 m. The element size on surfaces of the surrounding buildings was 3 m with soft behaviour using curvature function. The element size on another surfaces was 10 m with soft behaviour using distance and curvature function. On bottom boundary was applied inflation with 5 layers with the height of the first layer 0.4 m according to Blocken et al., (2007). It was generated 4 845 975 nodes. Computational grid is illustrated in Image 2.

2.4 Boundary conditions

The inlet boundary conditions of the domain are defined by the vertical profiles

$$v(z) = \frac{v^*}{\kappa} \ln \frac{z + z_0}{z_0} \quad , \tag{3}$$

$$v^* = \frac{v_{ref} \kappa}{\ln \frac{z_{ref} + z_0}{z_0}} \quad , \tag{4}$$

where $v(z)$ is mean wind velocity at height z, v^* is shear velocity, z_0 is aerodynamic roughness length ($z_0 = 0.7$), κ is von Kármán constant ($\kappa = 0.42$), v_{ref} is the reference wind speed, which for external pressure evaluation was chosen according to the Eurocode with National Annex (STN EN 1991-1-4, 2007) 25 m/s in reference height 10 m. For pedestrian comfort it was 10 m/s in reference height 100 m.

http://aum.svsfem.cz

Turbulence in the inlet area in computational domain was derived from equations

$$k = \frac{u^{*2}}{\sqrt{C_\mu}} \,, \tag{5}$$

$$\varepsilon(z) = \frac{u^{*3}}{\kappa(z + z_0)} \,, \tag{6}$$

where C_μ = 0.09. These boundary conditions fullfil the similarity of the mean velocity and turbulence profile with BLWT Bratislava (Hubová and Lobotka, 2014) and urban exposure terrain in location of investigated building.

On the surface of approach terrain and models it was applied the roughness. Due to the fact that real buildings and structures are rough and the approach terrain too. Application of the roughness on the approach terrain is important for fully developed ABL and generation of the adequate turbulence. The equation of roughness height is defined as

$$k_s = \frac{9{,}793 \; z_0}{C_s} \,, \tag{7}$$

where k_s is equivalent sand-grain roughness height [m], C_s is roughness constant [m]. For our case of simulation it is recommended to use C_s equal to 1.0 (Blocken et al., 2007).

Conditions on the boundaries are illustrated in Image 1. In the inlet part was used the similarity with ABL profile, outlet area was modelled as pressure outflow and on the side walls it was used symmetry conditions with zero gradient.
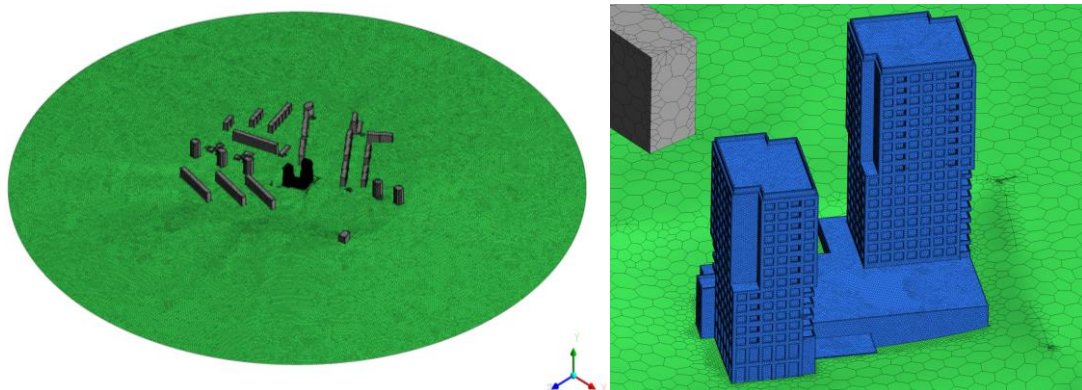

Image 2 – Illustration of the coumputational grid

2.5 Results from simulation

Because of many simulations during the case study, the results are summarized in Table 1. Only maximum and minimum value of pressure for various wind directions are shown. As you can see from Table 1, the major effect has the minimum value of pressure. It meas that the wind load which building is subjected, has the negative value. This suction has to be consider for design of the façade system. Minimum pressure was obtained on the roof part, especially near the parapet and on the corner zone where the separation of vortices occur. Illustration of pressure distribution for wind direction 330 ° is in Image 3.

Table 2 Maximum and minimum value of pressure from simulation

| Wind direction [°]	Max. pressure [Pa]	Min. pressure [Pa]	max c_{pe} [ ]	min c_{pe} [ ]
0	219.04	-728.15	0.21	-0.69
30	78.87	-172.85	0.08	-0.16
60	631.37	-890.27	0.60	-0.85
90	799.72	-774.93	0.76	-0.74
120	968.97	-738.40	0.92	-0.70
150	919.82	-815.47	0.88	-0.78
180	841.80	-1 123.13	0.80	-1.07
210	764.80	-1 310.30	0.73	-1.25
240	445.57	-1 018.86	0.42	-0.97
255	463.24	-942.84	0.44	-0.90
270	396.49	-901.53	0.38	-0.86
285	161.73	-438.16	0.15	-0.42
300	429.49	-991.61	0.41	-0.94
330	611.39	-1 400.64	0.58	-1.33
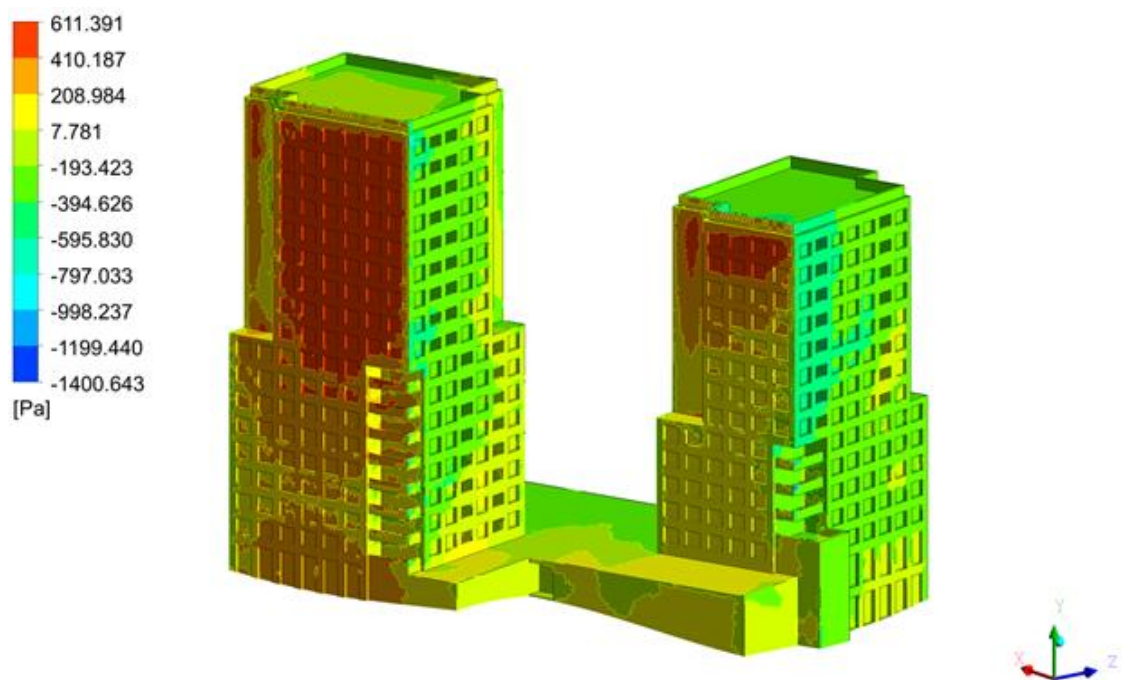
Image 3 – Pressure distribution for wind direction 330 °

3 Experimental measurement

After numerical case study the tunnel test campaign was planned on the reduced scale of 1/300th model including the surrounding topology. Taking into account the numerical results and critical areas it was identified the zones where probes and tubes were located on model and interested areas. Tests were carried out in a Boundary Layer Wind Tunnel of Slovak University of Technology in Bratislava. It is named Low Speed Boundary Layer Wind

http://aum.svsfem.cz

Tunnel with open circuit and works on negative pressure principle. The test section is 2.6 m wide, 1.6 m height and 26.3 m length. ABL is generated by barrier and uniformly roughness field. Height of the barrier was 150 mm. For this study, the ABL in the wind tunnel was interpreted as a geometrical scale of approximately 1:300.

The pressure transducer was used for pressure measurement. This device was conducted with plastic tube system to the investigated scale model. Transducer recorded the differential pressure between the reference point in free stream area and the point on the model. Then the pressure coefficient were defined as

$$c_{pe} = \frac{p}{1/2 \cdot \rho \cdot V^2} \tag{8}$$

where p is differencial pressure between local pressure on model and free stream static pressure in reference height [Pa], V is the free stream reference velocity on the reference height [m/s].

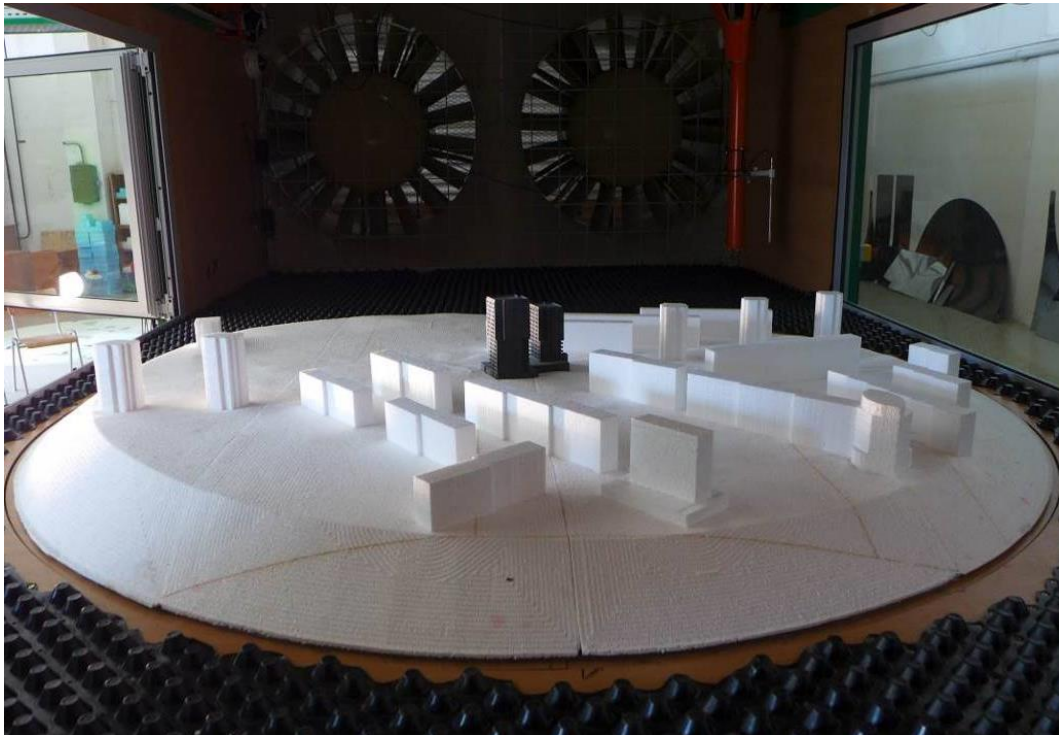Illustration of the arrangement of models and topography during measurement in wind tunnel is in Image 4.

Image 4 – Arrangement during tests in BLWT Bratislava

4   Conclusions

Numerical simulation shows us the overall view on the flow field around complex buildings because it was not possible to expect the flow pattern as for isolated simple building. Use of the calibrated and verified numerical model helps us for more accurate wind analysis. This approach is appropriate for localization of critical zone. But the quantification of loads and velocities is not very accurate. Values from simulations are slightly higher than from experiment. Therefore the simulation was used as base and preliminary study. For future works we will work to improve the simulation model for better catch with the wind tunnel experiment.

http://aum.svsfem.cz

References

ANSYS Inc., ANSYS Fluent Theory Guide, Release 18.1 (2017)

BLOCKEN B., CARMELIET J., 2004. A review of wind driven rain research in building science. *Journal of Wind Engineering and Industrial Aerodynamics*, vol. 92, pp. 1079 – 1130. ISSN 0167-6105.

BLOCKEN B., STATHOPOULOS T., CARMELIET J., 2007. CFD simulation of the atmospheric boundary layer–wall function problems. *Atmospheric Environment*, vol. 41(2), pp. 238-252. Elsevier (2007). ISSN 1352-2310.

FRANEK M., MACÁK M., KONEČNÁ L. 2016. Experimental and numerical evaluation of the external pressure coefficients on the elliptic cylinder. In Proceedings *of 24th SVSFEM ANSYS Users´Group Meeting and Conference 2016*, 1st – 3rd of June 2016, Dolní Morava, Czech Republic. pp. 53 – 62. ISBN 978-80-905525-3-1.

FRANKE J. et al., 2007. Best practice guideline for the CFD simulation of flows in the urban environment, COST Office Brussels (2007).

HUBOVÁ O. and LOBOTKA P., 2014: The multipurpose wind tunnel STU. *Civil and Environmental Engineering. Scientific- Technical Journal*. vol. 10th, Issue 1/2014, pp. 2 – 9, EV 3293/09. ISSN 1336-5835.

REICHRATH S., DAVIES T.W., 2002. Using CFD to model the internal climate of greenhouses: past, present and future. *Agronomie*, vol. 22, pp. 3 – 19. ISSN 0249-5627.

STATHOPOULOS T., 1997. Computational wind engineering: past achievements and future challenges. *Journal of Wind Engineering and Industrial Aerodynamics*, vol. 67 – 68, pp. 509 – 532. ISSN 0167-6105.

STN EN 1991-1-4, 2007. Eurocode 1: Actions on structures. Part 1-4: General actions. Wind actions (2017).

TOMINAGA Y. et al., 2008. AIJ guidelines for practical applications of CFD to pedestrian wind environment around buildings, *Journal of Wind Engineering and Industrial Aerodynamics* 2008. vol. 96, (10-11), pp1749-1761. ISSN 0167-6105.

Contact address:
Ing. Michal Franek, PhD.
Department of Building Construction, Slovak University of Technology in Bratislava, Faculty of Civil Engineering, Radlinského 11, 810 05 Bratislava
E - mail: michal.franek@stuba.sk

Ing. Marek Macák, PhD.
Department of Mathematics and Descriptive Geometry, Slovak University of Technology in Bratislava, Faculty of Civil Engineering, Radlinského 11, 810 05 Bratislava
E - mail: marek.macak@stuba.sk

doc. Ing. Oľga Hubová, PhD.
Department of Structural Mechanics, Slovak University of Technology in Bratislava, Faculty of Civil Engineering, Radlinského 11, 810 05 Bratislava
E - mail: olga.hubova@stuba.sk

http://aum.svsfem.cz

UTILIZATION OF OPTIMIZATION METHODS AND THEIR PRACTICAL APPLICATION IN HYDRAULICS

MATEJ PETROVIČ, MICHAL MASNÝ, JOZEF MIČIETA

Danfoss Power Solutions a.s., Považská Bystrica

Abstract: Various optimization methods and tools might significantly influence the product development in hydraulics and create the added value of the time spending on the optimization vs. the performance of the components. The article brings an overview of optimization methods which were applied on hydraulics components in real cases. The cases have been used for our product developments or component improvements. The optimizations in these cases affected the designs and functions of hydraulic components. Final designs have been physically tested and they are used in real applications.

Keywords: Optimization, Parametric, Non-parametric, Hydraulics

1   Introduction

THE AIM of the article is to describe the adoption of optimization methods in the designing, developing and improving hydraulic components. The optimization processes and best practices are included in the paper.

Optimization methods adoption and the components where they were applied to:

- topology optimization - plastic plug,

- parametric optimization - workpiece clamping,

- adjoint optimization - spool.

2   Topology optimization of the plastic plug

GENERALY SPOKEN, topology optimization (also known as a non-parametric optimization) changes a material layout in defined design space with respect to boundary conditions. The aim of the optimization is to maximize the efficiency of the system (WIKIPEDIA, 2019). The ANSYS software uses the SIMP (Solid Isotropic Material with Penalization method) gradient-based method (GUNWANT, 2012).

An exemplary topology optimization was applied on a plastic cover made from polyamide Durethan T40ZS - injection molded material with non-reinforced structure. The objective was to optimize the design regarding the strengths of the material. It was required to not increase tensile yield strength over 90 MPa and flexural ultimate strength over 130 MPa. The topology optimization played a key role to meet the requirements.
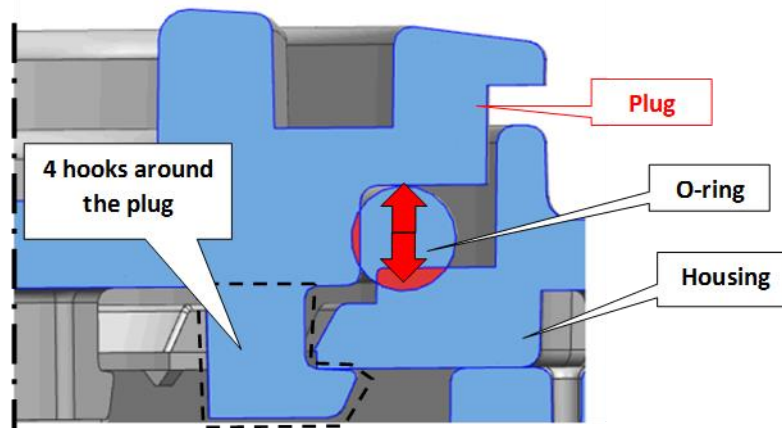
Image 2 – Geometry of plastic plug – cross-section view

The plug load is caused due to the press fit of the O-ring, deformed between the plug and the housing (Image 1). The maximum load is on the level of 210 N. The most loaded region of the plug is close to the interaction of the hooks with housing. They fix the plug in the housing.

One quarter-symmetric model including one complete hook was used for the FE-analysis. The initial plug was verified using the loading described above. The maximum principal stress is 137.33 MPa, which is 5.6 % over the flexural ultimate strength and 52.6 % over the tensile yield strength. The maximum principal stress was reduced to 100 MPa with geometry modifications (bigger radiuses, additional structures), which is still on non-acceptable level (it is over the tensile yield strength).
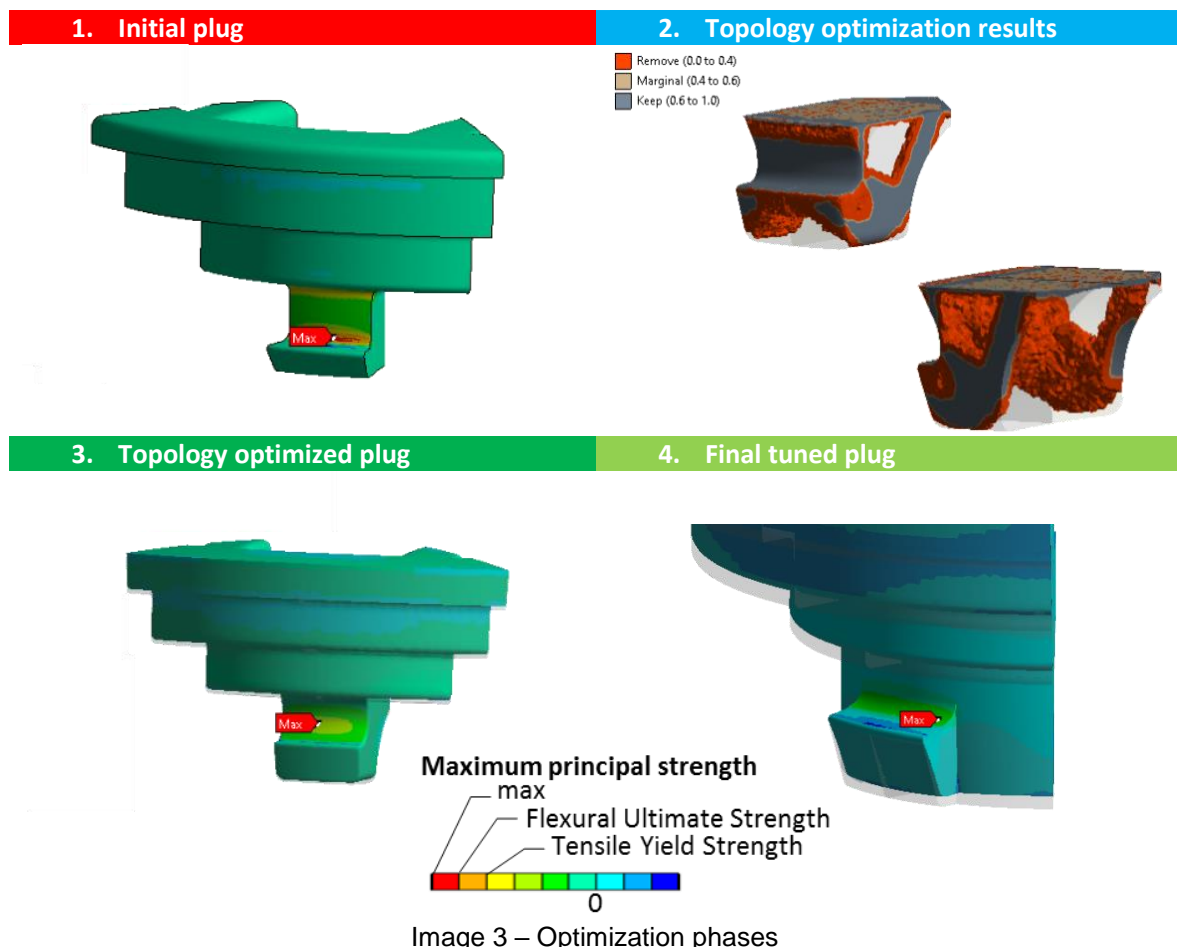

Image 3 – Optimization phases

The second step was to use the topology optimization. The area of the hook was modified – changed based on the topology sub-results within several phases to accept the space possibilities, results are summarized in the Image 2 and the Table 1. The next Topology optimized plug was designed with respect to the results. The maximum principal stress decreased to 89.45 MPa. The reduction of the maximum principal stress of the optimized plug was 35 % in comparison to the initial plug.

The outcome was presented to a team of design engineers, which made the next final design-tuned plug. This was the final design, because the stress level was reduced by additional 8.5 %. The maximum principal stress was 77.75 MPa and the plug is going to be tested. Prototypes from 3D printed material are currently verified and real parts are going to be available in a few months later.

Table 3   Maximum principal stress comparison, green: the darker the better; red: the lighter the better

Plug	Maximum principal stress (MPa)	Tensile yield strength (%)
Requirement - Target	90.00	100.0 %
Initial design	137.33	152.6 %
Topology optimized design	89.45	99.4 %
Final tuning	77.75	86.4 %

3 Parametric optimization of the workpiece clamping

A PARAMETRIC OPTIMIZATION at defined input variables finds extremes, minimum or maximum of output parameters according to respect any goal function. This type of optimization is usable if a simulation engineer knows all limitations of the structure. Every input is defined as a parameter with limits. The number of combinations of the input parameters (design points) defines the size of the optimization (JEKINS, 2014). Generally, a parametric optimization optimizes an investigated area (the most loaded area, spring shapes, etc.).

The aim of this particular case is to find the best position of the support pins for a clamping mechanism. This is another way how to utilize the parametric optimization tools. The support pins influence the precision of the machined housing after the machining process.

Input parameters for the optimization process are the positions of the support pins. The limits of each parameter were defined with a respect to the support pins of the workpiece. The deformations of the machined functional holes were considered as output parameters. The parametric optimization was done in the application ANSYS Design Xplorer. 240 design optimization loops were done to reach the optimal position of support pins.
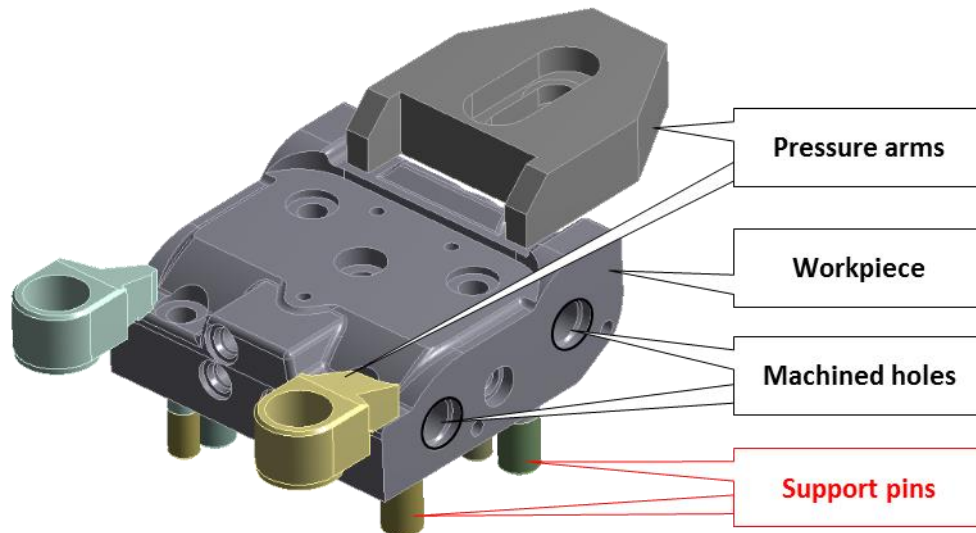
Image 4 – Clamping mechanism of workpiece

The outcomes of the parametric optimization were discussed with the production team and the new configuration of the support pins is going to be tested. Calculated radial deformations of the holes improved in the range of 7 – 31 %. The optimization shown nonuniform loading of the support pins in the initial setup. Two-times higher loading comes from preload bolt forces on the side with the two pressure arms (see Image 3), which can generate unstable clamping. Two support pins near the side with two bolts (left side) were overloaded in the original configuration. This effect has been eliminated in the new configuration of the support pins (see Table 2).

Table 4 Radial deformation improvement, the darker green is the better it is

Radial deformation (μm)		Original configuration	Optimized configuration	Difference to the Original
Hole 1	Maximum	3.67	2.53	-31 %
	Minimum	-6.67	-4.96	-26 %
Hole 2	Maximum	12.25	11.45	-7 %
	Minimum	-20.50	-16.65	-19 %

4   Adjoint optimization of the spool

ADJOINT OPTIMIZATION is a type of non-parametric optimization. Adjoint Solver and Morpher are special tools of Fluent which can extend the scope of standard flow analyses. Adjoint Solver provides sensitivity data in respect to desired objective (pressure drop, flow force etc.) The sensitivity data are used by Morpher for modification of the geometry (LI, 2011).

Objective of this example was to eliminate the pressure drop over the spool. The spool is as a barrier for oil flow and a key for the valve function as well. Each modification which decreases the pressure drop results in increasing the valve efficiency.

At first, the geometry of the valve cavities was modified for calculation in the ANSYS Fluent software. For this type of FEA simulations, the model was prepared only for one position of the spool. This position is probably the most frequent work stroke of the spool for the selected dimensions at defined mass flow rate.

In the next step the first model for the calculation of the current geometry was set up. The optimization process is described in the Image 4. All calculations were

solved with a steady – state turbulent flow model for the same position of the compensator spool in the cavity of the spool valve. Defined boundary conditions were the velocity at the inlet and the pressure at the outlet. The inlet velocity was calculated for the maximal value of the flow rate of 220 l/min and with the outlet pressure equals zero in all calculations. The adjoint solver offers many types of observables of interest such as force, moment of force, swirl … (EIGGENSPIELER, 2011).
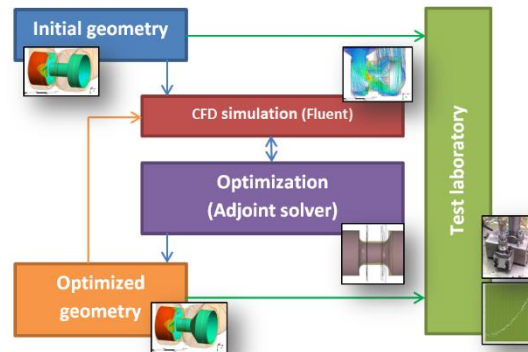

Image 5 – Process of the optimization

Adjoint solver modifies the surfaces within the requirements and keeps a respect for minimization of the pressure drop between the inlet and outlet (ANSYS, 2013). Here is possible to check current value during the setting of studied parameter. In Adjoint solution control, the stabilized scheme of the advancement controls was checked. The convergence criteria were set up in the next step. If all necessary options are set, the solution of the optimization calculation starts. After the calculation many sensitivity parameters of the geometry could be compared. Design modifications were evaluated in this case. The morphing control was used for the geometry editing. The modified geometry was exported for the next analysis. Image 5 shows the modified design versus the initial one. The diameter of the spool neck was changed and the opposite wall to the flow angle direction is under 53°. This value resulted from the geometry configuration and the boundary conditions. The velocity streamlines show how the spool shape impacts to the oil flow through the valve. This influence is evaluated with the radial forces.
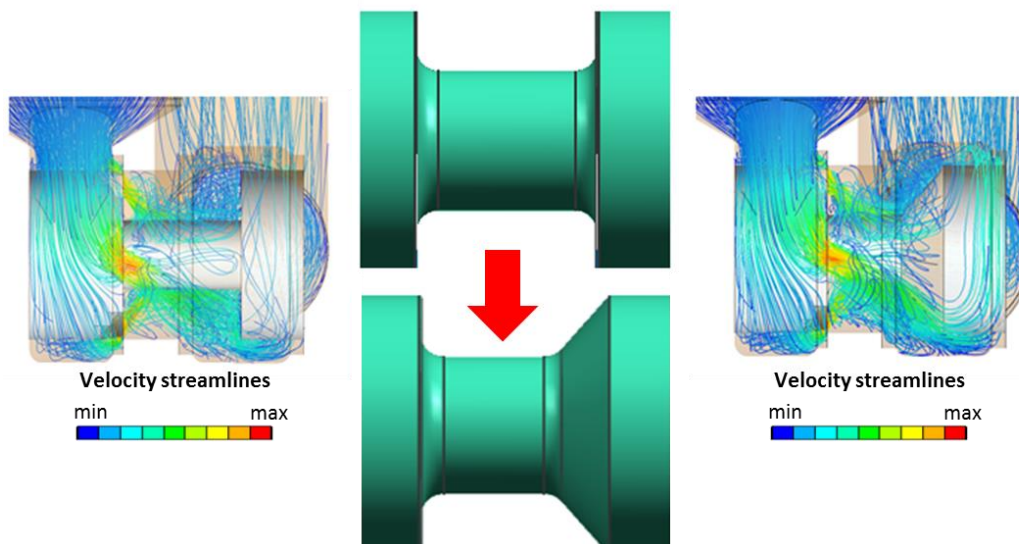

Image 6 – Velocity streamlines of the initial design (left), the initial versus the recommended optimized design (middle), velocity streamlines of the optimized design (right)

The spool was validated in the test lab in an open hydraulic circuit shown in Image 6. In this simple hydraulic scheme, no measuring accessories are shown. The spool (2) was tested in the two modifications – initial and optimized design.

Both variants were tested with a pressure ramp from 0 to 300 bar with the flow rate of 220 l/min by the orifice (3).
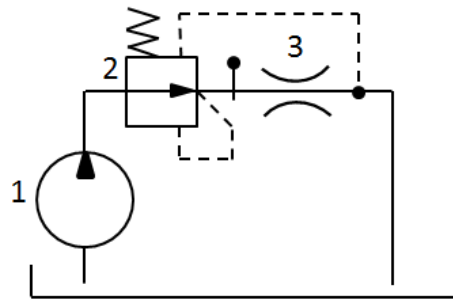

Image 7 – Hydraulic scheme of the tested valve without the measuring accessories:
1 - Pump, 2 - Tested spool and 3 - Orifice

The outcome (see Table 3) is a 7 % smaller pressure drop and it was achieved for oil flow through the valve. The spool modification has a significant influence on radial forces, it means 50 % increase. This impact can be reduced by the next cavity modification. Moreover, this modification came up to another 2 % improvement of the pressure drop.

Table 5   Adjoint optimization results comparison, green: the darker the better; red: the lighter the better

Geometry	Delta pressure reduction [%]	Delta Radial force to the reference [%]
Initial spool	reference	reference
Optimized spool	-7 %	+50 %
Optimized cavities	-9 %	+9 %

5 Conclusion

THE PAPER presents three types of optimizations: parametric optimization and two non-parametric optimizations – topology (structures) and adjoint (fluid domains). They have been applied in exemplary hydrostatic components. In general, optimizations have a strong valuable impact on product/component design development or its improvement. Deployment of optimization methods into the simulation-based design with systematic optimization tools, no trial and error method - based on "by experience", speed up the development within 20-30 %.

As nothing comes for free, one key prerequisite is knowing the toolset and its capabilities, otherwise this might need a lot of time and decrease the value of the outcome.

References

WIKIPEDIA THE FREE ENCYCLOPEDIA, 2019. *Topology optimization*. Wikipedia Foundation, Inc., 1 page, Available At: https://en.wikipedia.org/wiki/Topology_optimization

DHEERAJ GUNWANT, 2012. *Topology optimization of continuum structures using optimality criterion approach in ANSYS*. International Journal of Advances in Engineering & Technology. ISSN: 2231-1963, 16 pages, Available at: http://www.e-ijaet.org/media/47I11-IJAET1111180-Topology-Optimization.pdf

BRUCE JENKINS, 2014. *Parametric vs. non-parametric optimization*. Ora Research LLC, 1 page, Available At: http://oraresearch.com/2014/12/parametric-vs-non-parametric-optimization/

GENONG LI, CHI-YANG CHENG, 2011. Mesh Morphing and the Adjoint Solver in ANSYS R14.0. ANSYS, Inc., 55 pages, Available At:
https://support.ansys.com/staticassets/ANSYS/Conference/Boston/downloads/Mesh%20Morphing%20and%20Adjoint%20Solver%20-%20Li%20-%20Cheng.pdf

EGGENSPIELER GILLES, 2011. Ansys Fluent Adjoint Solver. Ansys, Inc., 38 pages, Available At:
https://support.ansys.com/staticassets/ANSYS/Conference/Confidence/San%20Jose/Downloads/optimization-adjoint-solver-9.pdf

ANSYS, INC. SOUTHPOINTE, 2013. ANSYS Fluent Adjoint Solver (Adjoint Solver Module Manual), ANSYS, Inc. Southpointe, 74 pages, Available At:
http://148.204.81.206/Ansys/150/ANSYS%20Fluent%20Adjoint%20Solver%20Manual.Pdf

NUMERICAL INVESTIGATION OF A MULTISTAGE CENTRIFUGAL RADIAL PUMP

PROKOP MORAVEC[1], LUKÁŠ ZAVADIL[1], JAKUB STAREČEK[1], TOMÁŠ KRÁTKÝ[1]
[1] Centre of Hydraulic Research

Abstract: The paper is focusing on numerical simulations of both, CFD and structural analysis of the multistage centrifugal radial pump CNE 2.2/5. Three types of a balance piston are investigated to uncover their possible advantages or disadvantages for a pump operation.

Keywords: Multistage centrifugal radial pump, balance piston, CFD, FSI, ANSYS CFX.

1   Multistage pumps

In general, the main attributes of a single stage centrifugal radial pump are characterized by a type (shape/dimensions) of the impeller, operating conditions, and its RPM. If a performance exceeding single limitation (RPM, size, etc.), exploitation of the several impellers arranged in series is a fitting solution, where each stage contributes with the same volumetric flow rate, but the heads add up to the total pump head (GÜLICH, 2014) – see Image 1.
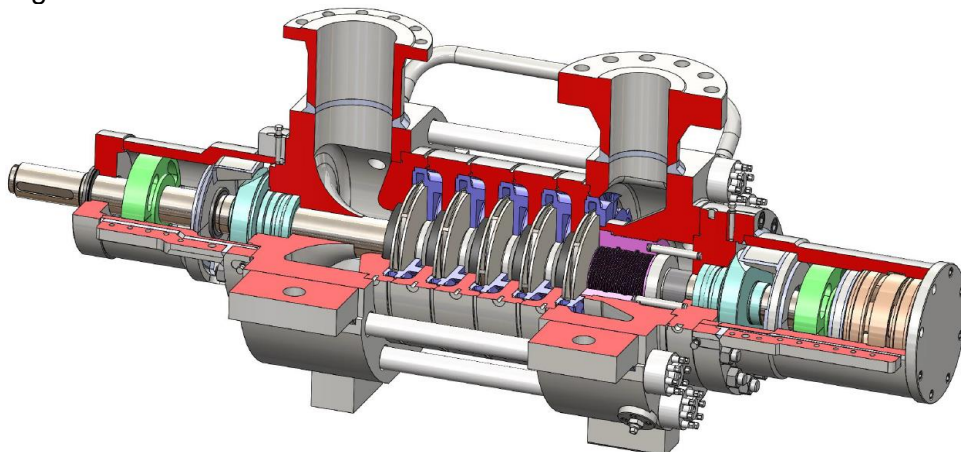

Image 1 – Multistage pump with the balance piston CNE 2.2/5

1.1   Balance pistons

Pressures created by the centrifugal radial pump cause axial forces on rotary and stationary parts (Image 2). Proper design of these parts can help, but the remaining forces need to be counterbalanced additionally (KARASSIK, 2008).
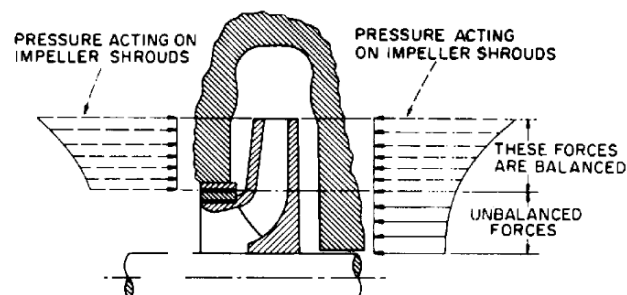

Image 2 – Pressure distribution and axial forces on the impeller (KARASSIK, 2008)

For the single-suction impellers of the multistage pump, where all are oriented in the same direction (Image 1), the total theoretical hydraulic axial thrust is computed as

a sum of the individual impeller thrusts. A direction of such total theoretical axial thrust is towards the suction part of the multistage pump. A part of this force must be balanced by some form of hydraulic balancing device, such as a balancing disk or the balance piston, to achieve the proper stability of the rotating parts of the pump (GÜLICH, 2014), (KARASSIK, 2008).

Balance piston induces a force, which acts in the opposite way than the axial thrust and has several advantages/disadvantages (GÜLICH, 2014):

- Robust design

- High reliability in operation

- Higher leakage

1.1.1. Physical phenomena affecting the piston

The force, which acts in the radial direction, is in the annular seal established by the direct stiffness. A significant pressure difference is created between the wide and narrow gap, due to the higher magnitude of the inlet loss on the side with the narrow gap. Such pressure difference causes a creation of a force, which centers the rotor (acts in the opposite way, then the rotor radial displacement). This phenomenon is called the **Lomakin effect** (GÜLICH, 2014) – see Image 3 **a**.

In the other way goes the **Bernoulli effect** with a de-centering impact (Image 3 **b**). A circumferential velocity c_u is in the annular seal maximal on the side of the narrow gap. With the maximal magnitude of the velocity goes hand in hand the minimal value of the pressure (Bernoulli equation). As a result, a force component $F_{r,B}$ acts from the wide to the narrow gap, such fact is captured in Image 3 **b** (GÜLICH, 2014).
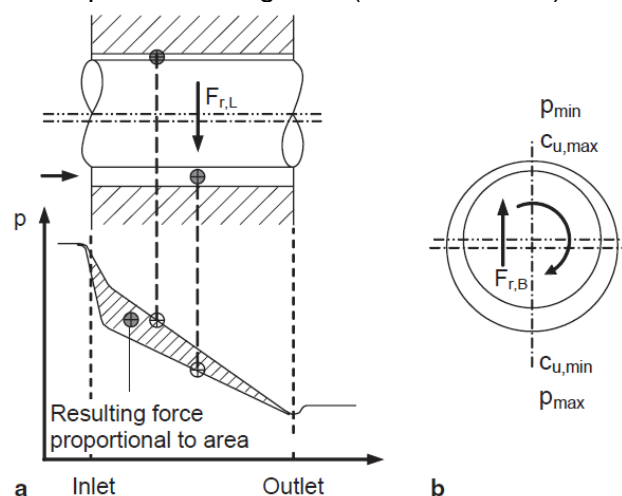

Image 3 – Radial forces in annular seal: **a** Lomakin effect; **b** Bernoulli effect (GÜLICH, 2014)

It must be noted that a proper design of the balance piston should equalize both, the Lomakin and the Bernoulli effect, to achieve the proper stability of the rotating parts of the pump.

1.2 Piston modifications

Three modifications of the balance piston were created and afterwards examined with CFD simulations, namely: the balance piston with flow channels in the rotor (Grooved rotor, Image 4 **a**), the balance piston with flow channels in stator (Grooved stator, Image 4 **b**) and the balance piston with flow channels in stator together with a swirl brake (Grooved stator + SB, Image 4 **c**).
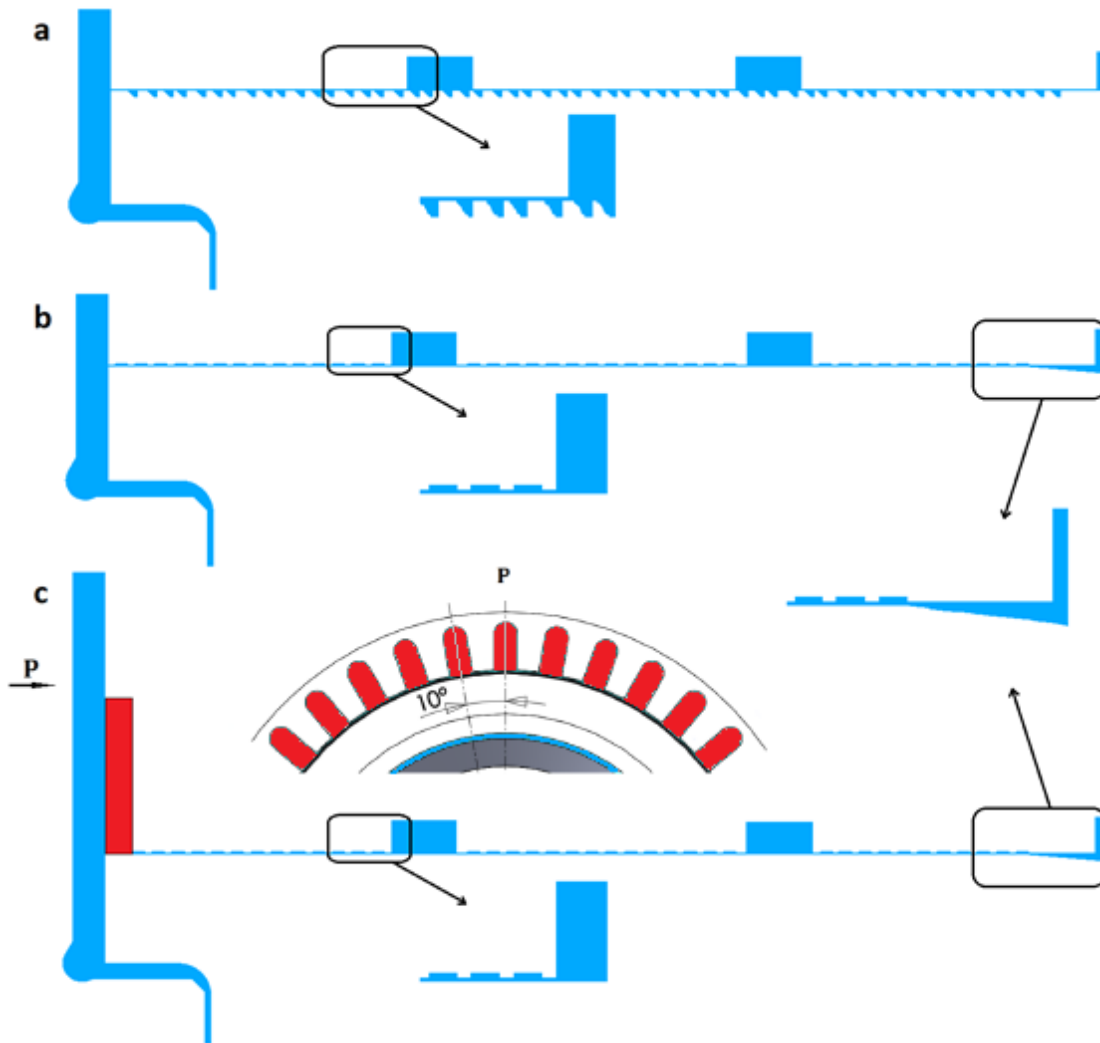
Image 4 – Types of the balance piston

The swirl brake (Image 4 **c**) is portrayed in the third modification by the red color and in the fluid model is characterized by **36 rectangular chambers** equally distributed at the beginning of the balance piston.

When creating the presented modification, several key attributes of the balance piston were pursued:

- Change of the pressure field
- Change of the velocity profile
- Circumferential velocity decrease
- Retaining volume losses
- Inlet fluid pre-rotation suppression
- Change of the resultant radial force acting on the piston

2 CFD simulation

Transient numerical simulations with **ANSYS CFX** were extensively utilized in a process of capturing flow inside the multistage centrifugal pump and afterwards for pressure distributions on the rotational and stationary walls, which were exploited in the fluid-structure interaction analysis. The fluid model was created according to a CAD model, in which all requested pump domains were present (Image 5). As a proper initialization for

the mentioned transient calculations served stationary simulations, which estimated the velocity and pressure fields in all flow domains.
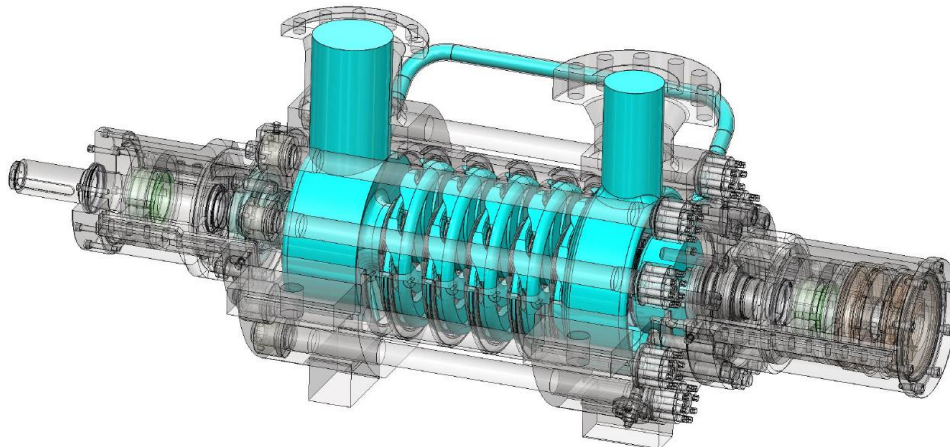

Image 5 – Fluid domain

The SST k-ω model of turbulence was chosen in all created CFD pump cases with a timestep value that represented 2 degrees of the rotor revolution. Each transient pump case included **117 expressions** for capturing hydraulic attributes of the CNE 2.2/5.

2.1　Computational domains

The complete CFD fluid model had **37 partial domains** separated from each other with either, GGI (green), or transient rotor-stator (red) types of interfaces (Image 6). The transient rotor-stator interfaces were employed between rotating and stationary domains to ensure correct flow patterns inside the pump.
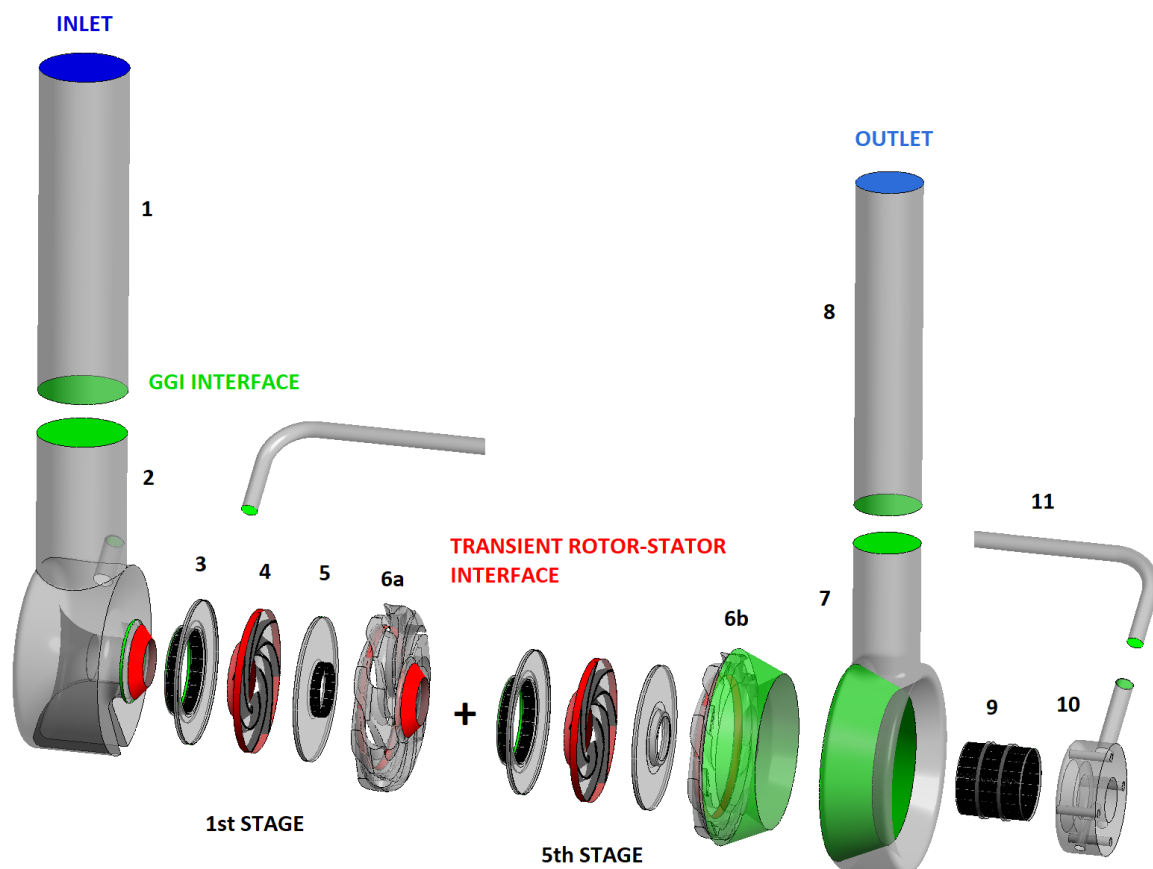

Image 6 – Computational domains for CFD

http://aum.svsfem.cz

Pressure from an auxiliary pump served as an inlet boundary condition – in Image 6 is this fact characterized by a dark blue color in domain 1. On the other hand, the outlet boundary condition was located in domain 8 and was portrayed by a mass flow rate, which corresponded to the chosen volumetric flow rates characteristic for the multistage pump CNE 2.2/5.

2.2   Computational mesh

The computational mesh of the multistage pump CNE 2.2/5 utilized hexahedral elements (for impellers, side-walls, balance piston) and tetrahedral types of elements (for inflow domain, outflow domain, diffusers, transfer tube, space behind piston) with high resolution near the walls (Image 7). The hexahedral mesh was created primarily in **ICEM CFD**, on the other hand, the tetrahedral computational grids were prepared in **ANSYS Meshing**.
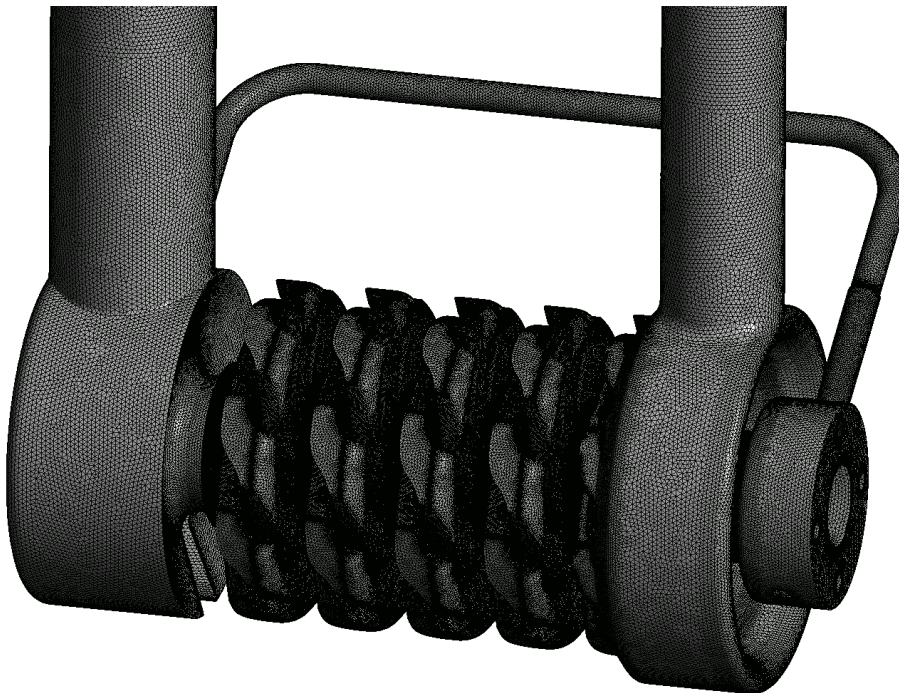
Image 7 – Computational mesh

With approximately 38 million nodes (58 million elements), the CFD simulations of the CNE 2.2/5 pump were the largest project ever made in the Centre of the Hydraulic Research..

2.3   CFD results

All performance characteristics of the pump were evaluated. However, the CFD analysis was primarily focused on the flow inside the three modified types of the balance piston (Image 6; domain 9), at first mostly on the absolute static pressure (Image 9) together with the axial (Image 10) and the circumferential velocity (Image 11), which were examined on a line located in the middle of the piston radial height (Image 8).

Image 8 – Position of the evaluation line (detail)

http://aum.svsfem.cz

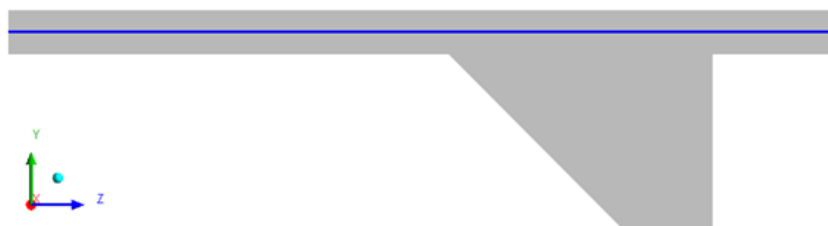Image 9 illustratavely shows gradual progress (decrease) of the absolute static pressure at the optimal flow rate of the pump from the highest to the lowest magnitude across the length of the balance piston. The length of the balancing device is expressed by an axial position *z (mm)*, where the beginning of each piston lies is in the axial position *z = 613 mm* and the end in *763 mm*.
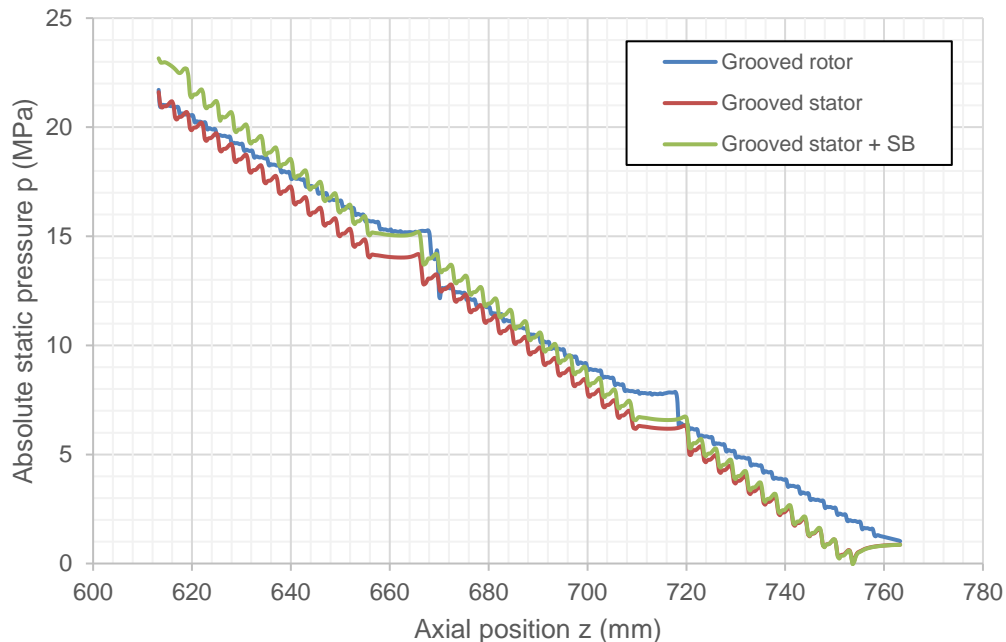
Image 9 – Absolute static pressure (optimal Q)

The balance piston with the grooved stator together with the swirl brake (green color, Image 9) is distinguished by higher magnitudes of the absolute static pressure at the beginning of its length. On the other hand, the absolute static pressure located at the end of both modification with the grooved stator is significantly lower than in the modification with the grooved rotor and even drops down to values close to the water vapour pressure. It means that cavitation could possibly develop in these areas.
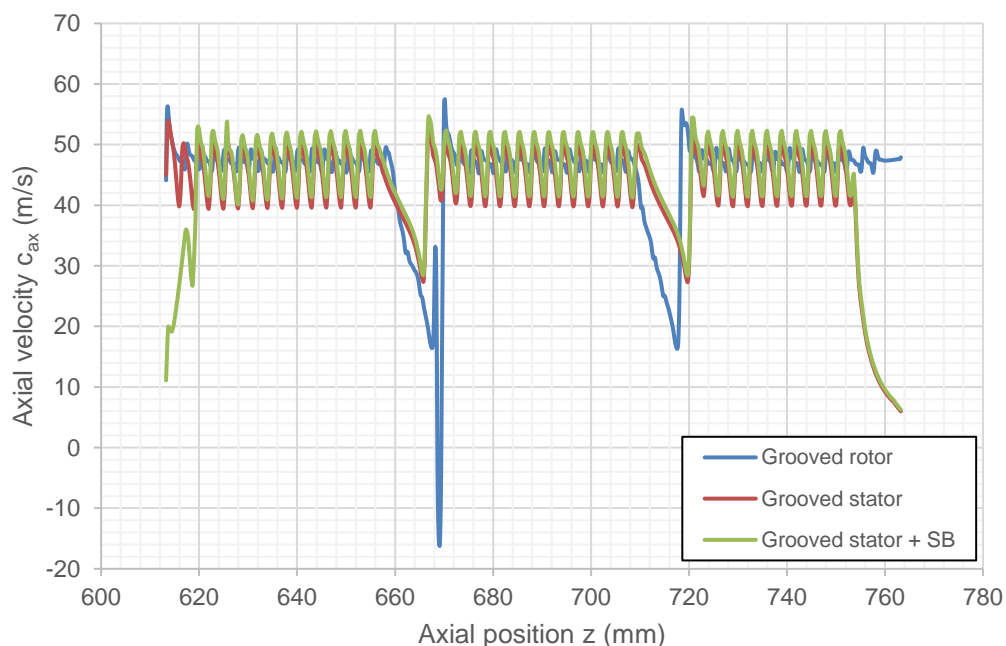
Image 10 – Axial velocity (optimal Q)

Images 10 and 11 capture specific (selected) velocities across the length of the balance pistons. First (Image 10), the circumferential velocity in the optimal flow rate of the multistage centrifugal radial pump is depicted on the line, which is positioned in the 50% of the piston clearance.
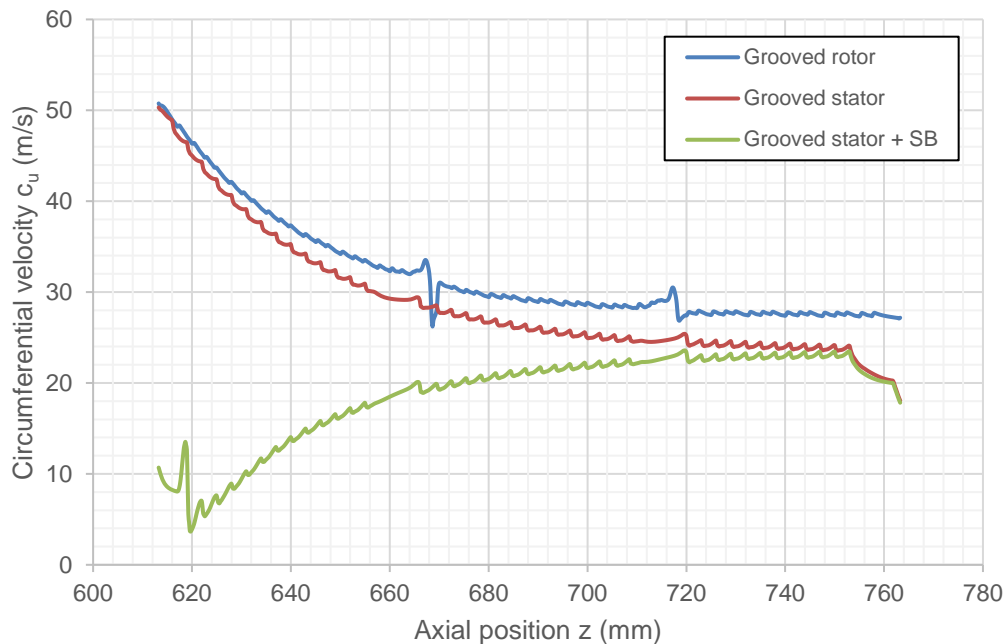
Image 11 – Circumferential velocity (optimal Q)

The axial and circumferential velocity decrease is obvious from Images 10-11 in the balance piston case with the grooved stator together with the swirl brake (portrayed by the green color). Such significant velocity change is caused by the rectangular chambers of the swirl brake located in the front part of the device, where the current fluid flow is substantially decelerated.

Images 10 and 11 also clearly reveal, how a change (enlargement) of the outlet area of the balance piston, which is captured in detail in Image **b**, **c**, affected the examined axial and circumferential velocities – the magnitude reduction of those mentioned velocities is perceptible.

Image 12 – Mass flow rate in the balance piston (optimal Q)
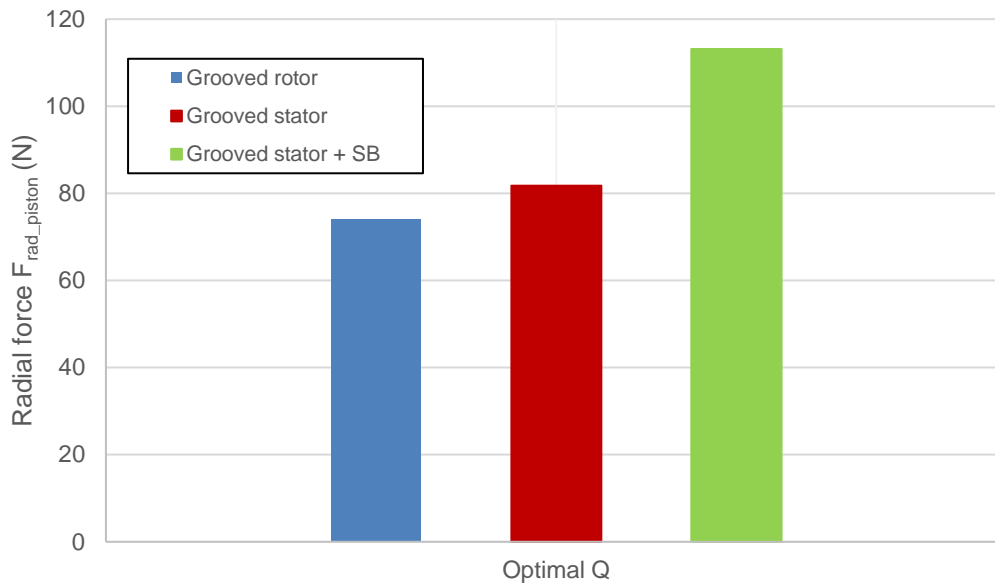
Image 13 – Radial force acting on the balance piston (optimal Q)

The last two images in this section (Image 12, 13) compare the mass flow rates through the modifications of the balancing devices and afterward the radial forces acting on the walls of the balance pistons. The highest mass flow rate has the modification with the grooved stator together with swirl brake, on the other hand, the modification with grooved rotor possesses the lowest mass flow rate through the piston (the difference is approximately 0.2 kg/s). The 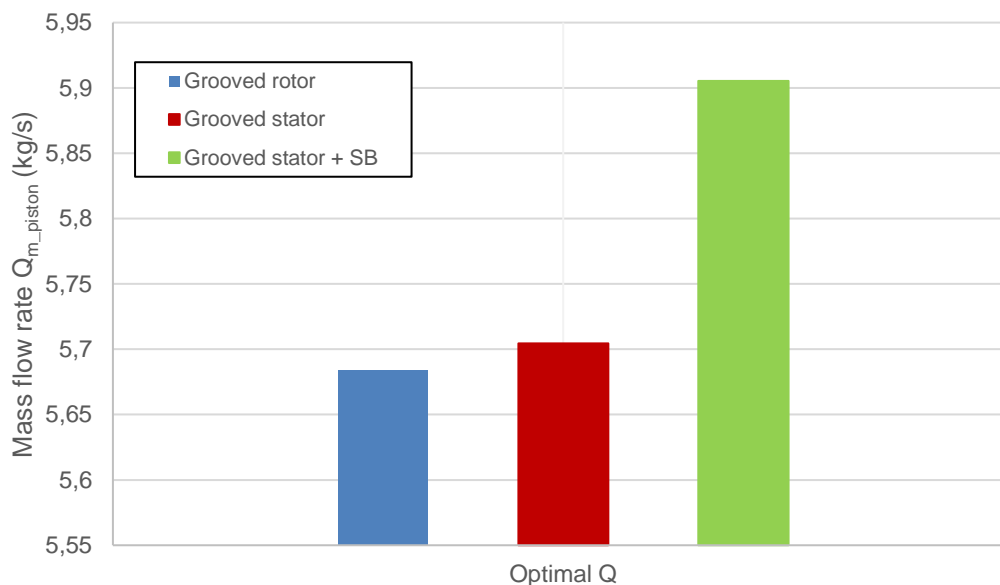walls of the piston modification with the grooved stator together with the swirl brake exert the higher radial force (Image 13) than the other investigated types of the balance piston, but the difference between the results is not significant.

3   FSI analysis (Static structural analysis)

Another crucial outcome from the transient CFD simulations was pressure distribution, which acted on solid walls during the fluid flow across the pump domains. Such pressure was imported on a solid model of the investigated multistage pump and afterwards utilized in the static structural analysis – Image 14 illustratively shows pressure import on the rotor of the pump.

Image 14 – Pressure import - rotor (structural analysis, Optimal Q, Grooved stator)

The static structural analysis employed a coarse mesh (Image 15) formed in **ANSYS Meshing** (approximately 1.6 million nodes / 9 million elements), the pressure from one timestep of the transient CFD simulation was used for both the static and rotating parts of

the pump and a half of a clutch (yellow body – left side; Image 15), which simulated a proper mounting of the multistage pump in a test circuit.
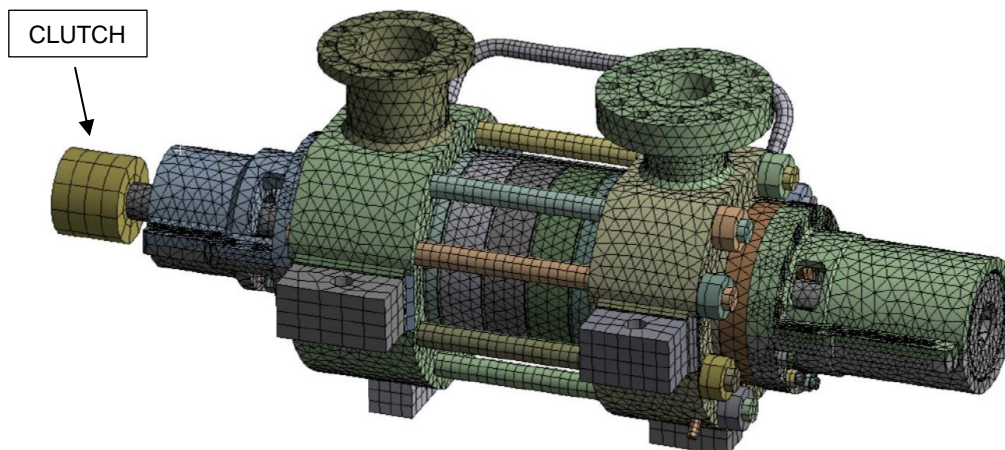
Image 15 – Structural mesh

Image 16 compares a total deformation of a pump shaft for all investigated modifications of the balance piston. Black lines in Image 16 show the position of the balancing device.
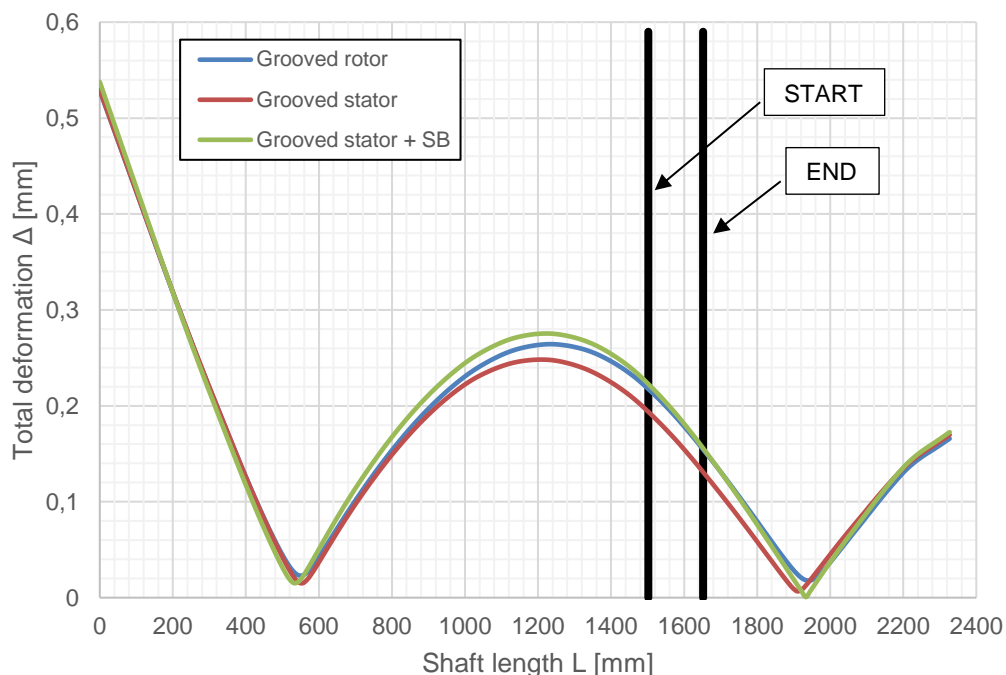
Image 16 – Shaft deformation

All the examined modifications display similar shaft total deformation at the axial location of the balance piston (in a range approximately between *0.1 – 0.2 mm*). Such deformations did not exceed a total gap between the stationary and rotating part of the balance piston. It must be noted that the total deformations were evaluated from one timestep of the transient CFD simulation and on the centered rotor, which was rotated to a specific position to properly fit and subsequently utilized the pressure fields on solid bodies. This computational approach overestimated the total deformations and should be substituted by the two-way FSI analysis, where the flow in the deformed piston is taken into account.

4　Conclusion and future outlook

The transient CFD simulations of the multistage centrifugal radial pump CNE 2.2/5 were performed for several RPM values and flow rates using turbomachinery-focused ANSYS CFX. With almost 38 million nodes, this project was the largest numerical simulation ever performed/executed by the Centre of the Hydraulic Research. Presented numerical simulations were focused on the flow investigation in the area of the balance piston. The balance piston is the device, mainly used in the centrifugal pump machinery to counterbalance some of the axial force acting on the pump rotor. Proper dimensions and overall shape of the piston play a crucial role in the correct behavior of this balancing device, where two effects (Lomakin and Bernoulli) strongly influence the rotor stability. Three modifications of the balance piston (with the grooved rotor, grooved stator and grooved stator together with the swirl brake) were created, simulated and subsequently compared on the flow and static structural basis. The flow analysis examined the static pressure, the axial and circumferential velocities along the length of the piston in the 50% of its height (see Image 8). From the CFD results is noticeable that the rectangular chambers of the swirl brake strongly decelerated the fluid flow, which is projected in the axial/circumferential velocity decrease and the static pressure increase at the front part of the piston. It must be noted that the modifications with the grooved stator show lower overall values of the static pressure in the rear section of the balance piston. This fact could be potentially problematic due to the possible cavitation development. The static structural analysis was also performed on all examined modifications of the balance piston. The total gap between the stationary and rotary parts of the piston was not surpassed, but the results of this analysis showed to be insufficient and the two-way FSI analysis will take place in the future work. In short, the future outlook includes:

- Two-way FSI analysis
- Physical measurement
- Comparison between the measurement and the two-way FSI analysis

References

GÜLICH, J. F. Centrifugal pumps. 3rd edition. Heidelberg: Springer, 2014, xli, 1116 p. ISBN 978-3-642-40113-8

KARASSIK, I. J. Pump handbook. 4th edition. New York: McGraw-Hill, 2008, 1102 p. ISBN 978-0-07-146044-6.

Acknowledgement

Contact address:
Ing. Prokop Moravec (p.moravec@sigma.cz), Ing. Lukáš Zavadil, Ph.D., Ing. Jakub Stareček, Mgr. Tomáš Krátký
Centre of Hydraulic Research, Jana Sigmunda 313, 783 49 Lutín

ON OWN CONSTITUTIVE MODELS IMPLEMENTATION INTO ANSYS

RADIM HALAMA

Department of Applied Mechanics, Faculty of Mechanical Engineering, VSB-TU Ostrava, 17.listopadu 2172/15, Ostrava 70800, Czech Republic

Abstract: The main aim of this contribution is to help other researchers to implement advanced constitutive equations into the FE program ANSYS. The basic procedure for user programmable features is described. Then, the improvement of distributed UPF subroutine is shown in 1D for the kinematic hardening rules of Prager and Chaboche. An implicit numerical stress integration algorithm is used for the implementation task. Finally, some interesting results of strain accumulation prediction based on own constitutive equations are presented.

Keywords: FEM, plasticity, small strain analysis, material model implementation

1 Introduction

The phenomenological approach in constitutive modeling has been extensively developed in last two decades. However, the material models available in commercial FE codes are not up to date, because there are too many applications and it is difficult to find out material models, which can help engineers with constitutive modeling. Too many parameters and too difficult calibration procedure are two main reasons of the current situation. There is no "universal" plasticity model even for materials with the same microstructure, i.e. metals, elastomers, concrete etc. Each phenomenological model is suitable for certain small group of materials, for instance austenitic stainless steels or aluminum alloys. That is why the possibility of own constitutive material model implementation is an important feature of FE codes. The main aim of this work is to describe the way of own constitutive model implementation and application in ANSYS. Some interesting results for MAKOC model with memory described in (HALAMA R., FUSEK M., ŠOFER M., PORUBA Z., MATUŠEK P., FAJKOŠ R., 2015) are presented for asymmetric multiaxial loading with emphasize on ratcheting description. The implementation for Prager bilinear kinematic hardening rule, Chaboche nonlinear kinematic hardening rule and own robust material model with a memory surface will be described briefly during the presentation of contribution on the conference.

2 General information about user subroutines in ANSYS

2.1 User subroutines

ANSYS supports implementation of own constitutive equations via subroutines written in FORTRAN or C++ (ANSYS, 2019). ANSYS distribution already provides templates of user subroutines. In the case of plasticity or viscoplasticity, USERMAT.F and USERPL.F can be modified according to the hardening model considered. Each subroutine works with particular types of finite elements. Several elements linked to USERPL.F are not available from GUI anymore (ANSYS, 2019). On the other hand, major part of them can be activated using the ANSYS script language APDL (ANSYS Parametric Design Language), thus the possibility of its usage is still available. New types of elements supports the subroutine named USERMAT.F. Uniaxial version of constitutive models can be implemented for 1D element LINK180 via subroutine USERMAT1D.F. The 3-dimensional case corresponds to the subroutine USERMAT3D.F.

2.2   Basic steps

By linking in own FORTRAN/C++ routine, a custom site-specific version of the ANSYS program is created and can be subsequently used in a FE analysis. Depending on the operating system a correct version of the Fortran and C ++ compilers must be installed on the computer. In the case of ANSYS 2019 R1, Microsoft Visual Studio Professional 2015 update 3 (including the MS C++ compiler), Intel C++ 17.0.4 compiler and Intel Visual FORTRAN 17.0.4 compilers are required. Before compiling, Customization Tools must be installed from the ANSYS installation menu. The code can be compiled in following steps:

- First, it is recommended to correctly set the system variables in the operating system

- Creating a USERMAT.F file and copying it to the folder:

    DISC:\Program Files\ANSYS Inc\vXXX\ansys\custom\user\platform

- Run the ANSCUST.bat batch file, which will compile all * .F and * .C files in the folder defined in the previous step. A new ANSYS.exe executable is created in the same directory.

In the case of 64bit Windows operation system, the platform is winx64. The new version of ANSYS.exe can be used by setting the path to the custom executable file in the ANSYS APDL Product Luncher.

3   Small strain plasticity implementation

In this chapter, small strain case is considered for the general form of kinematic hardening rule according to (KOBAYASHI M., OHNO N., 2002). During implementation, all equations could be rewritten to the matrix form as eplained in the conference paper (HALAMA R., FUSEK M., 2005). The MAKOC model with memory implementation is described in more details in the paper (HALAMA R., MARKOPOULOS A., JANČO R., BARTECKÝ M., 2017).

3.1   Incremental theory of plasticity

The rate-independent material's behavior model includes the additive rule for the total strain tensor

$$\epsilon = \epsilon^e + \epsilon^p, \tag{4}$$

with Hook's law assumption for elastic strain

$$\boldsymbol{\sigma} = \mathbf{D}^e{:}\epsilon^e = \mathbf{D}^e{:}(\epsilon - \epsilon^p), \tag{5}$$

where ϵ^p is the plastic strain tensor and $\mathbf{D}^e$ is the elastic stiffness matrix. The symbol $:$ denotes contraction, ie. using Einstain's summing rule $\boldsymbol{d} = \boldsymbol{b}{:}\boldsymbol{c} = b_{ij}c_{ij}$. According to yield surface concept, von Mises yield function is considered

$$f = \frac{3}{2}(\boldsymbol{s} - \boldsymbol{a}){:}(\boldsymbol{s} - \boldsymbol{a}) - Y^2, Y = \sigma_Y + R, \tag{6}$$

where $\boldsymbol{s}$ is the deviatoric part of stress tensor $\boldsymbol{\sigma}$, $\boldsymbol{a}$ is the deviatoric part of back-stress $\boldsymbol{\alpha}$, which states the centre position for the yield surface, Y corresponds to the radius of the yield surface with the initial size σ_Y and R is the isotropic variable. When a point characterising the current stress state lays on the yield surface, it is supposed, that it does not leave the yield surface. Therefore, so called consistency condition must be satisfied $\dot{f} = 0$. In the case of active loading (f=0 and $\dot{f} = 0$), the associated plastic flow rule is often used

$$d\boldsymbol{\epsilon_p} = \sqrt{\frac{3}{2}}d\lambda\frac{\partial f}{\partial \boldsymbol{\sigma}}, \tag{7}$$

whereas from the equation (3) goes

$$\frac{\partial f}{\partial \boldsymbol{\sigma}} = \sqrt{\frac{3}{2}}\frac{\boldsymbol{s}-\boldsymbol{a}}{Y} = \boldsymbol{n}. \tag{8}$$

The plastic multiplier $d\lambda$ in eq. (4) corresponds to the equivalent plastic strain increment. Generally, combined hardening model can be assumed, so the model consists of a kinematic hardening rule

$$d\boldsymbol{a} = g\big(\boldsymbol{a}, \boldsymbol{\epsilon_p}, d\boldsymbol{\epsilon_p}, dp, \boldsymbol{n}, etc.\big) \tag{9}$$

and an isotropic hardening rule

$$dY = h\big(R, dp, \boldsymbol{\sigma}, \boldsymbol{a}, \boldsymbol{\epsilon_p}, etc.\big). \tag{10}$$

3.2   Radial return alorithm application

The group of cyclic plasticity models of Chaboche type is considered in this work. Therefore, the backstress is decomposed to M parts

$$\boldsymbol{a} = \sum_{i=1}^{M}\boldsymbol{a}^{(i)}, \tag{11}$$

where each part is defined by its own evolution equation, mostly of Armstrong-Frederick type

$$d\boldsymbol{a}^{(i)} = \frac{2}{3}C_i d\boldsymbol{\epsilon_p} - \gamma_i\boldsymbol{a}^{(i)}dp^{(i)}, \tag{12}$$

where except material parameters C_i, γ_i and plastic strain increment $d\boldsymbol{\epsilon_p}$ the plastic strain increment $dp^{(i)}$ appears, which caused dynamic recovery of $\boldsymbol{\alpha}^{(i)}$. The quantity $dp^{(i)}$ may acquire a maximum value of the accumulated equivalent plastic strain, ie. $dp^{(i)} = dp = \sqrt{\frac{2}{3}d\boldsymbol{\epsilon_p}:d\boldsymbol{\epsilon_p}}$.

After Euler backward discretization it is possible to rewrite kinematic hardening rule

$$\boldsymbol{a}_{n+1}^{(i)} = \boldsymbol{a}_n^{(i)} + \frac{2}{3}C_i\Delta\boldsymbol{\epsilon}_{n+1}^p - \gamma_i\boldsymbol{a}_{n+1}^{(i)}\Delta p_{n+1}^{(i)} \tag{13}$$

to this form

$$\boldsymbol{a}_{n+1}^{(i)} = \theta_{n+1}^{(i)}\left(\boldsymbol{a}_n^{(i)} + \frac{2}{3}C_i\Delta\boldsymbol{\epsilon}_{n+1}^p\right), \tag{14}$$

where

$$\theta_{n+1}^{(i)} = \frac{1}{1+\gamma_i\Delta p_{n+1}^{(i)}} \tag{15}$$

fulfills the condition $0 < \theta_{n+1}^{(i)} \leq 1$. Now, it is important to ensure the yield condition

$$f_{n+1} = \frac{3}{2}(\boldsymbol{s}_{n+1} - \boldsymbol{a}_{n+1}):(\boldsymbol{s}_{n+1} - \boldsymbol{a}_{n+1}) - Y_{n+1}^2 = 0, Y_{n+1} = \sigma_Y + R_{n+1}. \tag{16}$$

In each time-step the elastic trial stress tensor σ_{n+1}^* is calculated from quantities known and from chosen $\Delta\epsilon_{n+1}$, i.e.

$$\sigma_{n+1}^* = \sigma_n + \mathbf{D}^e : \Delta\epsilon_{n+1}. \tag{17}$$

Therefore, the trial yield condition

$$f_{n+1}^* = \frac{3}{2}(s_{n+1}^* - a_n):(s_{n+1}^* - a_n) - Y_n^2 \geq 0 \tag{18}$$

is checked, if the loading is active. If it is true, the nonlinear scalar equation must be solved

$$\Delta p_{n+1} = \frac{\sqrt{\frac{3}{2}(s_{n+1}^* - a_n)^T:(s_{n+1}^* - a_n)} - Y_{n+1}}{3G + \sum_{i=1}^{M} C_i \theta_{n+1}^{(i)}}. \tag{19}$$

The derivation of this equation was described by (KOBAYASHI M., OHNO N., 2002). For the bilinear kinematic hardening ($M =1$) without assumption of isotropic hardening, when $Y_{n+1} = Y_n = \sigma_Y$ the equation (16) can be solved directly, because $\theta_{n+1}^{(1)} = 1$. In other cases the solution can be found by an iterative algorithm, see Fig. 1.
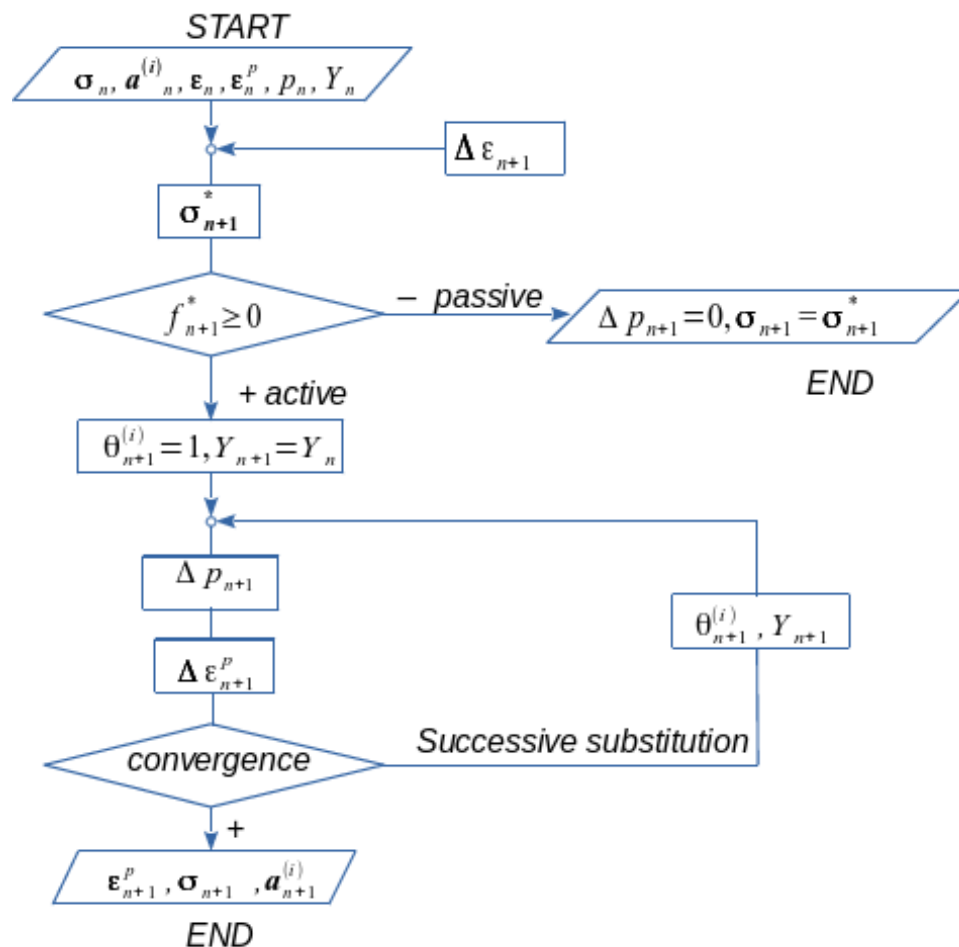

Fig. 8 – Stress integration scheme, see (HALAMA R., MARKOPOULOS A. et al, 2017)

http://aum.svsfem.cz

3.3   Radial return alorithm application

The need of tangent modulus calculation in each integration point was explained in the paper (HALAMA R., PORUBA Z., 2009). In order to reach parabolic convergence of the Newton-Raphson method in solution of global equilibrium equation, it is necessary to use the tangent modulus consistent with applied integration scheme. For simple hardening rules, for example Chaboche model, it is possible to determine the consistent tangent modulus in analytical way, see (KOBAYASHI M., OHNO N., 2002). In cases of more robust phenomenological models, it is sometimes necessary to use an approximation approach. For the MAKOC model with memory, the approximation approach proposed in (HALAMA R., PORUBA Z., 2009) has been applied.

4   MAKOC model with memory

The model based on AbdelKarim-Ohno (ABDEL-KARIM M., OHNO N., 2000) kinematic hardening rule was extended in the contribution (HALAMA R., FUSEK M., ŠOFER M., PORUBA Z., MATUŠEK P., FAJKOŠ R., 2015) by a stress based memory surface to take into account influence of stress amplitude on ratcheting of Class C steel (railroad wheel material). Only a comparison of predictions by Chaboche model (available in ANSYS) and MAKOC model with memory for an out of phase loading path are presented on the Fig.2.
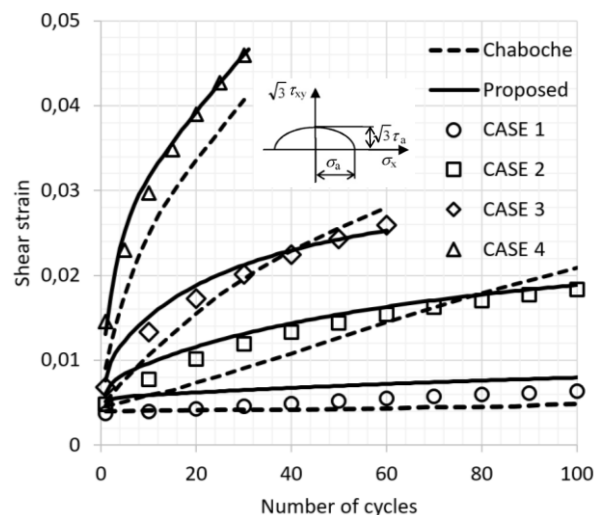
Fig. 9 – Multiaxial ratcheting prediction of Class C steel by Chaboche and MAKOC models, see (HALAMA R., ŠMACH J. et al, 2018)

5   Conclusions

Basic steps of the implementation procedure are specified in this paper. More detailed description can be found for instance in papers (HALAMA R., FUSEK M., 2005) and (HALAMA R., MARKOPOULOS A., JANČO R., BARTECKÝ M., 2017). Bilinear kinematic hardening rule do not require additional iterations in integration points in contrast with a nonlinear kinematic hardening rule. On the other hand, more robust cyclic plasticity models enable correct description of Non-Masing behavior, ratcheting, mean stress relaxation, additional hardening due to nonproportional loading and many other effects. The USERMAT.F subroutine can be used for a visoplastic model implementation too. Then, there is a possibility of creep – plasticity interaction description and so on.

The model MAKOC with memory based on AbdelKarim-Ohno kinematic hardening rule, which was proposed by author of paper, was also applied in less complex version in paper (HALAMA R., BARTECKÁ J., GÁL P., in press). All previously mentioned effects of

http://aum.svsfem.cz

cyclic plasticity can be described by the new model, which is important for many applications in industry.

References

ABDEL-KARIM M., OHNO N., 2000. Kinematic Hardening Model Suitable for Ratchetting with Steady-State. *International Journal of Plasticity*, Vol. 16, p. 225-240.

ANSYS, 2019, Ansys Multiphysics Manuals, Ansys Inc (1994-2019), Houston, USA.

CHABOCHE J.L., LEMAITRE J., 1990. Mechanics of Solid Materials. Cambridge University Press, Cambridge. ISBN 0-521-47758-1.

HALAMA R., BARTECKÁ J., GÁL P., in press. FE Prediction and Extrapolation of Multiaxial Ratcheting for R7T Steel. *Key Engineering Materials*.

HALAMA R., FUSEK M., 2005. Modifikace modelu cyklické plasticity s ohledem na multiaxiální ratcheting, část II. Implementace v programu Ansys. In: *Proceedings of Aplikovaná mechanika 2005*, March 29 - April 1, 2005. Hrotovice: Nahlik EtAl p. 33-34. ISBN 80-214-2373-0. (In Czech)

HALAMA R., FUSEK M., ŠOFER M., PORUBA Z., MATUŠEK P., FAJKOŠ R., 2015. Ratcheting Behavior of Class C Wheel Steel and Its Prediction by Modified AbdelKarim-Ohno Model, In: *Proceedings of the 10th International Conference on Contact Mechanics CM2015*, Colorado Springs, Colorado, USA, August 30 – September 3, 2015.

HALAMA R., MARKOPOULOS A., JANČO R., BARTECKÝ M., 2017. Implementation of MAKOC Cyclic Plasticity Model with Memory. *Advances in Engineering Software*, Vol. 113, p. 34-46.

HALAMA R. PORUBA Z., 2009. Tangent Modulus in Numerical Integration of Constitutive Relations and its Influence on Convergence of N-R Method. *Applied and Computational Mechanics*, Vol. 3, No.1, p. 27-38. ISSN 1802-680X.

HALAMA R., ŠMACH J., MATUŠEK P., SAKAINO T., 2018. Ratcheting prediction based development of rolling contact fatigue test for high pressures. In: *Proceedings of the 11th International Conference on Contact Mechanics and Wear of Rail/wheel Systems, CM 2018*, Delft, Netherlands, September 24 – 27, 2018, p. 350-355. ISBN 978-946186963-0.

KOBAYASHI M., OHNO A., 2002. Implementation of Cyclic Plasticity Models Based on a General Form of Kinematic Hardening, *International Journal for Numerical Methods in Engineering*, Vol. 53, p. 2217–2238.

Acknowledgement

Contact address:
doc. Ing. Radim Halama, Ph.D.
Department of Applied Mechanics, Faculty of Mechanical Engineering, VSB-TU Ostrava
17.listopadu 2172/15, Ostrava 70800, Czech Republic

Simulace spalování hnědého uhlí ve fluidním kotli

PAVEL FERKL, JINDRA KOSPRDOVÁ, PAVEL STŘASÁK
ENGINN EFFECT s.r.o.

Abstract:

Energy from burning of coal is still in widespread use in Czech Republic for heating of buildings and generation of electricity. From the process viewpoint, there are several challenges for operating a fluidized bed boiler. First, air inlets of boiler have to be designed to reduce local spots with high temperature as much as possible. High temperature leads to softening of the coal and its aggregation on boiler walls, which then leads to reduced boiler efficiency or unplanned shutdowns. Second, fluidized bed combustion processes often suffer from high amount of unburned carbon in flue, which lowers the overall efficiency. We developed a simulation procedure, which is detailed enough to capture important physical processes of coal combustion and at the same time it requires reasonable computing time. We primarily focused on analysis of flow field a tracking of particles of coal in the boiler. Finally, based on the simulation results, we proposed structural and operational changes, which should lead to higher efficiency and smoother operation.

Keywords: CFD, combustion, fluidised bed

1 Úvod

Spalování hnědého uhlí je celosvětově stále velmi využívaný způsob produkce energie, ať už pro výrobu elektřiny či užitného tepla. Existuje několik druhů technologií pro spalování uhlí. Mezi nejpoužívanější patří roštové spalování, práškové spalování, fluidní spalování a zplynování. Tento příspěvek se zaměřuje na numerické simulace fluidního spalování.U fluidního spalování se předem rozemleté palivo dostává nad fluidní rošt. Zde je proudem primární plynné směsi udržováno ve vznosu, v tzv. fluidní vrstě. Fluidní vrstvu pak mimo paliva typicky tvoří ještě další aditiva jako vápenec pro odsíření a písek pro zvýšení stability fluidní vrstvy. Mezi hlavní výhody tohoto způsobu spalování patří

- Relativně nízké teploty ve fluidní vrstvě, a tedy snížená produkce oxidů dusíku.
- Možnost přídavku dalších tuhých paliv jako biomasy nebo některých druhů odpadů.
- Postupné dávkování spalovacího vzduchu způsobuje nízkou koncentraci kyslíku ve většině spalovací komory a snižuje produkci oxidů dusíku.
- Možnost dávkování vápence pro částečné odsíření spalin.
- Typicky menší velikost zařízení potřebná k dosažení stejného výkonu oproti jiným technologiím.

Mezi nevýhody pak patří zvýšená citlivost na granulometrii paliva, zvýšené emise polyaromatických uhlovodíků a relativně dlouhé startovací časy. Pod fluidní rošty je přiváděno jen omezené množství vzduchu. V horní části fluidní vrstvy tak dochází především k odparu vody a těkavých organických složek. V dolní části pak probíhá reakce uhlíku na oxid uhelnatý. Navíc tím dochází k omezení úletu velkých popelových částic. K dospálení plynných reaktantů (oxidu uhelnatého a organických složek) pak dochází především v horní části spalovací komory.

Z návrhového a provozního hlediska je zajímavé mít znalost o proudovém poli ve spalovací komoře. Tato informace může pomoci pro vhodné umístění a rozvážení vzduchových vstupů, tak aby docházelo k dobrému promíchání plynných reaktantů a zároveň nedocházelo ke vzniku lokálnách míst s extrémně vysokou teplotou, která by mohla vést k měknutí popela a jeho napékání na stěny spalovací komory.Za tímto účelem se v posledních letech s úspěchem používá CFD simulací, které jsou schopné predikovat pole rychlostí, teplot a koncentrací hlavních složek. Druhou částí modelu je pak simulace pohybu a odhořívání diskrétních částic uhlí, která dává cennou informaci o úletu a případném nedopalu částic.Zbytek této zprávy je organizován následovně. Nejprve je představen numerický model, a vysvětleny jeho hlavní předpoklady. Následně jsou představeny typické výsledky simulací a okomentovány z nich plynoucí důsledky. Závěrem jsou pak shrnuty hlavní přínosy a limitace prezentovaného přístupu.

2   Metodika

Spalování uhlí je relativně složitý proces. Sestává se z několika kroků a částí, které je třeba zohlednit, pokud chceme vytvořit smysluplný model, jež bude popisovat reálné chování fluidního kotle. Celý model lze rozdělit na popis chování tří částí – plynné fáze, fluidního lože a palivové částice.

2.1   Plynná fáze

Proudové chování je modelováno pomocí Navierových-Stokesových, realizable k-epsilon (RKE) turbulentního modelu a stěnových funkcí. Při sdílení tepla jsou zahrnuty tepelné toky vedením, prouděním i sáláním. Typicky je známá teplota ve výparníku a přehříváku páry. Spolu s tloušťkou stěn pak tyto informace slouží k formulaci okrajových podmínek na stěnách spalovací komory. Jako radiační model je zvolena P1-aproximace [1], která představuje dobrý kompromis mezi přesností a výpočetní náročností.

U těchto typů simulací je vždy důležité zvolit vhodný spalovací model a reakční mechanismus. Mezi nejčastěji používané turbulentní spalovací modely patří Eddy-breakup (EBU) [2], Eddy-dissipation model (EDM) [3], Eddy-dissipation concept (EDC) [4] a Partially stirred reactor (PaSR) [5]. Z těchto modelů EB a EDM jsou založené na principu co je smíšené, to se spálí (limitace turbulentním mísením). Naopak EDC a PaSR navíc zohledňují i limitaci chemickou kinetikou. Lze pak využít již dříve publikovaných detailních reakčních mechanismů [6]–[8]. Pro prvotní výpočty zařízení lze doporučit EDM, který s nízkým výpočetním nákladem relativně přesně popisuje turbulentní difuzní plameny.

2.2   Fluidní lože

Fluidní lože je disperzní systém pevných částic v proudu plynné směsi. Z výpočetního hlediska není schůdné simulovat každou částici zvlášť včetně její interakce s proudovým polem, stěnami zařízení a ostatními částicemi. V realitě dochází díky těmto interakcím a změnám velikosti částic (rozpadem, agregací, odhoříváním, odparem, bobtnáním apod.) k jejich poměrně složitému pohybu [9]. Ve velkých průmyslových zařízeních je nutné tento proces zjednodušit a dívat se na fluidní lože jako porézní médium, které představuje odpor vůči proudu plynné směsi. Vzhledem ke geometrii spalovacích komor se často setkáváme s fluidními loži typu fontána. To lze zohlednit nastavením anizotropního odporu ve fluidním loži, tak aby odpor ve směru normály ke fluidnímu roštu byl menší než odpor v příčných směrech.

2.3   Palivové částice

V simulacích jsou částice uhlí modelovány pomocí tzv. diskrétních částic. Jedna částice v simulaci představuje mnoho reálných částic uhlí, které se pak v simulaci pohybují

jednotně. Tím se výrazně sníží počet částic, jejichž trajektorie je nutné predikovat a tím se sníží i výpočetní nároky.

Předpokládáme, že částice uhlí se skládají ze tří hlavních složek – vody, těkavých organických látek a pevných látek, a že při spalování podstupují několik po sobě jdoucích dějů [10]. Nejprve dochází k odparu vody. K odparu dochází, jakmile se teplota částice v simulaci zvýší nad určitou mezní hodnotu. Poté, co částice neobsahuje žádnou vodu, začínají se z částice odpařovat těkavé organické látky. Reálné uhlí obsahuje širokou škálu různých těkavých organických látek. V modelu jsou tyto látky nahrazeny jednou pseudo-složkou, jejíž molární hmotnost a spalné teplo je nastaveno tak, aby výhřevnost modelové částice odpovídala výhřevnosti uhlí. Pokud částice neobsahuje žádnou vodu ani těkavé organické látky, dochází k povrchové reakci uhlíku s kyslíkem. Vzhledem k tomu, že neuvažujeme zpětné reakce ani redukci uhlíku s oxidem uhličitým, předpokládáme, že produktem reakce je oxid uhelnatý.

3   Výsledky

Rychlostní pole ve spalovací komoře s fluidním ložem může vypadat jako na Obr. 1. Vzduch je do kotle dávkován z několika vstupů. Pod fluidní rošt je přiváděna primární směs vzduchu a recirkulačních spalin. Celkové množství plynu musí být dostatečné pro udržení paliva ve vznosu, avšak ne příliš vysoké, aby nedocházelo k nadměrnému úletu částic. Směs navíc musí obsahovat dostatek kyslíku pro spálení veškerého pevného uhlíku z paliva na oxid uhelnatý, ale ne o mnoho více, aby nedocházelo k nadměrně vysokým teplotám ve fluidní vrstvě. Další vzduch je poté přiváděn sekundárními a terciálními dýzami pro úplné spálení oxidu uhelnatého a organických těkavých látek.

Pokud je kotel provozován jako na Obr. 1, pak je značné množství vzduchu přiváděno až v horní části spalovací komory. Jedním z rizik tohoto přístupu je, že velmi vysoké výstupní rychlosti z terciálních dýz mohou vytvořit velký recirkulační vír, který se může zatáhnout až do dolní části spalovací komory a způsobit tam neočekávané lokální zvýšení teploty. Druhým problémem pak může být nestabilita víru v oblasti styku silných proudů z terciálních dýz, která může negativně ovlivnit hladký provoz kotle. Dalším rizikem pak je relativně krátká vzdálenost od terciálních dýz ke konci prvního tahu, což může vést na nedokonalé promíšení a vznik nehomogenního koncentračního pole složek.
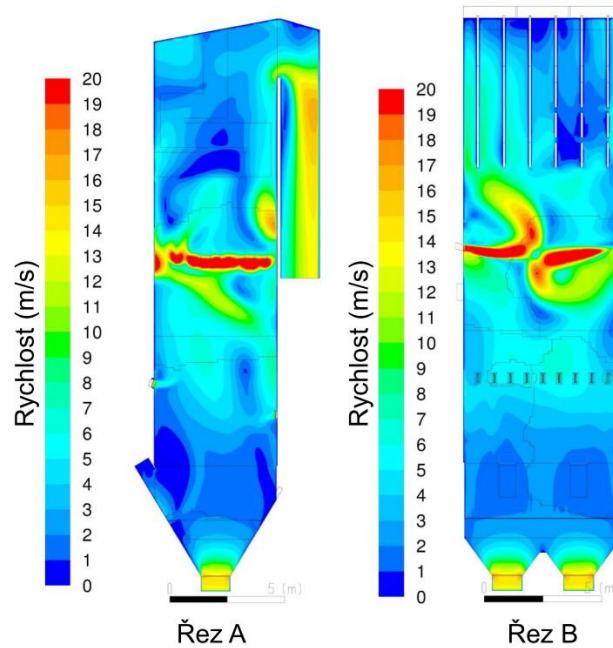
Obr. 1: Kontury rychlosti v příčném (Řez A) a příčném (Řez B) řezu.

Problém recirkulačního proudu je zřetelně vidět na konturách teploty v Obr. 2. V levé dolní části řezu A je vidět snížená teplota vlivem odparu vody z malých částic uhlí, které jsou záhy po vstupu do kotle unášeny vzhůru proudem plynu. Naopak v pravé dolní části řezu A je vidět zvýšená teplota způsobená recirkulačním proudem z terciálních dýz, který v této části způsobuje lokální zvýšení koncentrace kyslíku, a tedy intenzitu hoření. Při teplotách nad 1100 °C pak dochází k měknutí popelu a jeho napékání na stěny spalovací komory.
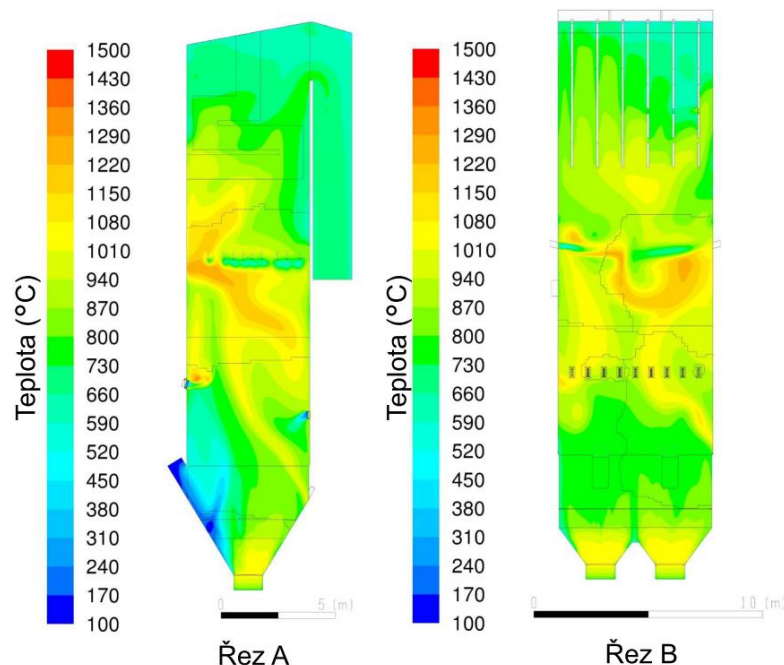
Obr. 2: Kontury teploty v příčném (Řez A) a příčném (Řez B) řezu.

Druhou částí simulace je poté analýza trajektorií částic uhlí (viz. Obr. 3). Pomocí této simulace je možné určit, jak velké částice mohou ze spalovací komory uletět a alespoň

přibližně predikovat nedopal v těchto částicích. Nejmenší částice (pod 100 μm) jsou ihned po vstupu unášeny do spalovací komory, kde postupně ztrácí vlhkost, organické těkavé látky a odhořívají. Velké částice (nad 1 mm) padají do fluidní lože, kde dochází k jejich pomalému odhořívání a případně rozpadu. Největší riziko z hlediska nedopalu tak představují středně velké částice, které podléhají riziku úletu, ale zároveň jsou příliš velké na to, aby došlo k odhoření veškerého pevného uhlíku.

Velikost částic 0,63 mm   Velikost částic 1 mm
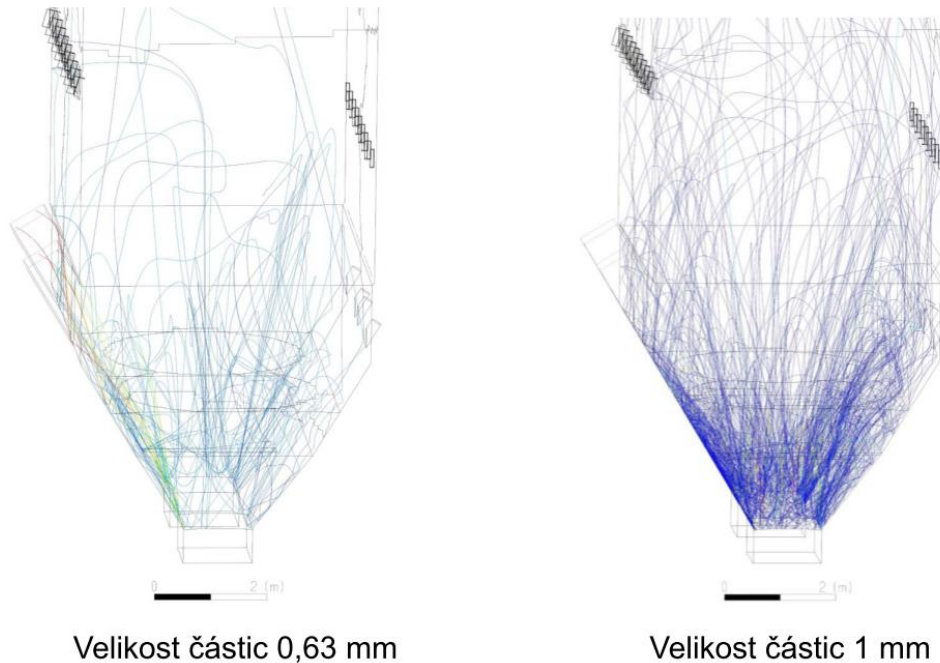
Obr. 3: Trajektorie částic obarvené hmotností částic.

4   Závěry

Fluidní spalování s sebou nese řadu výhod, jako např. flexibilitu ve výběru paliva, možnost částečného odsíření ve fluidním loži a relativně nízké teploty ve spalovací komoře, a tedy nízkou produkci oxidů dusíků. Technologie však s sebou nese i jistá rizika, jako např. vznik recirkulačních proudů, lokální vývoj velmi vysokých teplot a zvýšení nedopalu v úletu. Numerickými simulacemi lze predikovat jak rychlostní, teplotní a koncentrační pole ve spalovací komoře, tak pohyb palivových částic za provozních podmínek a tím případné problémy odhalit. S podporou výpočtů pak lze navrhnout úpravy vedoucí k optimalizaci celého procesu.

Literatura

[1] MODEST M. F., *Radiative Heat Transfer*, Second. Academic Press, 2003.

[2] SPALDING D. B, "*Mixing and chemical reaction in steady confined turbulent flames*," in Thirteenth symposium (international) on combustion, 1971, pp. 649–657.

[3] MAGNUSSEN B. F and HJERTAGER B. H, "*On mathematical modeling of turbulent combustion with special emphasis on soot formation and combustion*," Symp. Combust., vol. 16, no. 1, pp. 719–729, Jan. 1977.

[4] MAGNUSSEN B. F, "*On the structure of turbulence and a generalized eddy dissipation concept for chemical reaction in turbulent flow*," in 19th Aerospace Sciences Meeting, 1981, p. 7.

[5] KARLSSON J, "*Modeling auto-ignition,flame propagation and combustion in non-stationary turbulent sprays*," Chalmers university of technology, 1995.

[6] WANG H. et al., *"USC Mech Version II. High-Temperature Combtion Reaction Model of H2/CO/C1-C4 Compounds*," 2007. [Online]. Available: http://ignis.usc.edu/USC_Mech_II.htm.

[7] ZHOU C.-W. et al., "*An experimental and chemical kinetic modeling study of 1,3-butadiene combustion: Ignition delay time and laminar flame speed measurements*," Combust. Flame, vol.197, pp. 423–438, Nov. 2018.

[8] UCSD, "*Chemical-Kinetic Mechanisms for Combustion Applications*," 2019. [Online]. Available:http://combustion.ucsd.edu.

[9] ZHANG H, CEN K., YAN J., and NI M., "*The fragmentation of coal particles during the coal combustion in a fluidized bed*," Fuel, vol. 81, no. 14, pp. 1835–1840, Sep. 2002.

[10] BAUM M. M. and STREET P. J., "*Predicting the Combustion Behavior of coal particles*", Combust. Sci. Technol., vol. 3, no. 5, pp. 231-243, Jul. 1971.

Kontanktní adresa:
Ing. Michal Seifert
ENGINN EFFECT s.r.o.
Kolbenova 882/5a,
190 00, Praha 9

PROBABILISTIC ASSESSMENT TO ANALYSE OF THE SSI EFFECTS

JURAJ KRÁLIK, JURAJ KRÁLIK, jr.
Faculty of Civil Engineering STU in Bratislava
Academy of Fine Arts and Design in Bratislava

Abstract: This paper presents the results of the probabilistic and sensitivity analysis of the safety of the foundation plate considering the variability of the soil stiffness, structure geometry, permanent and variable masses. The advantages and disadvantages of the deterministic and probabilistic analysis of the foundation plate resistance are discussed. The sensitivity analysis of the foundations to the variability of the soil properties provides the important information for designers. The affectivity of the probabilistic design methodology is presented on the example of building foundation plate. The response surface method (RSM) for the analysis of the foundation plate reliability was used in program ANSYS. The probabilistic analysis gives us more complex information about the soil-foundation-structure interaction as the deterministic analysis.

Keywords: Soil-Structure Interaction, Probability, Sensitivity, RSM, ANSYS

1   Introduction

The requirements to design of the plate foundation increased due to development of calculation method and computer tools. The calculation model and resistance uncertainties determine the optimal design of the foundation plate. During the structural design process, an engineer has to consider problems of the soil-foundation and foundation-structure interaction in the point of view safety, reliability and durability of the structures. In the case of the high-rise buildings, the design of the foundation has the significant effect to safety of buildings.

Randomness in the loading and the environmental effects, the variability of the material and geometric characteristics of structures and many other "uncertainties" affecting errors in the computing model lead to a situation where the actual behavior of a structure is different from the modeled one (Rosovsky, 1995, US Army, 1995) .

Recent advances and the general accessibility of information technologies and computing techniques give rise to assumptions concerning the wider use of the probabilistic assessment of the reliability of structures using simulation methods (Baecher, 2003, Čajka, 2014, Janas, 2006, Keršner, 2006, Králik, 2006, 2009, Krejsa, 2016, Sýkora, 2013). Much attention should be paid to using the probabilistic approach in an analysis of the reliability of structures (Rosovský, 1995, Baecher, 2003, Čajka, 2014, Handbook 2, 2005, Králik, 2009)

The deterministic definition of the reliability condition has the form

$$R_d \geq E_d \tag{1}$$

and in the case of the probabilistic approach, it has the form

$$RF = R - E \geq 0 \tag{2}$$

where RF is the reliability function, which can be expressed generally as a function of the stochastic parameters X_1, X_2 to X_n, used in the calculation of R and E.

$$RF = g(X_1, X_2, ..., X_n) \tag{3}$$

The probability of failure is calculated as best estimation of the statistical parameters and theoretical model of the probability distribution of the reliability function Z= g(X).

The probability of failure is defined as best estimation of the numerical simulations in the form

$$p_f = \frac{1}{N} \sum_{i=1}^{N} I\left[g\left(X_i \right) \le 0 \right] \tag{4}$$

where N is the simulation number, $g(.)$ is the failure function, $I[.]$ is the function with value 1, if the condition in the square bracket is fulfilled, otherwise is equal to 0.

2   Calculation Model of the Foundation Plates

The resistance of the foundation plates of high rise buildings were investigated using the deterministic and probabilistic analyses. The considered building are 20 storey overground and 3 storey underground with storey height of 3m. The three types of the high rise building were considered. First model "D1" consists two cores and columns system, the foundation plate with dimension 21x36m and 1,5m thickness. Second model "D2" consists two central cores and columns system, the foundation plate dimension is 21x30m.
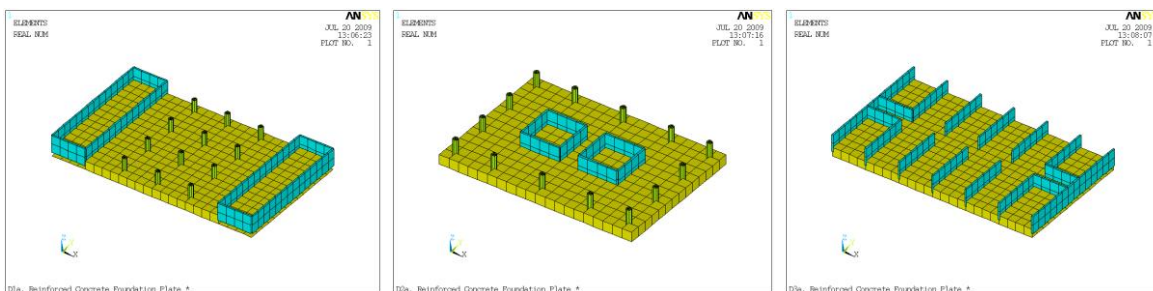

Image 1 Calculation models of foundation plate – D1, D2 and D3

All columns in these buildings are 600/600mm in cross-section. The thickness of floor reinforced concrete plate is 220mm. All floor slabs have a permanent load of 0.5kN/m2 and variable load of 2,0kN/m2. The material properties of this concrete building are Young's modulus, E = 30GPa and Poisson's ratio μ = 0.2.

The walls and foundation plate was modeled in software ANSYS using shell elements SHELL43, the Winkler subsoil by element SURFACE154 and the solid subsoil by element SOLID45. There are 544 shell, 13260 solid and 416 surface elements.

3   Soil-Foundation Interaction

The consideration of SSI effects is very important during the design process of the high rise building (Králik, 2006). The influence of the variability of the soil stiffness characteristic to the structure are not negligible (Baecher, 2003, Kotrasová, 2015, Králik, 2009, Krejčí, 2006, Melcer, 2016, Sucharda, 2018). The subsoil was considered as the layered medium typical to the environs of the City Bratislava (Table 1). The stiffness of the original subsoil is poor for the foundation of the high rise buildings usually. Hence the technology of the soil upgrading is used. The system KELLER propose the effective technology [Králik, 2006] of the soil upgrading (Table 1). The subsoil can be modeled by 3D FEM model or simple 1D Winkler model. In this paper the influence of the accuracy of these soil models to design of the foundation plate are considered. The most popular is the simple Winkler or Winkler-Pasternak model of the subsoil in practice (Králik, 2009, Kotrasová, 2015). These models are based on the theory of the 1D soil columns. Winkler constant C can be defined in the form (Baecher, 2003)

Table 1 The mechanical characteristic of the layered subsoil

	Original subsoil	Strengthened subsoil

Point	Soil typ	h_i [m]	γ [kNm^{-3}]	E_{def} [kPa]	v -	c_{ef} [kPa]	φ_{ef} [deg]	Soil typ	γ [kNm^{-3}]	E_{def} [kPa]	v -	c_{ef} [kPa]	φ_{ef} [deg]
1	G2	2,7	20	15330	0.43	0	31	G2+	23	75735	0.20	10	31
2	CH	3.5	19	17810	0.42	10	16	CH+	23	33747	0.42	10	16
3	ML	1.0	23	12728	0.46	18	25	Soilcret	25	900000	0.20	80	20
4	ML	2.8	19	11142	0.30	18	22	Soilcret	25	900000	0.20	80	20
5	SC	9.5	19	10266	0.40	10	28	SC	19	10266	0.40	10	28
6	CH	4.5	19	18692	0.35	10	16	CH	19	18692	0.35	10	16
7	SC	4.0	19	14953	0.35	10	28	SC	19	14953	0.35	10	28
8	CH	1.0	19	19938	0.35	10	16	CH	19	19938	0.35	10	16
9	SC	5.0	19	16200	0.35	10	28	SC	19	16200	0.35	10	28

$$C = \int_0^h E_{oed.k}\left(\frac{d\psi}{dz}\right)^2 dz \approx \frac{\sigma_o}{w} \tag{5}$$

where E_{oed} is the mean oedometric modulus, ψ is the shape function of the settlement along the depth of soil, σ_o is the contact stress from the building under the foundation, w is the settlement of the foundation. In the case of the layered soil the settlement may be calculated by STN 1001 using the following formula

$$w = \sum_{i=1}^n \frac{\sigma_{z,i} - m_i\sigma_{or,i}}{E_{oed,i}} h_i \, , \tag{6}$$

where $\sigma_{z,i}$ is the vertical stress in the middle of soil layer under foundation, m_i is the correct factor dependent on soil type, $\sigma_{or,i}$ is the original geostatic stress in the middle of soil layer, h_i is the layer thickness, $E_{oed,i}$ is the oedometric modulus of ith soil layer.

The Winkler subsoil can be modeled using surface elements SURF154 in the system ANSYS. These elements can be defined around of plate area to consider the effect of the soil resistance. The size of the boundary area L_w is determined as follow

$$L_w = (h_s\,/\,2).\tan(\varphi_{ef}) \tag{7}$$

4 Loading and Load Combination

The loading and load combination in the case of the deterministic as well as the probability calculation is different due to requirements of Eurocode 1990 (Handbook 2, 2005) and JCSS 2000 (JCSS, 2001), too. In the case of deterministic calculation of the structure the load combination is considered according to ENV 1990 as follows:

⮞ **Fundamental combination – deterministic method**

$$E_d = \gamma_g G_k + \gamma_q Q_k + \gamma_s \psi_{os} S_k \tag{8}$$

where G_k is the characteristic value of the permanent loads, Q_k - the characteristic value of the variable loading, S_k - the characteristic value of the snow loading, ψ_{os} - the combination factor according to ENV 1990 ($\psi_{os} = 0{,}6$). The load factors γ_g, γ_q, and γ_s are considered for the ultimate limit state ($\gamma_g = 1{,}35$; $\gamma_q = 1{,}5$; $\gamma_s = 1{,}5$) and serviceability limit state ($\gamma_g = 1{,}0$; $\gamma_q = 1{,}0$; $\gamma_s = 1{,}0$) in accordance with requirements of ENV 1990.

In the case of *probabilistic calculation* of the structure the load combination we take following:

⮞ *Fundamental combination– probabilistic method*

$$E = G + Q + S = g_{var}G_m + q_{var}Q_m + s_{var}S_m \tag{9}$$

where G_m is the mean value of the permanent loads, Q_m - the mean value of the variable loading, S_m - the mean value of the snow loading, g_{var}, q_{var}, s_{var} are the variable parameters defined in the form of the histogram calibrated to the load combination in compliance with Eurocode.

5　Uncertainties of Input Variables

The effect of soil-structure interaction can be investigated in the case of probabilistic assessment by sensitivity analysis of the influence of variable properties of soil (US Army, 1995, Baecher, 2003). A soil stiffness variability in the vertical direction is defined by the mean stiffness value $k_{i.k}$ from the geological measurement and the variable factor k_{i_var}. The stiffness of the structure is determined with the mean value of Young's modulus E_m and variable factor $e_{\_var}$. A load is taken with mean values G_m, Q_m, S_m and variable factors $g_{\_var}$, $q_{\_var}$ and $s_{\_var}$.

The uncertainties of the calculation model are considered by variable model factor θ_R and variable load factor θ_E for Gauss's normal distribution. In view of the uncertainties of calculation soil model and mechanical soil properties the various stiffness of soil are requirement to design foundation plate. In the deterministic analysis are used three values of the soil stiffness (Low-Medium-High), which values are determined from the median and lower and upper two quantile of this stiffness. These values of the quantile k_p can be defined for the normal distribution as follow

$$k_p = k_m.\left(1 \pm u_p.k_w\right) \tag{10}$$

where k_p is the quantil of the soil stiffness (for probability $P{=}0.05$ and $P{=}0.95$), k_m is the mean value of the soil stiffness, k_w is the value of the soil stiffness variation ($k_w{=}k_\sigma/k_m$), u_p is the normalized of the quantil values. On the base of the requirements (US Army, 1995) the standard deviation can be considered by 30% of mean value. The deterministic factors of the soil stiffness are utilized by values 0.5/1/1.5 (Low/Medium/High).

The random distribution of the input variables are considered on the base of the requirements ENV 1990. These values are calibrated to the ultimate limited state.

Table 2　Probabilistic model of input parameters

Name	Quantity	Mean value	Variable paramet.	Histogram	Mean	Stand. deviation	Min. value	Max. value
Soil	Layer stiffness	$k_{i,m}$	k_{i_var}	Normal	1.00	0.300	0.574	1.433
Material	Young's modul.	E_m	$e_{\_var}$	Normal	1.00	0.100	0.526	1.407
Action	Permanent	G_m	$g_{\_var}$	Normal	1.00	0.100	0.526	1.407
	Variable	Q_{m1}	$q_{\_var}$	Gama	0.60	0.350	0.005	4.073
	Snow	S_m	$s_{\_var}$	Gama	0.35	0.245	0.003	1.953
Model	Action uncertaint	θ_E	$e_{\_var}$	Normal	1.00	0.100	0.526	1.407
	Resist. uncertaint	θ_R	$r_{\_var}$	Normal	1.00	0.100	0.526	1.407

6　Reliability Criteria for Seismic Resistance of Structure

Reliability of the bearing structures is designed in accordance of standard requirements ENV 1992 for ultimate and serviceability limit state. The foundation reinforced concrete plate is designed on the bending and shear loads for ultimate limit state function as follow (Králik, 2009)

$$g(M) = 1 - M_E/M_R \geq 0, \qquad g(V) = 1 - V_E/V_R \geq 0 \tag{11}$$

where M_E, V_E are design bending moment and design shear force of the action and M_R, V_R are resistance bending moment and resistance shear force of the structure element.

The settlement w_E of the building is determined by the limit settlement w_R in accordance with ENV 1997 in the form (Králik, 2009)

$$g(w) = 1 - w_E / w_R \geq 0$$

(12)

where w_E is the vertical displacement, w_R is the limit value of building settlement.

7   Sensitivity Analysis

Sensitivity analysis of the influence of the variable input parameters to the reliability of the structures depends on the statistical independency between input and output parameters. Matrix of correlation coefficients of the input and output parameters is defined by Spearman (Králik, 2009).

The results of the sensitivity analysis of the settlement and bending moment of action of the foundation plate to the fundamental load combination in the model D2c are presented in the Image 2. These pictures present, that the variability of the input parameters q_{var}, g_{var} and s_{var} have the significant influence on the settlement and parameters q_{var}, g_{var}, e_{var}, s_{var} and $k_{4.var}$ are important for the bending moment m_x. The uncertainties of the variable load is first important parameter for the settlement and the bending moment and the variability of the permanent load for the shear forces. The ratio of the variability of input parameters is different in the model of foundation plate D1, D2 and D3. The configuration of the building walls and the columns impact to the behavior of the internal forces of the foundation plate.
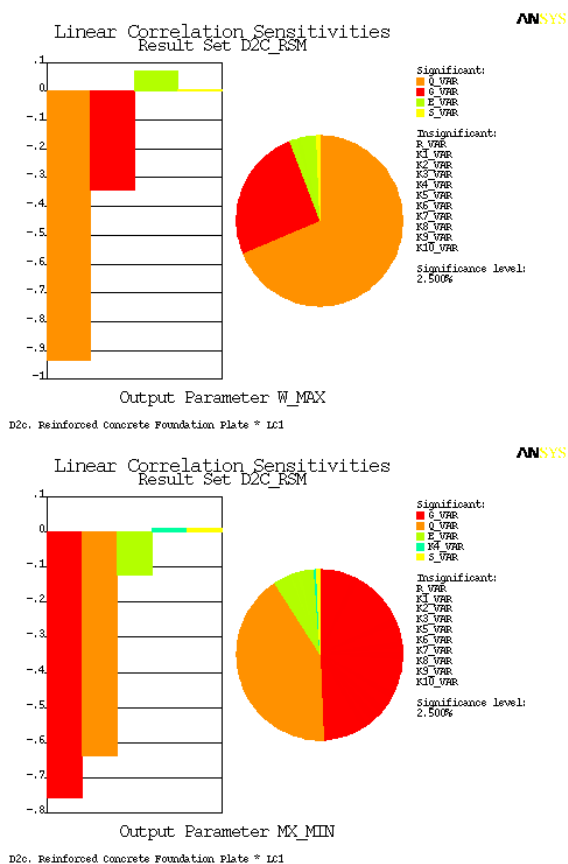

Image 2 Sensitivity analysis of the foundation plate settlement w and bending moment m_x
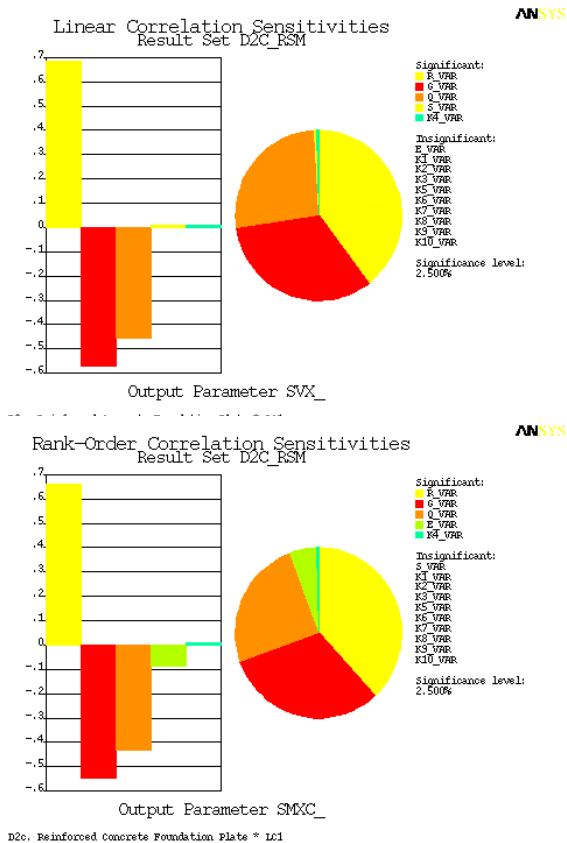
Image 3 Sensitivity analysis of the shear SVx and bending SMx safety function of plate

In the case of the shear and bending resistance sensitivity analysis of the plate, the most important variable parameters are the resistance r_{var} and q_{var}, g_{var}, $k_{4.var}$ also. The sensitivity of the safety function on shear resistance and bending resistance is presented in the Image 3. The sensitivity analysis gives the valuable information about the influence of uncertainties of input variables (load, material, model,) to engineer for optimal design of the structures.

8   Comparison of Deterministic and Probabilistic Analyses

Deterministic calculation of the resistance of the foundation plate for three type of wall and columns configuration was realized on the models D1, D2 and D3. The calculation model of the subsoil was considered as a) Winkler under plate area, b) Winkler under plate area and around strip, c) Solid under and around of plate area. The stiffness of Winkler constants are calculated from the equation (10). In the case of the soil model (b) the full and reduced stiffness (br) were considered.

Table 3 Comparison of deterministic analyses of the foundation plate

Model		w_{max}		M_{max}		V_{max}	
		[mm]	[%]	[kNm]	[%]	[kN]	[%]
D1	a	-136,09	118	304.45	116	640.30	83
	b	-116.89	101	152.44	58	648.27	84
	br	-161.39	140	221.21	84	824.33	107
	c	-115.48	100	262.67	100	767.73	100

D2	a	-90.83	54	97.09	113	541.46	88
	b	-89.04	53	115.59	42	521.32	62
	br	-132.42	78	163.89	50	718.06	60
	c	-169.23	100	233.48	100	871.13	100
D3	a	-73.15	71	223.16	57	416.67	77
	b	-38.05	37	103.88	82	354.79	65
	br	-59.65	58	164.47	78	458.95	84
	c	-102.85	100	285.51	100	543.16	100

Note: Winkler model = a). b). br); Solid model = c)

Table 4 Comparison of the deterministic and probabilistic analyses

Model		w_{max} [mm]			M_{max} [kNm]			V_{max} [kN]		
		min	mean	max	min	mean	max	min	mean	max
D1c	D	-202.95	-115.48	-100.82	189.97	262.67	418.37	659.09	767.73	927.90
	P	-111.18	-86.24	-66.41	191.23	228.16	265.89	453.57	554.16	668.88
D2c	D	-223.89	-169.23	-139.10	190.65	233.48	328.09	746.72	871.13	1059.00
	P	-148.60	-107.92	-78.82	154.02	184.69	217.06	530.07	642.01	765.17
D3c	D	-192.32	-102.85	-71.06	205.95	285.51	458.77	453.43	543.16	711.09
	P	-264.95	-126.52	-85.12	211.29	252.28	294.20	341.18	411.50	487.56

Note: D = deterministic, P = probabilistic analysis; min and max values are defined for the 5 and 95% probability to noexceedence

The reduction is defined by the ratio of the plate area and total subsoil area

$$k_{red} = A_p / (A_p + A_s),$$ (13)

where A_p is plate area, A_s is the subsoil area around of foundation plate. The results from the deterministic analysis with the different soil model (see Table 3) show us that the maximal difference is equal 63% of the settlement in the model D3, 68% of the bending moment in the model D2, and 38% of the shear forces in model D2. The scatter of the values of the output quantities is dependent on the structural system too.

The comparison of the deterministic and probabilistic analyses on the same soil model D3c (Table 4) show us that the maximal difference between the 95% quantile and mean deterministic value of the output quantity is equal 83% of the settlement in the model D3, 7% of the bending moment in the model D2, 13% of the shear forces in model D1. The scatter of the values of the internal forces from the deterministic and probabilistic analysis on the same soil model is lower as the difference between various soil models. The probabilistic results give us the less conservative values than the deterministic analysis.

9   Conclusions

This paper presented the results of the probabilistic and sensitivity analysis of the safety of the foundation plate considering the variability of the soil stiffness, structure geometry, permanent and variable masses. The advantages and disadvantages of the deterministic and probabilistic analysis of the foundation plate resistance were analysed [9]. On the example of three type of the high rise buildings the affectivity of the probabilistic design methodology was presented. The approximation method RSM of simulation for the

analysis of the foundation plate reliability was used on program ANSYS. The comparison of the deterministic and probabilistic analyses on the same soil model D3c show us that the maximal difference between the 95% quantil and mean deterministic values of the internal forces are minor as 13%. The scatter of the output quantities between Winkler simple model and solid soil model is higher than the differences between the deterministic and probabilistic analysis in the same soil model. The probabilistic analysis gives us more complex information about the soil-structure interaction than the deterministic analysis [9].

Acknowledgement

References

BAECHER G. B. JOHN T. CH., 2003. *Reliability and Statistics in Geotechnical Engineering*, John Wiley&Sons, Ltd, ISBN 0-471-49833-5.

ČAJKA R. KREJSA M., 2014. Measured Data Processing Using the DOProC Method. *Applied Mechanics and Materials*. Volume 501-504. Durnten-Zurich: Trans Tech Publications, 859(1), s. 114-121. ISBN 978-3-03835-005-7.

HANBOOK 2, 2005. Implementation of Eurocodes Reliability Backgrounds. Guide of the basis of structural reliability and risk engineering related to Eurocodes. Development of Skills Facilitating Implementatio of Eurocodes. Leonardo Da Vinci Pilot Project CZ/02/B/F/PP-134007. Prague, CR.

JANAS P. KREJSA M. KREJSA V., 2006. Structural Reliability Assessment Using Direct Determined Fully Probabilistic Calculation, In Proc. *3rd International ASRANet Colloquium*, (abstract p.8, full paper on CD), Glasgow, UK, ISBN 0-9553550-0-1.

JCSS-OSTL/DIA/VROU-10-11-2000, 2001. *Probabilistic Model Code, Part 1, Basis of Design, Working material,* http://www.jcss.ethz.ch/.

KERŠNER Z. NOVÁK D. VÍTEK J. L. TEPLÝ B., 2006. Decision-making support based on virtual statistical modelling: Case study of large subway tunnel launching. In Proc. *International Congress,* p. 3070-3077, Montreal, 2006, ISBN 2-921145-58-8.

KOTRASOVÁ K. GRAJCIAR I. KORMANÍKOVÁ E., 2015. "A Case Study on the Seismic Behavior of Tanks Considering Soil-Structure-Fluid Interaction," *Journal of Vibration Engineering and Technologies*. Vol. 3, pp. 315-330.

KRÁLIK J., 2006. Probabilistic Analysis of the robust problems in FEM by methods MC, IS, LHS and RSM under system ANSYS. In: *VII. Conference of Structure Reliability, Theme: Assesment of probabilistic design from the element and component to systems*, Prague, pp.57-66, ISBN 80-02-01770-6. (in Slovak)

KRÁLIK J. 2009. *Reliability Analysis of Structures Using Stochastic Finite Element Method*. Ed. STU Bratislava, 2009, 143 pp.

KRÁLIK J. KRÁLIK J. jr., 2006. Probability and Sensitivity Analysis of Soil-Structure Interaction of High-Rise Buildings. *Slovak Journal of Civil Engineering*, Slovak University of Technology Bratislava, ISSN 1210-3896, Vol. 14, No. 3, pp.18-32.

KRÁLIK J. KRÁLIK J., jr., 2009. Probability and Sensitivity Analysis of Machine Foundation and Soil Interaction. *Applied and Computational Mechanics*. ZCU Plzen. ISSN 1802-680X, 2009, Vol.3, No.1.

KREJSA M. BROŽOVSKÝ J. JANAS P. ČAJKA R. and KREJSA, V., 2016. Probabilistic Calculation Using Parallel Computing. In: *Engineering Mechanics 2016 : 22nd international conference* : May 9-12, 2016, Svratka, Czech Republic : book of full texts. Prague: Institute of Thermomechanics, Academy of Sciences of the Czech Republic, p. 347-350. ISBN 978-80-87012-59-8.

KREJČÍ T., KOUDELKA T., ŠEJNOHA J., KUKLÍK P., 2006. Numerical Analysis of Foundation Slabs, *Proceedings of the Eighth International Conference on Computational Structures Technology* [CD-ROM], Civil-Comp Press Ltd, ISBN 1-905088-07-8.

MELCER J. et al., 2016. Dynamics of Transport Structures (in Slovak), (EDIS, Žilina, 2016), pp.374, ISBN 978-80-554-1178-1.

SUCHARDA O. ŠMIŘÁKOVÁ M. VAŠKOVÁ J. MATEČKOVÁ P. KUBOŠEK J. and ČAJKA R., 2018. Punching Shear Failure of Concrete Ground Supported Slab. *International Journal of Concrete Structures and Materials*, 12(1), s. 1-14. ISSN 1976-0485.

SÝKORA M. HOLICKÝ M., 2013. Assessment of Uncertainties in Mechanical Models, In: *Applied Mechanics and Materials*, Vol. 378, pp 13-18, © Trans Tech Publications, Switzerland.

ROSOVSKY D. V., 1995. *Structural Reliability*. Part of publication W.Chen, The Civil *Engineering Handbook*, CRC Press, W.F.Chen Ed. Clemson University, SC.

US Army Corps of Engineers, 1995. *Engineering and Design, Introduction to Probability and Reliability Methods for Use in Geotechnical Engineering*, ETL 1110-2-547, CECW-EG, No. 1110-2-547, 30 September, Washington.

CFD CALULATION OF AIRFLOW DISTRIBUTION IN GENERATOR

PAVEL ŠTURM[1], JIŘÍ VONDÁL[2], BRANISLAV ZUŠTIN[2]
[1]BRUSH SEM s.r.o., [2]SVS FEM s.r.o.

Abstract: The purpose of this project was to develop the calculation methodology for the air cooled turbo-generators using Computational Fluid Dynamics (CFD). This method focuses especially on a complex ventilation design calculations of the rotating machines. It is needed at the stage of prototype designing as well as at the stage of increasing power of currently manufactured generators (very often requested on smaller machines which are used on trailers). With this method it is possible to design well balanced cooling multi-compartment system, improve basic ventilation system and reduce or even eliminate hot spots.

The main focus of this project was to investigate limitations in air distribution design, verification of the new calculation method with testing on manufactured machine and improving the ventilation system of the machines wherever needed and possible.
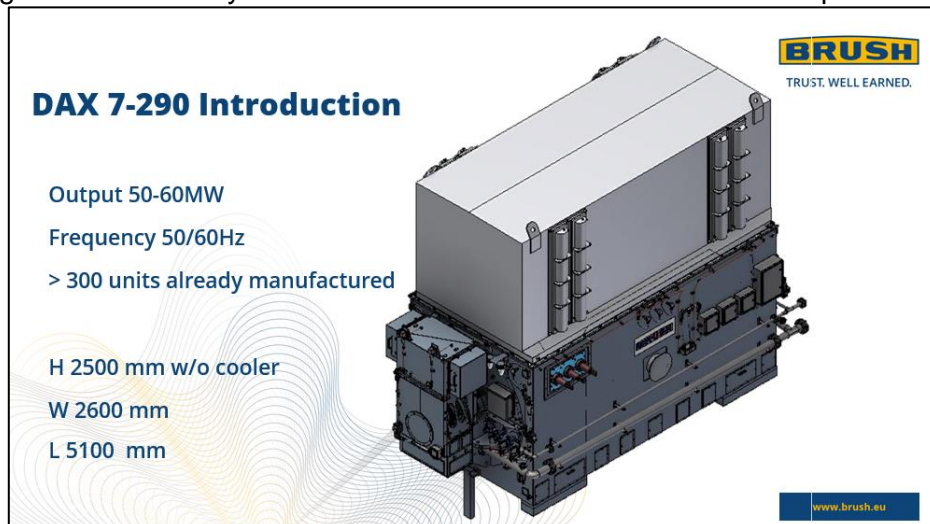
Image 1 – Brush generator DAX 7-290

Keywords: CFD, ventilation, turbo generator, rotating machine

1 Description of Brush Generators' Ventilation

Brush generators are cooled by air either in open circuit, filter ventilated or closed water cooled configuration. The generators internal air system is similar in all cases. Cooling air is forced around the generator by means of two axial fans mounted on the rotor shaft. The air is distributed into 3 main ventilation branches behind the fan.

One branch leads air across the stator endwinding to transfer duct which ends in cooling compartment. Second branch leads air into the rotor and the third branch leads air into the gap between stator and rotor where the air is mixed by the air from other branches. Such a mixed air is going through the stator radial ducts to the generator exhaust to ambient atmosphere or to the cooler depends on the configuration.

The rotor cooling air is flowing under the rotor endcap and is split into next 3 ventilation branches- one for cooling the endwinding and exhaust from the rotor endcap. Next two branches lead air for cooling the rotor body through the subslots beneath the winding slot and through interslots between the winding slots. The cooling air escapes from

the subslots through radial exhaust ducts along the length of the winding while the exhausts from interslots are positioned in the center of the rotor.
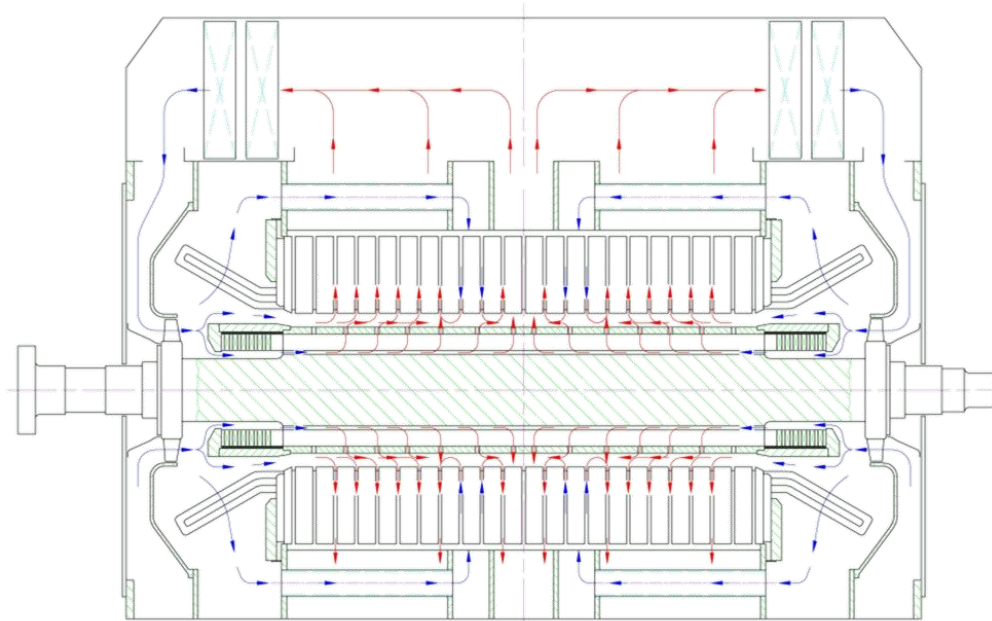

Image 2 – Scheme of generator ventilation system

2   Project Workflow

2.3 Geometry

The geometry was created in CAD system Autodesk Inventor and later simplified for further CFD use in ANSYS SpaceClaim. The original 3D model was created for the production of the real generator so a lot of modifications, simplifications and changes were needed. Anyway all of the modifications should have no impact on CFD calculation of airflow distribution inside the machine. The main goal was to create CFD model as close as possible to the real model to get the results which correspond to data from the real testing. After the model was simplified inverse volume of air was created and split to several smaller regions for meshing purposes.

2.3 Mesh

Calculation mesh was created in ICEM CFD software. This was the most time consuming stage of the whole project. The model is very complex with a lot of detailed parts on the order of millimeters combined with generator which spans to the order of meters. Bottom-up approach was used for mesh creation. In ICEM it is possible to create high quality mesh with lot of geometry details and low HW demands.

With the dimensions of the whole machine approx. 2500 x 2600 x 5100 mm and for example stator radial ducts approx. 10 x 460 mm, rotor subslot and interslot length 1450 mm with cross section in the range of millimeters and hundreds of small gaps and openings, creating the high quality mesh was a challenge.

Non-conformal boundary interface was used at the stator-rotor connection. The center of air gap was defined as the position of that interface which is in agreement with the calculation of rotational models theory.

Active core of rotor and stator were meshed separately and later joined into one grid in Fluent solver. The computational grid consists of approx. 100 mil cells with the lowest orthogonal quality 0.57.

Rotor endwinding, stator endwinding and fan suction area were also meshed separately. Its surface mesh was created in ANSYS ICEM CFD, imported into Fluent Meshing and meshed with native polyhedral cells. Total cell count was 17.5 million with maximal skewness 0.79.

Total 139 181 897 cells,

88 126 464 hexaelements, 51 055 433 polyhedral elements
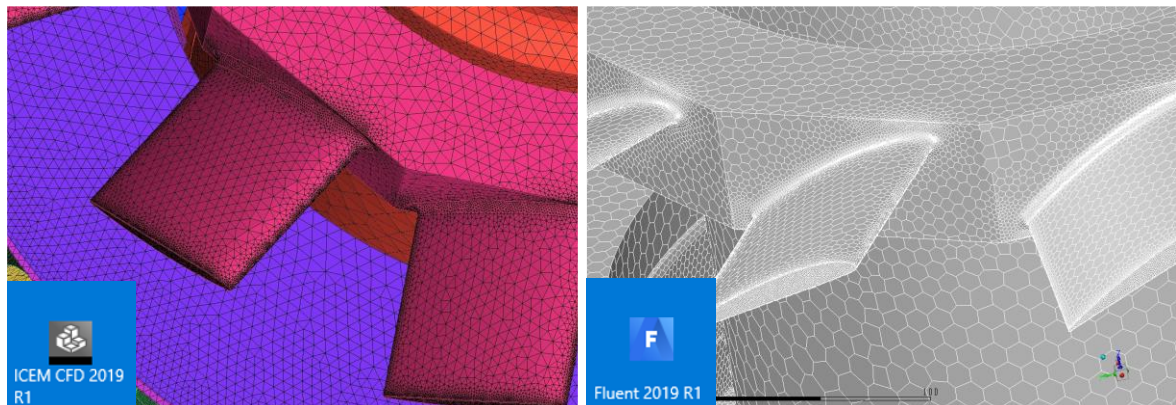
Image 3 – Example of calculation mesh in ICEM CFD (L) and Fluent (R)

2.3 CFD Calculation

ANSYS Fluent was used as primary solver. All the calculations were performed on single computer – processing station.

2.3.1 Calculation Settings and Boundary Conditions

Boundary condition of the model was set based on previous calculations. To achieve required flow rate the inlet was set to type Mass Flow Inlet and two outlets to type Pressure Outlet. This combination enhances the numerical stability of the solution. Walls were set to no-slip conditions. Since the Moving Reference Frame (MRF) procedure was used the rotational speed for the rotor part was set to 3000 rpm (50 Hz). Coupled solver was used with pseudo-transient approach. Spatial discretization was set to second-order upwind scheme, but the turbulence quantities which were set to First Order Upwind. Turbulence was modelled with realizable k-epsilon model and Enhanced Wall Treatment wall function.
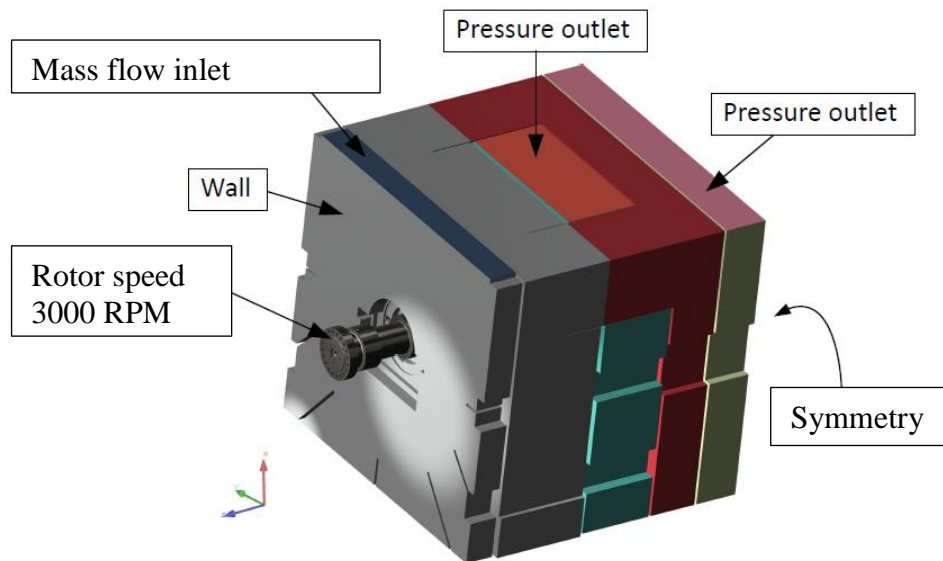
Image 4 – Boundary conditions setup on external faces

2.3.2   Used Hardware

All calculation was performed on processing station equipped with 745 GB RAM and Intel® Xeon® Gold 6154 CPU @ 3.00GHz processor.

RAM demands: Single precision – 276 GB, Double precision - 408 GB

Total wall clock time required for 1 iteration was 81 seconds with 32 cores.

3.1 CFD Results

The main output from CFD analysis was airflow distribution inside turbogenerator. A total of 420 different locations were monitored and evaluated for its air flow rate and ventilation effect. Monitoring was automatized through journal script with enhanced reporting capabilities.
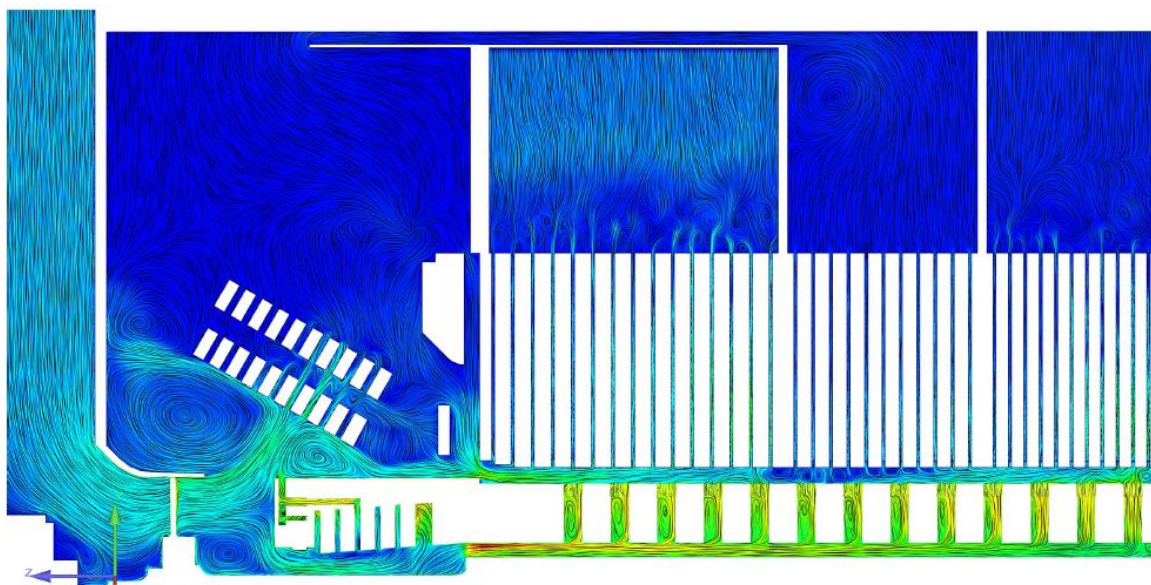
Image 5 – Contours of velocity magnitude

http://aum.svsfem.cz
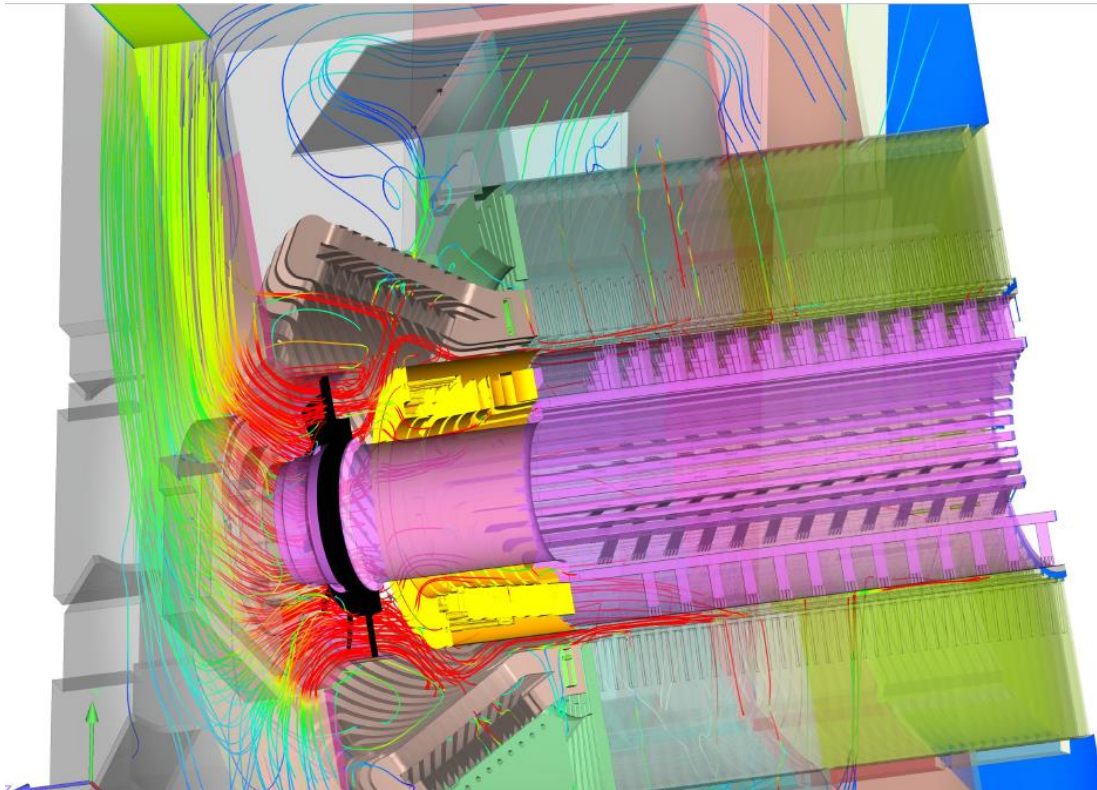
Image 6 – Pathlines coloured by velocity magnitude

3 Validation of CFD Results

3.1 Ventilation Measurement on Real Machine

To validate all air flow calculations it is necessary to compare the calculation results with ventilation measurement. Measuring on a rotating rotor is practically impossible. Therefore Brush proposed the measurement on a non-rotating rotor fed by two, identical, external fans. Distribution of air flow in such a static rotor is almost identical to distribution in rotating rotor.

On the other way, it is possible to measure stator ventilation on the completed machine during standard tests.

Stator

The machine without connected electrical supplies ran at full speed until air temperature stabilizes. Data were taken from many thermocouples, RTDs and air pressure tubes.

Bottom / top transfer duct, inlet / outlet:

Prandtl tube, fixed on a rod, was moved uniformly across the left or right half of the cross-section of the ducts or the auxiliary duct. It was positioned at the openings of machine's inlet/outlet.

Stator ducts:

Prandtl tubes were inserted into the outlet of the duct. The position was in the middle of its width, 60 mm before the duct end. Only ducts accessible through outlet openings on the upper wall of the machine (inspection panels) were measured. There were 2 measuring points in each duct – on the left and right side, 550 mm from the vertical plane of symmetry, measured on the circumference of stator yoke.

Image 7 – Stator ventilation measurement

Rotor

Measurement of the axial air flow distribution was conducted on a non-rotating (stationary) production rotor. Two radial fans were connected via chambers and channels to the rotor. The air flow rate supplied by fans and consequently the pressure in chambers was adjustable. Total air flow rate was measured by two Thomas cylinders attached to the fan inlet.

Special gadget was used to measure flow rate in subslot. It was placed step by step on groups of holes in wedges. The anemometer probe was connected to the output pipe of the gadget and the air velocity in the extension vas measured.

To measure flow rate in interslot, Brush used the auxiliary air channel shown, which was put step by step on the exhaust of the interslot. The mean velocity on the channel output was determined by an integration of the velocity profile by means of the anemometer probe.

To measure flow rate in endwinding under the rotor end cap Brush used the anemometer probe applied directly on the gap output. To make measuring easier, we divided the gap into 4 equal sectors on the rotor circumference. The mean velocity on the sector outputs was acquired by an integration of the velocity profile using anemometer.

Image 8 – Test stand when assembly is completed.

3.2 CFD Model Sensitivity

How the CFD model is behaving when geometry is changed was compared to test on real machine. Transfer duct were blocked on the machine and the same way simulated by CFD. The modifications which were tested consisted of fully open and partially blocked ducts. Partial blockage was 50 %, 75 % and 90 % of the original cross section.

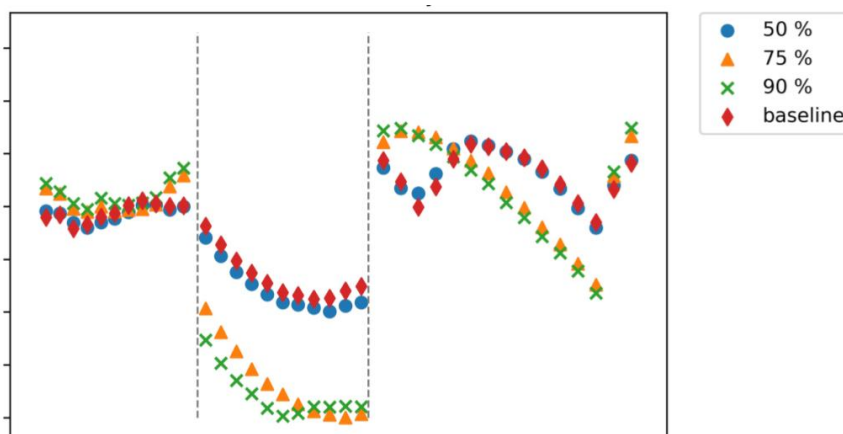Image 9 – Transfer ducts blocking by using woody covers with appropriate cross section holes

Image 10 – Comparison of the airflow quantity in stator radial ducts along the machine in different modification of machine's ventilation configuration.

3.3 Comparative Study of Using ANSYS CFX/Fluent

Comparison was conducted to validate simulations by another tool. The aim was to investigate benefits and drawbacks of each software. The CFX focuses on rotating machines, while Fluent is more general CFD software. There was a little difference in setup procedure and resulting velocity field. Since Fluent can benefit from direct connection to Fluent Meshing it was chosen as primary tool for following simulations.
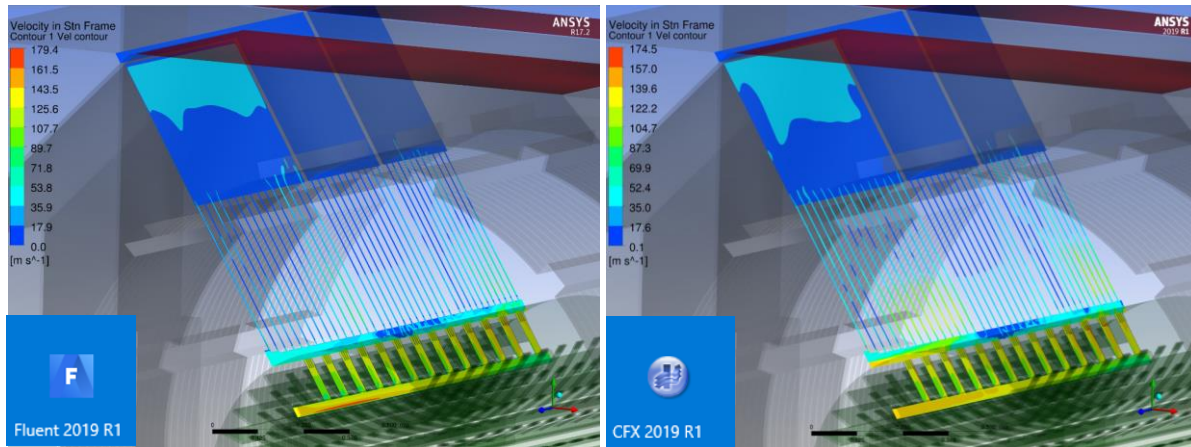

Image 11 – Comparison of the velocity contours reached by Ansys Fluent (L) and Ansys CFX (R).

3.4 CFD Transient Solution Compared to Steady Solution

While the steady state solution took 3 days of calculation the transient solution took 14 days for 1 real rotor turn.

The results from transient solution confirms accuracy of steady solution using Moving reference frame/ frozen rotor approach.
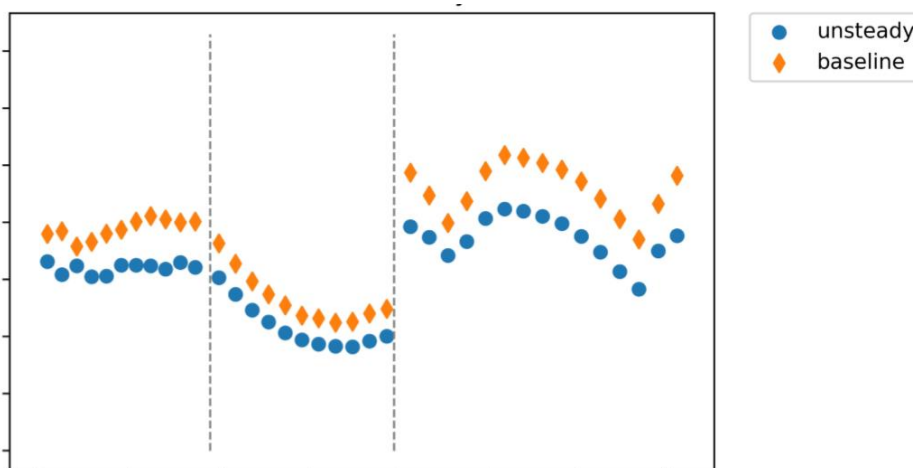
Axial distance from the central axis of machine (L) to end of stator core (R)

Image 12 – Comparison of the airflow quantity in stator radial ducts along the machine for steady and transient setting of calculation

3.5 Analytical Calculation

Brush's in-house code for analytical calculation is based on ventilation resistance network according to image 13.

Air flow distribution of the generator is calculated as follows:

• Ventilation calculation of rotor separately was done by the program "TBRv_4". The slot part was solved like channel with branches, the end part of winding as thermo-siphon effect.

• Ventilation calculation of stator separately, was done by the program "TBSk_5" as preliminary one. The method of calculation is similar to the "TBRv_4", the slot part.

• The complete ventilation calculation of generator was done in the program "DOC1_1k2". The air flow in branches of one half of generator (ventilation symmetry) were solved as matrix of square and linear equations.
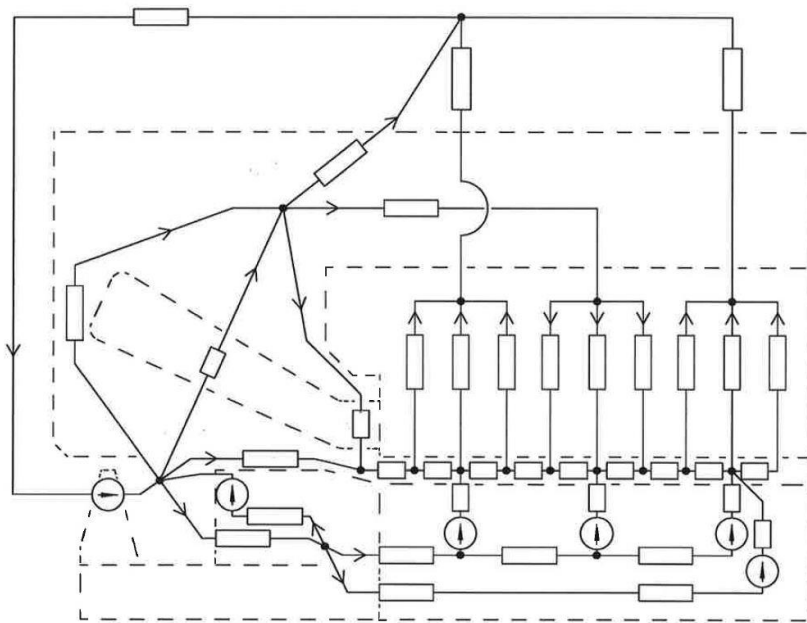

Image 13 – Example of the ventilation resistance network

4   Summary

Comparison of CFD predictions and analytical calculations with ventilation measurement was accomplished.

The calculations were done on half of the rotor due to symmetry. The velocities in the slot part were taken from the punched slits. Comparison between calculation and measurement has been done for identical cross section of channels – see below.

The measured values are the mean values in appropriate channels and cross sections.
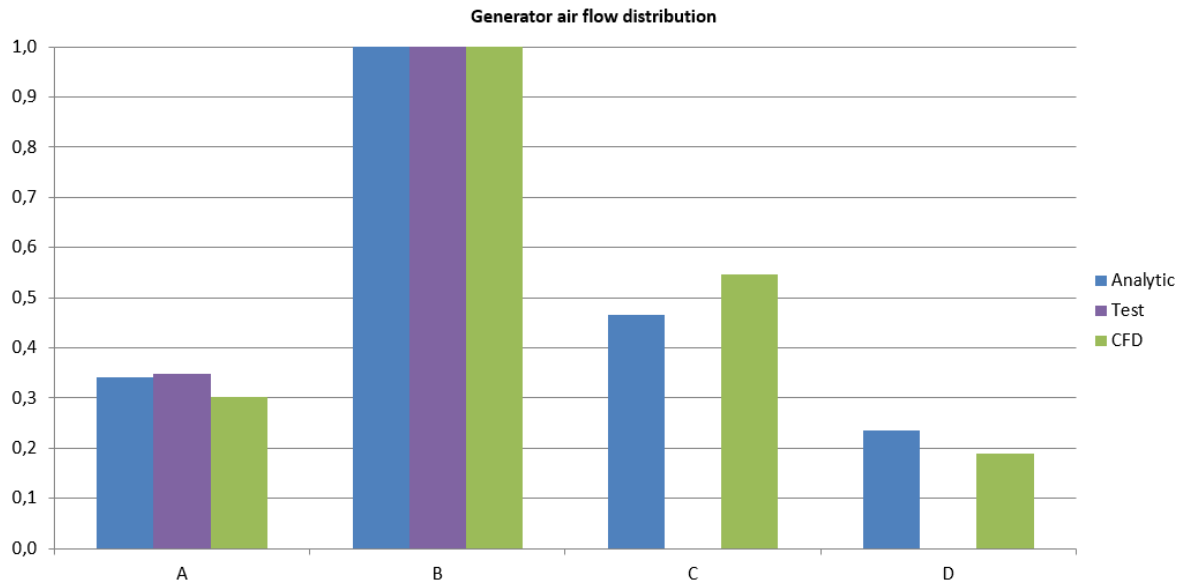
Generator air flow distribution

Image 14 – Generator airflow distribution. Transfer duct inlet (A), total airflow across the fan (B), air flow into airgap between stator and rotor (C), airflow into the rotor (D).
Note: (C) and (D) not possible to measure therefor measurement from nonrotating rotor was taken for the comparison and is shown in image 15.
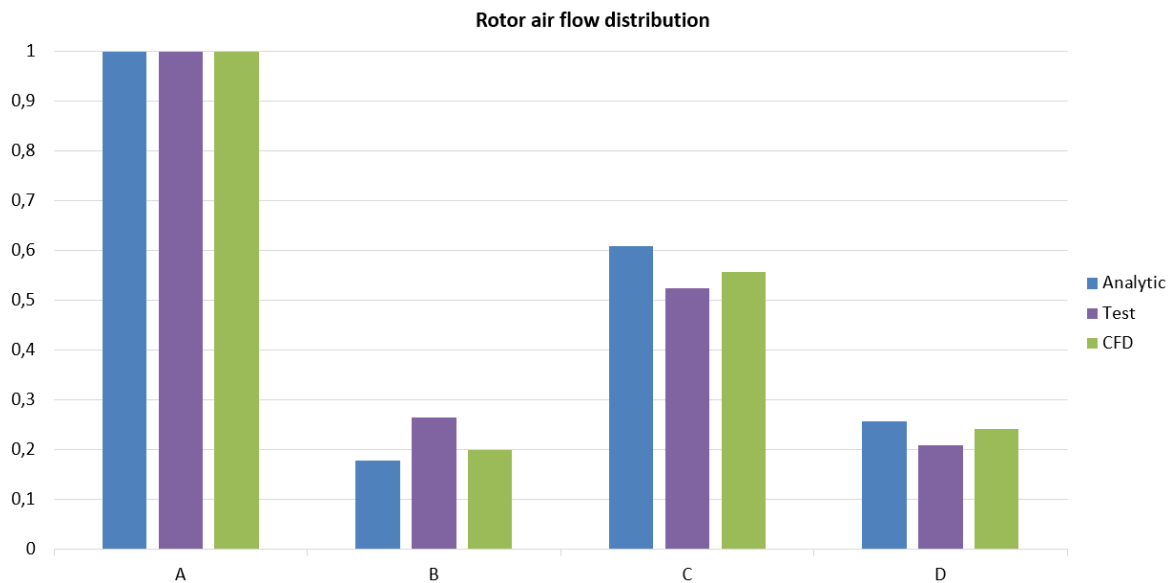
Rotor air flow distribution

Image 15 – Rotor airflow distribution. Total airflow to rotor (A), airflow from radial exit of rotor endcap (B), subslot radial flow (C), interslot radial flow (D)
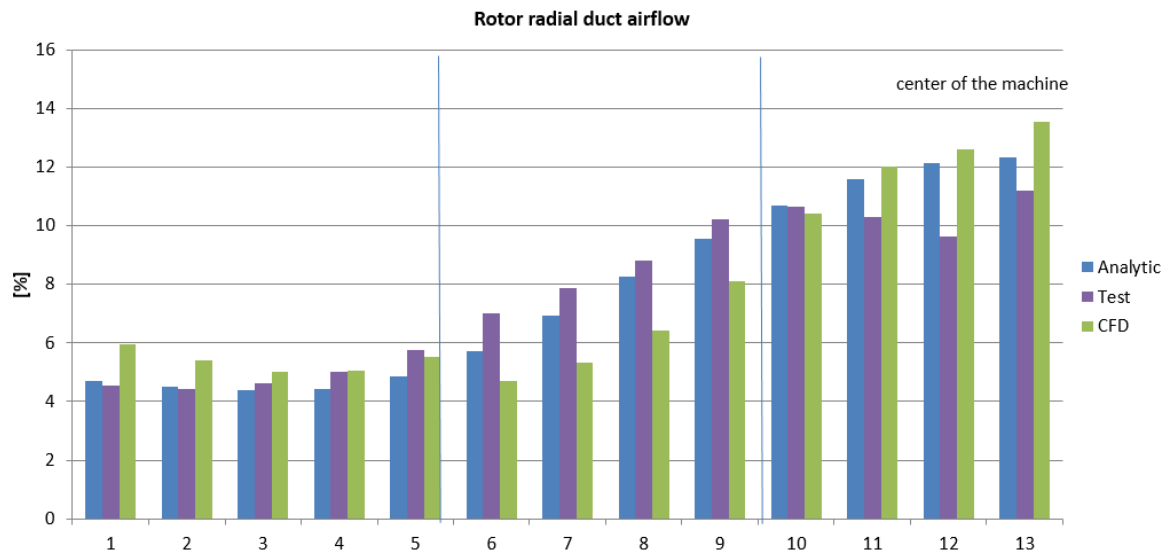
Image 16 – Subslot airflow distribution along the rotor

Image 17 – Stator radial duct airflow distribution along the stator

5   Conclusion and Planned Future Activities

Values and trends from CFD are confirmed by the ventilation measurement on the real machine even on different design configuration. Methodology of using the steady state solution was confirmed by comparison to the transient calculation. Analytical calculations provide good results in comparison to CFD. Nevertheless, it is not able to capture all details which are currently needed by the market with increasing demand for higher power density of each machine.

Future activities: Temperature distribution calculation

References

Brush internal documentation, test protocols, manuals, technical reports etc.

Contact address:
Pavel Šturm, BRUSH SEM s.r.o.
Edvarda Beneše 564/39
301 00 Plzeň, Doudlevce
Pavel.sturm@brush.eu

http://aum.svsfem.cz

Scientific and professional quality of conference is guaranteed by SVS FEM s.r.o. and Faculty of Electrical Engineering and Communication Brno University of Technology together with many professionals from different scientific and industrial areas. Conference papers are reviewed by Editorial board.

Editorial board

Chairman:
Prof. Ing. Jaroslav Buchar, Dr.Sc. (SVS FEM s.r.o., Škrochova 42, 613 00 Brno, The Czech Republic)

Members (alphabetically):
Ing. Tibor Bachorec, Ph.D. (SVS FEM s.r.o., Škrochova 42, 613 00 Brno, The Czech Republic)
Ing. László Iván, Ph.D. (SVS FEM s.r.o., Škrochova 42, 613 00 Brno, The Czech Republic)
prof. Ing. Horyl Petr, CSc., dr.h.c. (Dpt. of Mechanics, Technical University of Ostrava, 17. listopadu 15, 708 00 Ostrava, The Czech Republic)
doc. Ing. Petr Koňas, Ph.D. (SVS FEM s.r.o., Škrochova 42, 613 00 Brno, The Czech Republic)
Ing. Jarmil Schwangmaier (SVS FEM s.r.o., Škrochova 42, 613 00 Brno, The Czech Republic)
Ing. Miroslav Stárek (SVS FEM s.r.o, Škrochova 42, 613 00 Brno, The Czech Republic)